The PHILOSOPHICAL MAGAZINE

FIRST PUBLISHED IN 1798

. 2 Eighth Series No. 19 July 1957

A Journal of Theoretical Experimental and Applied Physics

PRICE £1 5s. 0d.
Annual Subscription £13 10s. 0d. payable in advance

ALERE FLAMMAM.
Printed and Published by
TAYLOR & FRANCIS LTD.
RED LION COURT, FLEET STREET, LONDON, E.C.4

Crossing Symmetry and the Relativistic Equation for two Fermions†

By S. F. Edwards and P. T. Matthews‡
Department of Mathematical Physics, University of Birmingham

[Received March 19, 1957]

Abstract

A consideration of the symmetries of the scattering matrix of two fermions leads to the proposal of a linear scattering equation. This equation, unlike the ladder approximation, is shown to have all the symmetries and invariance properties of the true t matrix. In the limit of one of the fermions becoming indefinitely heavy the relation of this and the ladder approximations to the Dirac equation is discussed and it is shown how a covariant equation which reduces to the Dirac equation in the no-recoil can be formulated.

§ 1. Introduction

The construction of relativistic two body scattering equations is a well-known procedure from the work of Bethe and Salpeter (1951), and Schwinger (1951). In this formulation the equation for the two body propagator (or wave function) is a clear generalization of the non-relativistic equation, and can also be viewed as a summation of a series of Feynman integral, in the simplest case the ladder summation. However, the complete solution of the problem satisfies several invariance requirements, in particular a relativistic theory must exhibit the correct statistics between ingoing and outgoing particles as well as the usual symmetries amongst ingoing and outgoing where appropriate. The former crossing symmetry is a very powerful restriction in the theory of nucleon–meson scattering and must necessarily be satisfied by any theory of this reaction (Chew and Low 1956, Feldman and Matthews 1956). In particular, if one wishes to use the relativistic analogue of ordinary potential scattering, the Bethe–Salpeter equation, which in the ladder approximation violates this symmetry, has to be modified to include it before it can be successfully applied. After modification a very simple theory of meson–nucleon scattering results, which agrees with experiment, and with discussions based upon unitary and causality which are sufficient alone in no-recoil theory to indicate the form the solution will take (Chew and Low 1956, Edwards and Matthews 1957 a). This paper discusses

† Communicated by Professor R. E. Peierls, C.B.E., F.R.S.
‡ Present address: University of Rochester, Rochester, N.Y., U.S.A.

whether the crossing symmetry imposes any serious restrictions upon processes involving two fermions and whether the theory can be modified to admit this symmetry. It has been noted elsewhere (Edwards and Matthews 1957, henceforth I) that the crossing symmetry does indeed exist for two fermion scattering, but is of vital importance only if one of them can annihilate with the other. For this case the modified equation for the propagator has to be used before a successful theory can be evolved. In the limit of the mass of one of the fermions tending to infinity, the exact equation for the other is of course the Dirac equation, but this is not easily obtained from the relativistic equations. This difficulty is discussed and it is shown how the modified equation improves the situation.

§ 2. Crossing Symmetry for Two Fermion Scattering

The crossing symmetry for fermions has been discussed in detail elsewhere (I), so here we shall simply quote the results. If the process is illustrated diagrammatically as in fig. 1 with p_1, p_2 incoming momenta and q_1, q_2 outgoing momenta, considering the particles as distinguishable for the moment, then if one introduces

$$\left.\begin{aligned} r_1&=p_1+q_1 \\ r_2&=p_2+q_2 \\ r_3&=p_1-q_1=q_2-p_2 \end{aligned}\right\} \quad . \quad . \quad . \quad . \quad . \quad . \quad (1)$$

the t matrix satisfies

$$[t(r_1, r_2, r_3, \gamma^{(1)}, \gamma^{(2)})]=t^{\mathrm{Tr}(1)}(-r_1, r_2, r_3, \gamma^{(1)\,tr}, \gamma^{(2)}) \quad . \quad . \quad (2)$$

$$=t^{\mathrm{Tr}(2)}(r_1, -r_2, r_3, \gamma^{(1)}, \gamma^{(2)\,tr}). \quad . \quad . \quad (3)$$

The indices Tr(1), Tr(2) mean transpose of all matrices in the 1 and 2 spaces respectively. This algebraic operation is equivalent to swinging over the 1 lines, then reversing the arrow on the line (fig. 2), and similarly for the 2 line.

Fig. 1

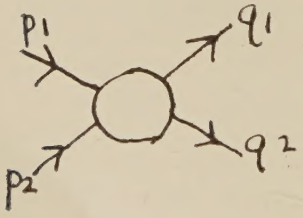

Fig. 2

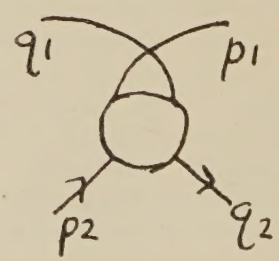

These remarks are true only for even interactions, i.e. those which do not change sign under charge conjugation, e.g. the pseudoscalar meson interaction γ_5. For interactions involving a change of sign under charge conjugation the t matrix has to be considered a function of the coupling constant which changes sign upon crossing. The diagrams illustrated are for particle–particle scattering but of course the t matrix also includes

particle anti-particle scattering which diagrammatically amounts to a reversal of arrows on the anti-particle line.

In the centre of mass system, the meson–nucleon crossing symmetry operation transforms the energy ω and cosine of the angle between initial and final relative momentum $z(=k\,.\,k^1/k^2,\ k^2=k^{12})$ into ω_1 and z_1 where

$$\omega_1\sqrt{(m^2+\omega_1{}^2-\mu^2)}+\tfrac{1}{2}(\omega_1{}^2-\mu^2)(1+z_1)$$

$$=-\omega\sqrt{(m^2+\omega^2-\mu^2)}-\tfrac{1}{2}(\omega^2-\mu^2)(1+z) \quad . \quad . \quad . \quad . \quad (4)$$

$$(\omega^2-\mu^2)(1-z)=(\omega_1{}^2-\mu^2)(1-z_1). \quad . \quad . \quad . \quad . \quad . \quad (5)$$

For $m \gg w$ these become

$$\omega_1=-\omega+(1+z)(\omega^2-\mu^2)(m+2\omega)^{-1}+0(m^{-3}) \quad . \quad . \quad . \quad (6)$$

$$z_1=z-2m(1-z^2)(m-2\omega z)^{-1}+0(m^{-3}) \quad . \quad . \quad . \quad . \quad (7)$$

and so correspond approximately to reflection in energy. It is shown in I that for fermion–fermion scattering the corresponding relation is

$$\omega_1{}^2=-(\omega^2-\mu^2)(1+z)/2. \quad . \quad . \quad . \quad . \quad . \quad . \quad (8)$$

Whereas in the meson–nucleon case the t matrix at ω is approximately related to its value at ω, which by simple manipulations can, for example in effective range theory, be related back to the value at ω, the form (8) offers little information on the structure of the corresponding t matrix, since there is no simple relation between ω_1 and ω or indeed any physical energy. However, when say nucleon–anti-nucleon scattering is considered, it can be shown (I) that the scattering contains a part t_1, which satisfies (8) and can be expressed in terms of nucleon–nucleon scattering (except for states for which the latter is excluded by statistics), and also a part t_2 which satisfies the crossing relation

$$\omega^2=\omega_1{}^2, \quad z_1=-z. \quad . \quad . \quad . \quad . \quad . \quad . \quad . \quad . \quad (9)$$

This is a restriction as powerful as that of meson–nucleon scattering and any theory must conform to it. Even in the nucleon–nucleon case the observance of the crossing symmetry brings the theory much nearer to a form which allows non-relativistic and no-recoil limits to be taken correctly. In § 3 the theory will be set up in invariant form.

§ 3. The Invariant Theory

In this section is derived the simplest relativistic generalization of the non-relativistic theory which satisfies all the invariance properties discussed above. This will neglect self energy effects, i.e. virtual emissions and absorption in which the same fermion emits as absorbs, though the formalism can be extended without difficulty to these processes if required. A rigorous derivation of the relativistic equation is given in the Appendix using Schwinger's functional differential formalism, whilst in what follows we shall put it forward as a plausible consequence of our invariance

requirements. Consider for example two nucleons (taken not identical); the ladder approximation for their propagator is

$$(S_1^{-1}S_2^{-1}+I_{12})G_{12}(1,\,2\,;\,3,\,4)=\delta(1-2)\delta(3-4) \quad . \quad . \quad . \quad (10)$$

where

$$S_1^{-1} \equiv \frac{\gamma_\mu^{(1)}}{i}\frac{\partial}{\partial x_\mu^{(1)}}+m_{(1)}. \quad . \quad . \quad . \quad . \quad . \quad . \quad (11)$$

Similarly S_2^{-1} and I_{12} is the interaction which in ladder approximation of pseudoscalar meson theory is $g^2\gamma_5^{(1)}\gamma_5^{(2)}\Delta(13)\delta(2-4)\delta(3-4)$. The t matrix is obtained from G_{12} by the substitution

$$G_{12}=S_1S_2+S_1S_2tS_1S_2, \quad . \quad . \quad . \quad . \quad . \quad . \quad (12)$$

integrations being suppressed, and satisfies

$$t_{12}(1,\,2\,;\,3,\,4)=-I_{12}(1,\,2\,;\,3,\,4)$$
$$+\int\int I_{12}(1,\,5\,;\,36)S_1(5,\,7)S_2(6,\,8)t_{12}(7,\,2\,;\,8,\,4)$$
$$\times d^4\,7d^4\,8d^4\,5d^4\,6. \quad . \quad . \quad . \quad . \quad . \quad . \quad . \quad . \quad . \quad . \quad . \quad (13)$$

This equation is shown symbolically in fig. 3. It contains the series of ladder diagrams when the first approximation for I is taken, and omits crossed diagrams, i.e. those in which meson lines cross. In the Bethe–Salpeter approach these diagrams are included by altering I_{12}, and in principle I_{12} can be written down to make the equation exact, the formal expression for example in terms of functional derivatives having been

Fig. 3

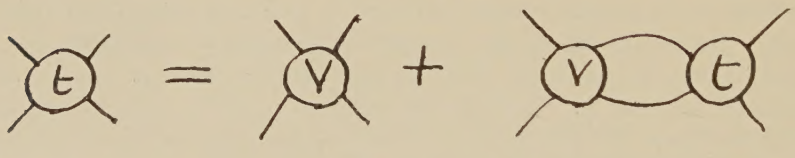

Fig. 4

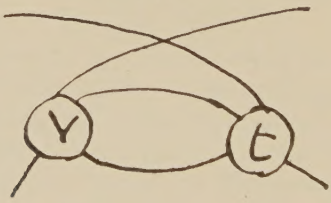

given by Schwinger (1951). Here it is proposed to symmetrize the kernel of (13) by adding the crossed term derived from it (fig. 4). To have the crossing also on the lower fermion line (i.e. time reversal) the whole thing should be symmetrized, leading finally to

$$t(1,\,2\,;\,3,\,4)=-I_{12}(1,\,2\,;\,34)+\tfrac{1}{2}\int\int\int\int d^4\,5d^4\,6d^4\,7d^4\,8$$
$$\times[I_{12}(1,\,5\,;\,3,\,6)S_1(5,\,7)S_2(6,\,8)t_{12}(7,\,2\,;\,8,\,4)$$
$$+I_{12}(2,\,5\,;\,3,\,1)S_1(5,\,7)S_2(6,\,8)t_{12}(7,\,1\,;\,8,\,4)$$
$$+t_{12}(1,\,5\,;\,3,\,6)S_1(5,\,7)S_2(6,\,8)I_{12}(7,\,2\,;\,8,\,4)$$
$$+t_{12}(2,\,5\,;\,3,\,6)S_1(5,\,7)S_2(6,\,8)I_{12}(7,\,1\,;\,8,\,4)] \quad . \quad . \quad . \quad (14)$$

which is given diagrammatically in fig. 5. I in this equation now satisfies all the symmetry properties of t in all approximations as it clearly does in the first. For the complete analysis both (13) and (14) can be exact (with different I function of course), but (14) satisfies all the symmetry and invariance properties for t in its approximate form. The original form (10) can be discussed as a homogeneous equation, i.e. a wave equation, but this is not possible in the symmetrical form. The reason is that we are emphasizing the symmetry relations between initial and final states, which is not an easy concept in terms of wave functions.

Fig. 5

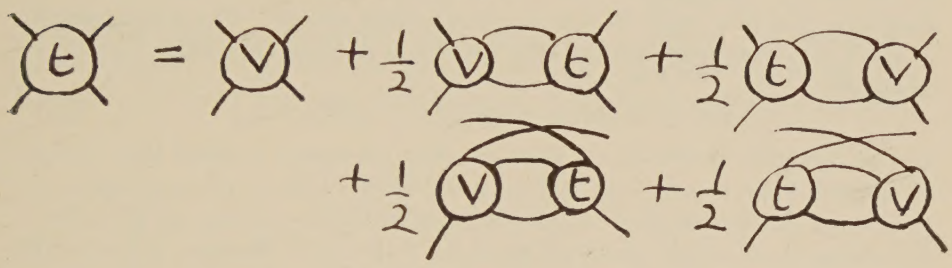

Fig. 6

Fig. 7

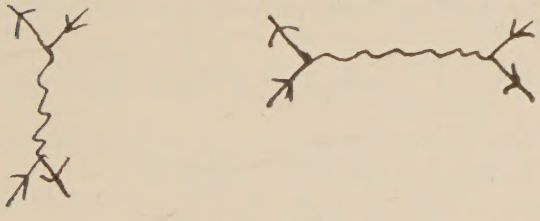

Using Born approximation for I the new equation fails at the third iteration since it gives the diagrams of fig. 5 with a coefficient of $\frac{1}{2}$ instead of unity. This has to be compensated for by a change in I without altering the invariance property of I.

When the two fermions can interchange through the interaction, e.g. proton, neutron and charged meson, I will contain the two types of diagram of fig. 6. For nucleon–anti-nucleon scattering these terms are given by fig. 7.

This structure of terms containing a pair annihilation and creation, and those in which nucleon and anti-nucleon lines run continuously through a graph, typify the two classes of term which the diagram series can be split into. Though this is not an easy concept mathematically, the diagrams reveal very simply the fact that part of the nucleon–anti-nucleon scattering resembles nucleon–nucleon, whereas part is quite different.

§ 4. The No-Recoil Limit

If one of the fermions becomes infinitely heavy, the problem is *exactly* determined by the Dirac equation for the light fermion in the potential of the heavy. Being exact the Dirac equation must be the sum of *all* the diagrams and it is easy to see how this comes about. The propagators of the heavy fermions become step functions in time and delta functions of space

$$S(1, 2) \to \Theta(t_1\, t_2) \exp[(im(t_1 - t_2)]\delta(x_1 - x_2) \quad . \quad . \quad . \quad (15)$$

and an integration over boson lines entering the heavy fermion line, when all diagrams are summed, is just an integration of the time coordinate of the vertex from $-\infty$ to $+\infty$, all the step functions adding up to unity. For example, in second order we have fig. 8 (parts of diagrams not shown being identical).

Fig. 8

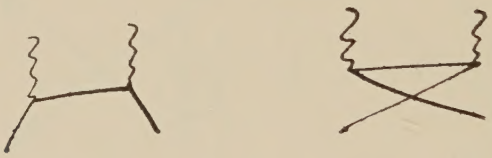

These give, when the exponential factors are removed by end conditions, the integrals

$$\int_{-\infty}^{\infty}\int_{-\infty}^{\infty} dt_1 dt_2[\Delta(A, 1)\Delta(B, 2)\Theta(1, 2) + \Delta(A, 1)\Delta(B, 2)\Theta(2, 1)]$$

$$\equiv \int_{-\infty}^{\infty}\int_{-\infty}^{\infty} dt_1 dt_2 \Delta(A1)\Delta(A2) \equiv V(a)V(b) \quad . \quad . \quad . \quad (16)$$

where a, b are the (space) distances of A, B from the origin where the heavy fermion is, and $V(a)$ the static potential

$$V(a) = \int_{-\infty}^{\infty} \Delta(A, 1) dt_1.$$

Since all diagrams are required to get the no-recoil limit it is clear that no approximation which can be expressed in terms of diagrams can ever give the correct limit, though clearly eqn. (14) is very much closer to it than eqn. (13) which does not even resemble the symmetry required to take the limit.

Since no 'set of diagrams' can give the required limit it is interesting to note that there is a simple addition to (14) (though not a unique

addition), which gives an estimate of the missing term, is covariant and yields the correct no-recoil limit. Say for example we are considering electron–proton scattering given diagrammatically by fig. 9,

$$t(1,2\,;3,4)=\gamma_\mu^{(1)}\gamma_\mu^{(2)}D(1,3)\delta(1-2)\delta(3-4)$$
$$+\tfrac{1}{2}\gamma_\mu^{(1)}\gamma_\mu^{(2)}D(1,3)\iint S(1,5)S(1,6)t(5,6\,;3,4)d^4\!5d^4\!6$$
$$+\text{sym. terms.}$$

Then the addition of the term

$$\frac{1}{8}\iint\gamma_\mu^{(1)}D(1,5)S_1(1,6)\left\{\gamma_\mu^{(2)},\left\{t(6,2\,;3,4),\left(\frac{1}{\gamma^{(2)}S_2(3,4)\gamma^{(2)}}\right)\right\}\right\}S_2(5,4)$$
$$\times d^4\!5d^4\!6$$

provides a possible extension. (The brackets { } stand here for anti-communicator.) This can be thought of as a 'diagram' as in fig. 10. Indeed in the field theoretic derivation of the Appendix it is represented

Fig. 9

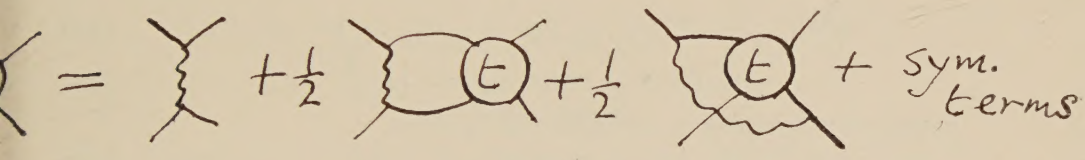

Fig. 10

by a functional derivative of the t matrix. This term removes an S_2, and replaces it by an $S_2\gamma S_2$ as required. If this procedure were exact this form would be symmetric between the two fermions, and if this symmetry is important clearly a term symmetric between the two fermions could be employed. The S function in the denominator could of course never occur in the more usual kind of expansion.

Acknowledgments

The authors would like to thank Mr. J. S. Langer for several helpful comments, and Professor Peierls for useful discussions.

References

Bethe, H. A., and Salpeter, E. E., 1951, *Phys. Rev.*, **84,** 1232.
Chew, G. F., and Low, F. E., 1956, *Phys. Rev.*, **101,** 1570.
Edwards, S. F., and Matthews, P. T., 1957 a, *Phil. Mag.*, **2**; 1957 b, *Ibid.*, **2**; 1957 c (to be published).
Feldman, G., and Matthews, P. T., 1956, *Phys. Rev.*, **101,** 1212.
Schwinger, J. S., 1951, *Nat. Acad. Sci.*, **37,** 452.

APPENDIX

The Derivation of the Equation

This most convenient technique for the calculation of equations of this type is the functional differential, introduced by Schwinger. Since we deal only with nucleon–nucleon scattering and shall not consider radiative corrections it is convenient to eliminate right away the meson variables, whereupon the effective equations of motion become

$$\left(\frac{\gamma_\mu}{i}\partial_\mu+m-g^2\int \Delta(xy)[\bar{\psi}(y),\,\gamma_5\psi(y)]d^4y\right)\psi(x)=\eta(x) \tag{A1}$$

where η is the spinor source. Taking expectation values and differentiating with respect to η

$$S'(x,\,x')=\delta\langle\psi(x)\rangle/\delta\eta(x') \tag{A2}$$

$$\delta\langle K\rangle/\delta\eta=i[\langle K\bar{\psi}\rangle_+-\langle K\rangle\langle\bar{\psi}\rangle] \tag{A3}$$

so that

$$\left(\frac{\gamma_\mu}{i}\partial_\mu+m-g^2\int \Delta(x,\,y)[\mathscr{D}(y,\,z),\,\gamma_5\overline{\mathscr{D}}(y,\,z)]\right)S'=\delta(x-x') \tag{A4}$$

$$\mathscr{D}(y,\,z)=S'(y,\,z)(\delta/\delta\langle\psi(z)\rangle)-\langle\bar{\psi}(z)\rangle. \tag{A5}$$

Suppressing integration variables this becomes

$$S'=S+g^2S\Delta[\mathscr{D},\,\gamma_5\mathscr{D}\ldots]S'. \tag{A6}$$

Since we wish to treat our equation symmetrically we use the symmetric form

$$S'=S+\tfrac{1}{2}g^2S\Delta[\mathscr{D},\,\gamma_5\overline{\mathscr{D}}]S'+\tfrac{1}{2}g^2S'\Delta[\mathscr{D},\,\gamma_5\overline{\mathscr{D}}]S \tag{A7}$$

and in the latter term $\mathscr{D}$ operates from right to left. Now to obtain the t matrix, the substitution

$$S(xy)t(y,\,\zeta\,;\,z,\,\eta)S(z,\,x')=(\delta/\delta\langle\psi(\zeta)\rangle)(\delta/\delta\langle\bar{\psi}(\eta)\rangle)S'(x,\,x') \tag{A8}$$

i.e.

$$t=S^{-1}(\delta^2/\delta\langle\bar{\psi}\rangle\delta\langle\psi\rangle)S'S. \tag{A9}$$

Applying this to (A6) and multiplying out and performing the function derivatives, one obtains

$$t=g^2\Delta+\tfrac{1}{2}\mathscr{S}(\Delta SSt)+g^2(\Delta S\{\delta^2/\delta\langle\bar{\psi}\rangle\delta\langle\psi\rangle\}t)+R \tag{A10}$$

where $\mathscr{S}$ stands for the symmetric combination of (A6), and R for radiative corrections. The remaining term, the derivative of t, is dropped in (14) and it is essentially this term which is considered in § 4.

Remarks on Crossing Symmetry†

By S. F. Edwards
Department of Mathematical Physics, University of Birmingham, England

and P. T. Matthews‡
Department of Physics, University of Rochester, Rochester, New York

[Received May 9, 1957]

Abstract

Some relations between different partial wave amplitudes due to crossing symmetry are derived for meson–nucleon scattering and some similar symmetry properties for the nucleon–nucleon interaction.

§ 1. Introduction

The Chew–Low (1956) theory of meson–nucleon scattering is based on applying the restrictions of unitarity and 'crossing' symmetry to a fixed-source interaction. Their equations have since been rederived by Oehme (1956) as the low-energy limit of dispersion relations, which also include the limitations imposed by causality. In their exact form the dispersion relations are identities, which can only be used as a check on the correct interpretation of the physical data. (By interpretation we mean the deduction of the scattering amplitude from the observed cross section.) It is only after approximation, introducing new physical information, that they become genuine equations for the scattering amplitudes. These equations are very powerful, but they always involve an integral over the whole energy range. To evaluate these integrals, or even to show that they converge, additional assumptions have to be made.

We wish to point out here, that crossing symmetry alone implies certain relations between the different partial wave amplitudes, which do not involve any integrations, and must be satisfied exactly by any theory of meson–nucleon scattering. In particular a relation between the s- and p-waves is established which indicates that the splitting between the 31 and the 13 phase shifts is of the same order as the phase shifts themselves.

We also show that a similar crossing symmetry exists for the scattering amplitude of two distinguishable fermions linked by an interaction which

† Communicated by Professor R. E. Peierls, F.R.S.

‡ On leave of absence from Department of Mathematical Physics, University of Birmingham, England.

is even under charge conjugation. The implications of insisting on this invariance in an approximate equation for the two nucleons will be discussed in a separate paper.

§ 2. Crossing in Pion–Nucleon Scattering

Suppose the meson momenta and charge label are p_1, r finally and q_1, s initially, and the nucleon momenta are p_2 finally and q_2 initially. Then crossing symmetry, which is a direct consequence of relativistic invariance and the Bose statistics of the mesons (Feldman and Matthews 1956) implies that for the scattering amplitude

$$t_{rs}(p_1, p_2, q_1, q_2)=t_{sr}(-q_1, p_2, -p_1, q_2). \quad . \quad . \quad . \quad (2.1)$$

On the energy shell

$$p_1+p_2=q_1+q_2 \quad . \quad . \quad . \quad . \quad . \quad . \quad . \quad . \quad (2.2)$$

and

$$p_1{}^2=q_1{}^2=\mu^2, \quad p_2{}^2=q_2{}^2=m^2. \quad . \quad . \quad . \quad . \quad . \quad (2.3)$$

Consequently there are only three independent 4-vectors and two independent scalar products. For discussion of crossing it is convenient to use the variables

$$\left.\begin{aligned} r_1&=(p_1+q_1)/2 \\ r_2&=(p_2+q_2)/2, \\ r_3&=(p_1-q_1)/2=(p_2-q_2)/2, \end{aligned}\right\} \quad . \quad . \quad . \quad . \quad (2.4)$$

and to take as the independent scalars

$$r_1 r_2=a, \quad r_3{}^2=b. \quad . \quad . \quad . \quad . \quad . \quad . \quad . \quad . \quad (2.5)$$

Under the crossing operation

$$a \to -a, \quad b \to b. \quad . \quad . \quad . \quad . \quad . \quad . \quad . \quad . \quad (2.6)$$

In the centre of mass coordinate system

$$\left.\begin{aligned} r_1&=\epsilon, \quad -(\mathbf{k}+\mathbf{k}')/2, \\ r_2&=\omega, \quad (\mathbf{k}+\mathbf{k}')/2, \\ r_3&=0, \quad (\mathbf{k}'+\mathbf{k})/2, \end{aligned}\right\} \quad . \quad . \quad . \quad . \quad . \quad . \quad . \quad . \quad (2.7)$$

where $2\mathbf{k}$ and $2\mathbf{k}'$ are the relative momenta in the final and initial states, ($|\mathbf{k}|=|\mathbf{k}'|$), and ϵ and ω are the corresponding nucleon and meson energies. Then

$$\left.\begin{aligned} a&=2\epsilon\omega+k^2(1+z), \\ b&=k^2(1-z), \end{aligned}\right\} \quad . \quad . \quad . \quad . \quad . \quad . \quad . \quad . \quad (2.8)$$

where

$$z=\frac{\mathbf{k} \cdot \mathbf{k}'}{k^2}.$$

The scattering amplitude may be expressed in terms of these variables, and according to (1)

$$t_{rs}(\omega, z)=t_{sr}(\omega_1, z_1), \quad . \quad . \quad . \quad . \quad . \quad . \quad . \quad . \quad (2.9)$$

where, by (6) and (8)

$$2\omega(m^2+\omega^2-\mu^2)^{1/2}+(\omega^2-\mu^2)(1+z)$$
$$=-[2\omega_1(m^2+\omega_1{}^2-\mu^2)^{1/2}+(\omega_1{}^2-\mu^2)(1+z_1)],$$

and

$$(\omega^2-\mu^2)(1-z)=(\omega_1{}^2-\mu^2)(1-z_1). \quad . \quad . \quad . \quad . \quad . \quad (2.10)$$

In the limit $m\to\infty$, these equations are satisfied by

$$\omega_1=-\omega, \quad z_1=z. \quad . \quad . \quad . \quad . \quad . \quad . \quad . \quad . \quad (2.11)$$

We thus expand in powers of $1/m$ and obtain the approximate solutions

$$\omega_1=-\omega+\frac{(\mu^2-\omega^2)(1+z)}{m-2\omega}+O(m^{-2}), \quad . \quad . \quad . \quad . \quad (2.12)$$

$$z_1=z+\frac{2\omega(1-z^2)}{m+2\omega z}+O(m^{-2}). \quad . \quad . \quad . \quad . \quad . \quad (2.13)$$

§ 3. The Partial Wave Relations

The isotopic spin projection operators are

$$P^1{}_{rs}=\tfrac{1}{3}\{\delta_{rs}+\tfrac{1}{2}[\tau_r,\tau_s]\},$$
$$P^3{}_{rs}=\tfrac{1}{3}\{2\delta_{rs}-\tfrac{1}{2}[\tau_r,\tau_s]\}.$$

Hence

$$P_{sr}{}^i=P_{rs}{}^j a^{ji} \quad \text{where}$$
$$a=\frac{1}{3}\begin{pmatrix}-1 & 4\\ 2 & 1\end{pmatrix}. \quad . \quad . \quad . \quad . \quad . \quad . \quad . \quad . \quad (3.1)$$

The angular momentum projection operators are

$$\left.\begin{aligned} S_{l+}&=\frac{1}{2l+1}[(l+1)Y_l(z)-i\sigma_n(1-z^2)Y_l{}'(z)],\\ S_{l-}&=\frac{1}{2l+1}[lY_l(z)+i\sigma_n(1-z^2)Y_l{}'(z)],\end{aligned}\right\} \quad . \quad . \quad . \quad (3.2)$$

and

$$Tr\int S_{lj}(z)S^+{}_{l'j'}(z)\,dz=\frac{(2j+1)}{(2l+1)^2}\delta_{ll'}\delta_{jj'}, \quad . \quad . \quad . \quad . \quad (3.3)$$

where Tr means the trace of the σ matrices. Then, expanding t in partial waves and using (2.9),

$$t(\omega,z)=P^i S_j(z)t_{ji}(\omega),$$
$$=P^i a^{ik}s_j{}^+(z_1)t_j{}^k(\omega_1). \quad . \quad . \quad . \quad . \quad (3.4)$$

Thus

$$s_j(z)t_j{}^i(\omega)=a^{ik}s_j{}^+(z_1)t_j{}^k(\omega_1). \quad . \quad . \quad . \quad . \quad . \quad (3.5)$$

By (3.3) to extract the j-wave part of this equation one must operate with

$$\frac{(2l+1)^2}{(2j+1)}\,Tr\int s_{lj}{}^+(z)\ldots dz, \quad . \quad . \quad . \quad . \quad . \quad . \quad (3.6)$$

giving

$$t_{lj}{}'(\omega)=\frac{(2l-1)^2}{(2j+1)}\,Tr\int s_{lj}{}^+(z)a^{il}s_{im}{}^+(z_1)t_{im}{}^k(\omega_1)\,dz. \quad . \quad . \quad (3.7)$$

Since both z_1 and ω_1 are functions of z and ω, the right-hand side of this equation involves a mixture of partial waves. If $t(\omega_1)$ is expanded as a Taylor series about the point $\omega_1=-\omega$, the integral may be evaluated.

At energies up to the resonance one may assume that only S and P waves are contributing. Let $t^i(\omega)$, $(i=1, 3)$, be the two s-wave amplitudes and $t_j{}^i(\omega)$, $(i, j=1, 3)$ be the four p-wave amplitudes. Then for the S-wave equation one obtained

$$t^i(-\omega)=a^{ik}\left[t^k(\omega)-\frac{k^2}{2m}\frac{\partial t^k}{\partial\omega}-\frac{4}{3}\frac{\omega}{m}\Pi^k-\frac{k^2}{3m}\frac{\partial\Pi^k}{\partial\omega}+O(m^{-2})\right]. \quad (3.8)$$

where
$$\Pi^k=\tfrac{1}{3}t_1{}^k+\tfrac{2}{3}t_3{}^k, \quad (3.9)$$

and for the p-wave equation

$$t_j{}^i(-\omega)=a^{ik}a_{jm}\left[t_m{}^k(\omega)-\frac{k^2}{m}\frac{\partial t_m{}^k}{\partial\omega}-\frac{k^2}{m}\frac{\partial\Sigma_m{}^k}{\partial\omega}+O(m^{-2})\right]. \quad (3.10)$$

where a_{jm} is the matrix (3.1), but now operates on the angular momentum variable and

$$\Sigma_m{}^k=t^kc_m, \quad c_m=(1, 1). \quad (3.11)$$

§ 4. Discussion

Equations (3.8) and (3.10) are our main results. Taking only the first term on the right-hand side of (3.10) gives the relation between the various p-waves in the static limit, which has been obtained previously by Chew and Low (1956). The additional term shows a further dependence upon the S-waves. If one subtracts the equation for $t_1{}^3$ from that for $t_3{}^1$ one obtains

$$t_3{}^1(+)-t_1{}^3(+)=\frac{k^2}{2m}\frac{\partial}{\partial\omega}[t_3{}^1(\omega)-t_1{}^3(\omega)+t^1(\omega)-t^3(\omega)], \quad (4.1)$$

where $t(+)$ is the even part of $t(\omega)$. If the S-waves are neglected, this is clearly consistent with the well-known degeneracy

$$t_3{}^1=t_1{}^3. \quad (4.2)$$

According to Drell *et al.* (1956) the experimental points may be approximately fitted by

$$\left.\begin{aligned}t^1(\omega)&=-0.04+0.14\omega,\\ t^3(\omega)&=-0.04-0.07\omega,\end{aligned}\right\} \quad (4.3)$$

in units of μ. Taking these values

$$t_3{}^1(+)-t_1{}^3(+)\simeq\frac{1}{2}\frac{k^2}{m\mu^2}0.21 \quad (4.4)$$

which indicates a splitting of about 1° at $k\simeq\mu$. This is of the same order of magnitude as the phase shifts themselves, and shows that these two phase shifts must be treated separately and in conjunction with the s-waves in any adequate theory.

Equation (3.8) shows how the s-waves are coupled through crossing symmetry to the derivative of the p-wave.

This investigation was originally undertaken in the hope of relating the energy dependence of the s-waves to the resonance in the (3.3) state. We have been unable to find any indication of this.

§ 5. Fermion–Fermion Crossing Symmetry

Consider the interaction of two distinguishable fermions, through an interaction which is even under charge conjugation. Then the propagation corresponding to scattering is

$$G(p_1, p_2, q_1, q_2) = \int \exp\left[-i(p_1x_1+p_2x_2-q_1y_1-q_2y_2)\right] \quad . \quad (5.1)$$
$$\langle T(\psi_1(x_1)\psi_2(x_2)\bar{\psi}_1(y_1)\bar{\psi}_2(y_2))\rangle\, d^4x_1 \ldots d^4y_2,$$
$$= \int \exp\left[-i(p_1x_1+p_2x_2-q_1y_1-q_2y_2)\right]$$
$$\langle -T(\bar{\psi}_1(y_1)\psi_2(x_2)\psi_1(x_1)\bar{\psi}_2(y_2))\rangle d^4x_1 \ldots d^4y_2 \quad . \quad . \quad . \quad (5.2)$$

Now the charge conjugate field is given by

$$\psi^1 = C\bar{\psi}, \quad \bar{\psi}^1 = C^{-1}\psi, \quad . \quad . \quad . \quad . \quad . \quad . \quad . \quad . \quad (5.3)$$

$$C^t = -C, \quad C^{-1}\gamma_\mu C = -\gamma_\mu{}^t \quad . \quad . \quad . \quad . \quad . \quad . \quad (5.4)$$

Thus, substituting for ψ_1, in terms of $\psi_1{}^1$ and interchanging the dummy variables x_1, y_1,

$$G_{\alpha\beta}(p_1, p_2, q_1, q_2) = \int \exp\left[-i(q_1x_1+p_2x_2+p_1y_1-q_2y_2)\right]$$
$$C'_{\alpha\beta}\langle T(\psi_1'(x_1), \psi_2(x_2)\bar{\psi}_1'(y_1)\psi_2(y_2))\rangle C^{-1}{}_\beta\, d^4x_1 \ldots d^4y_2$$
$$= [C_1{}^{-1}\bar{G}^{t(1)}(-q_1, p_2, -p_1, q_2)C_1]^{t(1)} \quad . \quad . \quad . \quad . \quad (5.5)$$

where $t(1)$ implies the spinor transpose with respect to particle 1 and G denotes that particle 1 has been replaced by its anti-particle.

However for even interactions the anti-particle interactions are the same as the particle interactions. Thus, using (4.4) we have

$$G(p_1, p_2, q_1, q_2, \gamma^{(1)}, \gamma^{(2)})$$
$$= G^{t(1)}(-q_1, p_2, -p_1, q_2, -\gamma(1)^t, \gamma(2)). \quad . \quad . \quad . \quad (5.6)$$

The effect of the double tranpose is to reverse the order of all the (1) factors.

In terms of the variables defined in § 2, this reads

$$G(r_1, r_2, r_3, \gamma(1), \gamma(2))$$
$$= G^{t(1)}(-r_1, r_2, r_3, -\gamma(1)^t, \gamma^{(2)}) \quad . \quad . \quad . \quad . \quad . \quad (5.7)$$

Insisting on this invariance in approximate equations brings the theory much nearer to a form which allows non-relativistic and no-recoil limits to be taken correctly. This will be discussed in detail in a separate paper.

After this manuscript was completed the author's attention was drawn to some similar considerations by F. E. Low (1956), the results of which were reported at the International Conference in Pisa.

References

Chew, G. F., and Low, F. E., 1956, *Phys. Rev.*, **101,** 1570.
Drell, S. D., Friedman, M. H., and Zachariasen, F., 1956, *Phys. Rev.*, **104,** 236.
Feldman, G., and Matthews, P. T., 1956, *Phys. Rev.*, **101,** 1212.
Low, F. E., 1956, *Nuovo Cim.*, Suppl. **2,** 767.
Oehme, R., 1955, *Phys. Rev.* **100,** 1503; 1956, *Ibid.*, **102,** 1174.

The Thermal Instability of a Rotating Fluid Sphere Heated Within†

By S. Chandrasekhar, F.R.S.
University of Chicago

[Received March 21, 1957]

Summary

In this paper the problem of the thermal instability of an incompressible rotating fluid sphere heated within is considered. The equations governing the state of marginal instability are derived for the case when the motions and the associated perturbations have symmetry about the axis of rotation. The underlying characteristic value problem is solved for a slightly modified set of boundary conditions. Nevertheless, the solution obtained suffices to determine the general nature of the dependence of the lowest Rayleigh number for the onset of instability on the Taylor number $T(=4\Omega^2R^4/\nu^2)$.

§ 1. Introduction

In recent years the onset of thermal instability in horizontal layers of fluid heated from below has been investigated both theoretically and experimentally under a wide variety of conditions (Chandrasekhar 1952 a, 1953 a, 1954 a, b, 1956 a, Chandrasekhar and Elbert 1955, Fultz and Nakagawa 1955, Nakagawa 1957). These studies have disclosed a number of novel features: the onset of thermal instability as oscillations of increasing amplitude (i.e. as overstability) when a metallic liquid such as mercury is subject to Coriolis acceleration, and the conflicting nature of the effects of rotation and magnetic field when they act simultaneously. While these studies have been useful in thus drawing attention to the different types of phenomena one may encounter when rotation and magnetic field are present, it is important for applications to problems such as convection in the earth's core that the relevant investigations are extended to a spherical geometry. The simplest problem in this latter category, that of the thermal instability of a fluid sphere heated within, has indeed been investigated (e.g. Wasiutynski 1946, Jeffreys and Bland 1951, Chandrasekhar 1952 b, 1953 b, Backus 1955); but the extension to the case of a rotating sphere or when a magnetic field is present raises mathematical difficulties of a different order from those encountered in the

† Communicated by the Author.

solution of the corresponding plane problems. The reasons for the increased difficulty are principally two: first, while the physical circumstances, at best, allow only symmetry about an axis, the boundary conditions are specified on a sphere; and second, it does not appear that the problems can be solved by variational techniques such as those which enabled the solution of the plane problems.

The present paper is devoted to the problem of the thermal instability of a rotating fluid sphere with internal heat sources. The manner in which the solution is obtained in one very special case may be suggestive of methods one might adopt for the solution of more difficult problems.

§ 2. The Equations of the Problem

We shall consider a homogeneous sphere of radius R rotating with an angular velocity Ω about the z-axis and with a uniform distribution of heat sources such that in the absence of conduction the temperature at each point will rise at the rate ϵ. In treating this problem we shall ignore the rotational flattening of the sphere: this is justified in our present context, since the principal effect we are seeking is that of the Coriolis-acceleration term, $2\mathbf{u}\times\mathbf{\Omega}$, in the equation of motion: for this purpose the small departure of the equilibrium configuration from a sphere is not essential.

The temperature distribution in the equilibrium state is given by (Chandrasekhar 1952 b, eqn. (2): this paper will be referred to hereafter as I)

$$T=\beta(R^2-r^2), \quad \beta=\epsilon\, 6\kappa, \qquad \ldots\ldots (1)$$

where κ is the coefficient of thermometric conductivity. Under these circumstances, the equation governing small departures from the initial stationary state are (cf. I, eqns. (11), (13) and (14)):

$$\frac{\partial\theta}{\partial t}=\kappa\nabla^2\theta+2\beta\mathbf{u}\,.\,\mathbf{r} \qquad \ldots\ldots\ldots (2)$$

and

$$\frac{\partial\mathbf{u}}{\partial t}=-\operatorname{grad}\delta\varpi+\gamma\theta\mathbf{r}-\nu\operatorname{curl}^2\mathbf{u}+2\Omega\mathbf{u}\times\mathbf{l}_z \qquad \ldots (3)$$

where ν denotes the coefficient of kinematic viscosity, ρ the density, $\mathbf{u}$ the velocity, θ and δp are the perturbations in the temperature and pressure respectively, $\delta\varpi=\delta p/\rho$ and $\mathbf{l}_z$ is a unit vector along the axis of rotation, and

$$\gamma=\frac{4}{3}\pi G\alpha\rho. \qquad \ldots\ldots\ldots (4)$$

In eqn (4), G is the constant of gravitation and α is the coefficient of volume expansion. In addition we have the condition

$$\operatorname{div}\mathbf{u}=0, \qquad \ldots\ldots\ldots (5)$$

on the velocity field.

§ 3. The Equations Governing Marginal Stability in case the Velocity Field has Axial Symmetry

In this paper we shall restrict our consideration to the case when the instability sets in as a stationary pattern of convection. In this case the equations governing marginal stability are:

$$\kappa\nabla^2\theta=-2\beta\mathbf{u}\cdot\mathbf{r} \quad . \quad . \quad . \quad . \quad . \quad . \quad . \quad . \quad (6)$$

and

$$\text{grad}\,\delta\varpi=\gamma\theta\mathbf{r}-\nu\,\text{curl}^2\,\mathbf{u}+2\Omega\mathbf{u}\times\mathbf{l}_z. \quad . \quad . \quad . \quad . \quad (7)$$

In the further discussion of these equations we shall assume that the velocity field as well as the distribution of θ have symmetry about the z-axis.

If the velocity field is divergence free and has axial symmetry, we can express it as a superposition of a poloidal and a toroidal field in terms of two scalars; thus (cf. Lüst and Schlüter 1954, Chandrasekhar 1956 b, c):

$$\mathbf{u}=\mathbf{l}_z\times\mathbf{r}\,U-\text{curl}\,(\mathbf{l}_z\times\mathbf{r}\,V), \quad . \quad . \quad . \quad . \quad . \quad . \quad (8)$$

where U and V are two scalar functions which are azimuth independent. The physical interpretation of these two scalars is the following: U defines motions which are entirely in the meridional planes and V defines motions which are entirely rotational.

The particular advantage of the representation (8) in the present connection is that we can write down without any difficulty the result of the operation, any number of times, of curl on $\mathbf{u}$. Thus (cf. Chandrasekhar 1956 b, eqn. (18))

$$\text{curl}\,\mathbf{u}=-\mathbf{l}_z\times\mathbf{r}\Delta_5 U+\text{curl}\,(\mathbf{l}_z\times\mathbf{r}V), \quad . \quad . \quad . \quad . \quad (9)$$

where Δ_5 is the Laplacian operator for axisymmetric functions in five dimensional Euclidean space: by repeated applications of this formula we obtain

$$\text{curl}^2\,\mathbf{u}=-\mathbf{l}_z\times\mathbf{r}\Delta_5 V-\text{curl}\,(\mathbf{l}_z\times\mathbf{r}\Delta_5 U), \quad . \quad . \quad . \quad (10)$$

$$\text{curl}^3\,\mathbf{u}=+\mathbf{l}_z\times\mathbf{r}\Delta_5{}^2 U-\text{curl}\,(\mathbf{l}_z\times\mathbf{r}\Delta_5 V), \quad . \quad . \quad . \quad (11)$$

etc.

Returning to eqns. (6) and (7), we first eliminate $\delta\varpi$ by taking the curl of eqn. (7). We thus obtain

$$\gamma\,\text{grad}\,\theta\times\mathbf{r}-\nu\,\text{curl}^3\,\mathbf{u}+2\Omega\,\text{curl}\,(\mathbf{u}\times\mathbf{l}_z)=0. \quad . \quad . \quad . \quad (12)$$

It can be readily verified that

$$\text{grad}\,\theta\times\mathbf{r}=\mathbf{l}_z\times\mathbf{r}\left(\frac{\partial\theta}{\partial z}-\frac{z}{\varpi}\frac{\partial\theta}{\partial\varpi}\right), \quad . \quad . \quad . \quad . \quad (13)$$

where $\varpi[=\sqrt{(x^2+y^2)}]$ is the distance of a point from the axis of symmetry; also,

$$\text{curl}\,(\mathbf{u}\times\mathbf{l}_z)=\mathbf{l}_z\times\mathbf{r}\frac{\partial V}{\partial z}+\text{curl}\left(\mathbf{l}_z\times\mathbf{r}\frac{\partial U}{\partial z}\right). \quad . \quad . \quad . \quad (14)$$

Making use of eqns. (11), (13) and (14), we can rewrite, eqn. (12) in the form

$$\mathbf{l}_z\times\mathbf{r}\,\gamma\left(\frac{\partial\theta}{\partial z}-\frac{z}{\varpi}\frac{\partial\theta}{\partial\varpi}\right)-\nu\{\mathbf{l}_z\times\mathbf{r}\Delta_5{}^2U-\mathrm{curl}\,(\mathbf{l}_z\times\mathbf{r}\Delta_5 V)\}$$
$$+2\Omega\left\{\mathbf{l}_z\times\mathbf{r}\frac{\partial V}{\partial z}+\mathrm{curl}\left(\mathbf{l}_z\times\mathbf{r}\frac{\partial U}{\partial z}\right)\right\}=0. \quad . \quad . \quad . \quad (15)$$

The poloidal and the toroidal fields represented in this equation must separately vanish. Thus, we must have

$$\Delta_5{}^2U-\frac{2\Omega}{\nu}\frac{\partial V}{\partial z}=\frac{\gamma}{\nu}\left(\frac{\partial}{\partial z}-\frac{z}{\varpi}\frac{\partial}{\partial\varpi}\right)\theta \quad . \quad . \quad . \quad . \quad (16)$$

and

$$\Delta_5 V+\frac{2\Omega}{\nu}\frac{\partial U}{\partial z}=0. \quad . \quad . \quad . \quad . \quad . \quad (17)$$

Now applying the operator Δ_5 to eqn. (16), we have

$$\Delta_5{}^3U-\frac{2\Omega}{\nu}\frac{\partial}{\partial z}\Delta_5 V=\frac{\gamma}{\nu}\Delta_5\left(\frac{\partial}{\partial z}-\frac{z}{\varpi}\frac{\partial}{\partial\varpi}\right)\theta, \quad . \quad . \quad . \quad (18)$$

since the operations Δ_5 and $\partial/\partial z$ permute. Eliminating V from this last equation by making use of eqn. (17), we obtain

$$\Delta_5{}^3U+\frac{4\Omega^2}{\nu^2}\frac{\partial^2U}{\partial z^2}=\frac{\gamma}{\nu}\Delta_5\left(\frac{\partial}{\partial z}-\frac{z}{\varpi}\frac{\partial}{\partial\varpi}\right)\theta. \quad . \quad . \quad . \quad (19)$$

It may be readily verified that

$$\Delta_5\left(\frac{\partial}{\partial z}-\frac{z}{\varpi}\frac{\partial}{\partial\varpi}\right)=\left(\frac{\partial}{\partial z}-\frac{z}{\varpi}\frac{\partial}{\partial\varpi}\right)\Delta_3, \quad . \quad . \quad . \quad . \quad (20)$$

where Δ_3 is the usual three dimensional Laplacian for axisymmetric functions. By making use of eqn. (6), we may therefore rewrite the right-hand side of eqn. (19) in the manner :

$$-\frac{2\beta\gamma}{\kappa\nu}\left(\frac{\partial}{\partial z}-\frac{z}{\varpi}\frac{\partial}{\partial\varpi}\right)\mathbf{u}\,.\,\mathbf{r}. \quad . \quad . \quad . \quad . \quad . \quad . \quad (21)$$

On the other hand, according to eqn. (8)

$$\mathbf{u}\,.\,\mathbf{r}=-\left(\frac{\partial}{\partial z}-\frac{z}{\varpi}\frac{\partial}{\partial\varpi}\right)\varpi^2U. \quad . \quad . \quad . \quad . \quad . \quad (22)$$

Equation (19) thus reduces to

$$\Delta_5{}^3U+\frac{4\Omega^2}{\nu^2}\frac{\partial^2U}{\partial z^2}=\frac{2\beta\gamma}{\kappa\nu}\left(\frac{\partial}{\partial z}-\frac{z}{\varpi}\frac{\partial}{\partial\varpi}\right)^2\varpi^2U. \quad . \quad . \quad . \quad (23)$$

In spherical polar coordinates ($\mu=\cos\vartheta$, φ) eqn. (23) takes the form

$$\Delta_5{}^3U+\frac{4\Omega^2}{\nu^2}\left(\mu\frac{\partial}{\partial r}+\frac{1-\mu^2}{r}\frac{\partial}{\partial\mu}\right)^2U=\frac{2\beta\gamma}{\kappa\nu}\frac{\partial^2}{\partial\mu^2}[(1-\mu^2)U], \quad . \quad (24)$$

where, now

$$\Delta_5=\frac{\partial^2}{\partial r^2}+\frac{4}{r}\frac{\partial}{\partial r}+\frac{1-\mu^2}{r^2}\frac{\partial^2}{\partial\mu^2}-\frac{4\mu}{r^2}\frac{\partial}{\partial\mu}. \quad . \quad . \quad . \quad . \quad (25)$$

Similarly, eqns. (16) and (17) take the forms

$$\Delta_5{}^2 U - \frac{2\Omega}{\nu}\left(\mu\frac{\partial}{\partial r}+\frac{1-\mu^2}{r}\frac{\partial}{\partial\mu}\right)V=\frac{\gamma}{\nu}\frac{1}{r}\frac{\partial\theta}{\partial\mu}, \quad . \quad . \quad . \quad (26)$$

and

$$\Delta_5 V+\frac{2\Omega}{\nu}\left(\mu\frac{\partial}{\partial r}+\frac{1-\mu^2}{r}\frac{\partial}{\partial\mu}\right)U=0. \quad . \quad . \quad . \quad . \quad (27)$$

Also, it may be noted here that

$$\mathbf{u}=-\frac{\partial}{\partial\mu}[(1-\mu^2)U]\mathbf{l}_r-\frac{(1-\mu^2)^{1/2}}{r}\frac{\partial}{\partial r}(r^2U)\mathbf{l}_\vartheta+r(1-\mu^2)^{1/2}V\mathbf{l}_\varphi, \quad (28)$$

where $\mathbf{l}_r$, $\mathbf{l}_\vartheta$ and $\mathbf{l}_\varphi$ are unit vectors along the arcs dr, $r\,d\vartheta$ and $r\sin\vartheta\,d\varphi$ in the three principal directions.

3.1. *Boundary Conditions*

Solutions of eqns. (24), (26) and (27) must be sought which satisfy certain boundary conditions. These depend on the nature of the bounding surface at $r=R$: but in all cases θ and the component of $\mathbf{u}$ in the direction $\mathbf{l}_r$ must vanish. According to eqns. (26) and (28) these latter conditions require:

$$U=0 \text{ and } \Delta_5{}^2 U-\frac{2\Omega}{\nu}\left(\mu\frac{\partial}{\partial r}+\frac{1-\mu^2}{r}\frac{\partial}{\partial\mu}\right)V=0 \text{ on } r=R. \quad (29)$$

If the bounding surface $r=R$ is rigid and no slip occurs here, then the components u_ϑ and u_φ of $\mathbf{u}$ along $\mathbf{l}_\vartheta$ and $\mathbf{l}_\varphi$ must also vanish. From eqn. (28), it follows that the vanishing of these additional components of $\mathbf{u}$ at $r=R$ require

$$\frac{\partial U}{\partial r}=0 \text{ and } V=0 \text{ on } r=R \text{ (rigid surface)}. \quad . \quad . \quad . \quad (30)$$

(Actually, the vanishing of u_ϑ requires only that $\partial(r^2U)/\partial r=0$; since, however $U=0$ at the boundary, the condition on U stated follows.) On the other hand, if the bounding surface should be free, then the vanishing of the tangential viscous stresses on this surface requires (I, eqn. (21))

$$\frac{\partial}{\partial r}\left(\frac{u_\vartheta}{r}\right)=\frac{\partial}{\partial r}\left(\frac{u_\varphi}{r}\right)=0. \quad . \quad . \quad . \quad . \quad . \quad . \quad (31)$$

According to eqn. (28) these conditions are equivalent to

$$\left.\begin{aligned}&\frac{\partial}{\partial r}\left[\frac{1}{r^2}\frac{\partial}{\partial r}(r^2U)\right]=\frac{\partial^2U}{\partial r^2}+\frac{2}{r}\frac{\partial U}{\partial r}-\frac{2U}{r^2}=0,\\ \text{and}\\ &\frac{\partial V}{\partial r}=0 \qquad \text{on } r=R.\end{aligned}\right\} \quad . \quad . \quad . \quad (32)$$

Since $U=0$ on $r=R$, the first of these conditions can also be expressed as

$$\frac{\partial^2}{\partial r^2}(rU)=0. \quad . \quad . \quad . \quad . \quad . \quad . \quad . \quad . \quad (33)$$

Collecting the foregoing conditions, we may write

$$U=0, \quad \frac{\partial U}{\partial r}=0, \quad V=0 \text{ and } \Delta_5^2 U-\frac{2\Omega}{\nu}\mu\frac{\partial V}{\partial r}=0, \quad . \quad . \quad (34)$$

on a rigid bounding surface, and

$$U=0, \quad \frac{\partial^2}{\partial r^2}(rU)=0, \quad \frac{\partial V}{\partial r}=0 \text{ and } \Delta_5^2 U-\frac{2\Omega}{\nu}\frac{1-\mu^2}{r}\frac{\partial V}{\partial \mu}=0, \quad . \quad (35)$$

on a free bounding surface. Finally, we may note that if we measure distances in units of the radius of the configuration, we may rewrite eqns. (24) and (27) in the forms:

$$\Delta_5^3 U+T\frac{\partial^2 U}{\partial z^2}=C\frac{\partial^2}{\partial \mu^2}[(1-\mu^2)U], \quad . \quad . \quad . \quad . \quad (36)$$

and

$$\Delta_5 V=-\frac{2\Omega}{\nu}R\frac{\partial U}{\partial z}, \quad . \quad . \quad . \quad . \quad . \quad . \quad . \quad (37)$$

where

$$T=\frac{4\Omega^2}{\nu^2}R^4 \text{ and } C=\frac{2\beta\gamma}{\kappa\nu}R^6, \quad . \quad . \quad . \quad . \quad . \quad (38)$$

are the Taylor and the Rayleigh numbers, respectively.

§ 4. The Solution of the Characteristic Value Problem for a Special Case

It does not appear that the characteristic value problem presented by eqns. (24) to (27) together with the boundary conditions (34) or (35) can be solved in any simple way. In particular, it does not appear that the problem can be solved by a variational method. However, since our principal interest is in the asymptotic dependence of C on the Taylor number T, the following method of obtaining this dependence suggests itself.

From our experience with the plane problems we may feel assured that as a general rule the *nature* of the dependence of the critical Rayleigh number on auxiliary parameters such as T (to allow for the effects of Coriolis acceleration) or Q (to allow for the effects of a magnetic field) is largely independent of the boundary conditions with respect to which the underlying characteristic value problem may have been solved: indeed, in all cases which have been examined the asymptotic dependences on parameters such as T and Q are the same for solutions satisfying very different boundary conditions. Consequently, it would appear that we may seek solutions for the spherical problems also with the boundary conditions slightly modified so as to allow a simpler solution of the characteristic value problem; this will be permissible, if our particular concern is to discover the nature of the dependence of C on the Taylor number, for example.

Thus, if we should consider the problem without rotation (treated in I) we are required to seek solutions of the equation (in our present notation)

$$\Delta_5{}^3U = C\frac{\partial^2}{\partial\mu^2}(1-\mu^2)U, \qquad \ldots\ldots \quad (39)$$

together with the boundary conditions

$$U=0, \quad \Delta_5{}^2U=0 \quad (r=1)$$

and

$$\textit{either } \frac{\partial U}{\partial r}=0 \quad \textit{or} \quad \frac{\partial^2}{\partial r^2}(rU)=0 \quad (r=1), \qquad \ldots\ldots \quad (40)$$

depending on whether the bounding sphere is rigid or free. Solutions appropriate for these boundary conditions have been obtained by variational methods in I. However, for the slightly modified boundary conditions

$$U=0, \quad \frac{\partial^2 U}{\partial r^2}+\frac{4}{r}\frac{\partial U}{\partial r}=0 \quad \text{and} \quad \Delta_5{}^2U=0, \qquad \ldots \quad (41)$$

the problem admits of an explicit solution. For (Chandrasekhar 1956 d, eqn. (36))

$$U=T_{n,j}=\frac{J_{n+3/2}(\alpha_{j,n}r)}{r^{3/2}}C_n{}^{3/2}(\mu), \qquad \ldots\ldots \quad (42)$$

where $\alpha_{j,n}$ is the jth zero of the Bessel function $J_{n+3/2}(x)$ and $C_n{}^{3/2}(\mu)$ is the Gegenbauer polynomial, satisfies the boundary conditions (41) and represents a solution of eqn. (39) provided

$$\alpha^6_{j,n}=(n+1)(n+2)C. \qquad \ldots\ldots \quad (43)$$

If we compare this formula for C with that given in I (eqn. (81); note that the order of the spherical harmonic l in this equation is related to the order of the Gegenbauer polynomial, n, by $l=n+1$) we observe that the present solution predicts the same general dependence of C on the order n as that obtained in I for solutions satisfying the correct boundary conditions; moreover, the asymptotic dependence of C on n for $n\to\infty$ is the same for all three boundary conditions (namely,

$$\partial U/\partial r=0, \quad \partial^2(r^2U)/\partial r^2=0 \text{ and } \partial^2(r^4U)/\partial r^2=0).$$

For the reasons stated, we shall seek a solution of the equation

$$\Delta_5{}^3U+T\frac{\partial^2 U}{\partial z^2}=C\frac{\partial^2}{\partial\mu^2}(1-\mu^2)U, \qquad \ldots\ldots \quad (44)$$

which satisfies the boundary conditions

$$U=0, \quad \frac{\partial^2 U}{\partial r^2}+\frac{4}{r}\frac{\partial U}{\partial r}=0 \text{ and } \theta=0 \text{ on } r=1. \qquad \ldots \quad (45)$$

We can satisfy the boundary conditions on U by expanding it in terms of the various modes $T_{n,j}$ (which it may be noted here form a complete set of orthogonal functions); thus,

$$U=\sum_{n,j}A_{n,j}T_{n,j}. \qquad \ldots\ldots\ldots \quad (46)$$

When the characteristic value C has been determined by this substitution for U, we shall also have satisfied the boundary condition on θ: for, according to eqns. (24), (26) and (27)

$$\mathcal{A}_5\left(\frac{1}{r}\frac{\partial\theta}{\partial\mu}\right)=\frac{2\beta}{\kappa}\frac{\partial^2}{\partial\mu^2}(1-\mu^2)U\,; \quad . \quad . \quad . \quad . \quad . \quad (47)$$

when U has the form (46), this equation becomes

$$\mathcal{A}_5\left(\frac{1}{r}\frac{\partial\theta}{\partial\mu}\right)=-\frac{2\beta}{\kappa}\sum_{n,j}A_{n,j}(n+1)(n+2)T_{n,j}, \quad . \quad . \quad . \quad (48)$$

and the required solution of this equation is

$$\begin{aligned}\frac{1}{r}\frac{\partial\theta}{\partial\mu}&=\frac{2\beta}{\kappa}\sum_{n,j}\frac{A_{n,j}}{\alpha^2{}_{j,n}}(n+1)(n+2)T_{n,j}\\&=-\frac{2\beta}{\kappa}\sum_{n,j}\frac{A_{n,j}}{\alpha^2{}_{j,n}}\frac{J_{n+3/2}(\alpha_{j,n}r)}{r^{3/2}}\frac{d^2}{d\mu^2}[(1-\mu^2)C^{3/2}{}_n(\mu)] \quad . \quad (49)\end{aligned}$$

or

$$\theta=-\frac{2\beta}{\kappa}\sum_{n,j}\frac{A_{n,j}}{\alpha^2{}_{j,n}}\frac{J_{n+3/2}(\alpha_{j,n}r)}{r^{1/2}}\frac{d}{d\mu}[(1-\mu^2)C^{3/2}{}_n(\mu)], \quad . \quad (50)$$

and this clearly vanishes on $r=1$.

Returning to the solution of eqn. (44) together with the boundary conditions (43), we first observe that the results of applying the operators $\mathcal{A}_5{}^3$ and $\partial^2(1-\mu^2)/\partial\mu$ to U given by eqn. (46) are:

$$\mathcal{A}_5{}^3U=-\sum_{n,j}A_{n,j}\alpha^6{}_{j,n}T_{n,j} \quad . \quad . \quad . \quad . \quad . \quad (51)$$

and

$$\frac{\partial^2}{\partial\mu^2}[(1-\mu^2)U]=-\sum_{n,j}A_{n,j}(n+1)(n+2)T_{n,j}. \quad . \quad . \quad (52)$$

The effect of the operator $\partial^2/\partial z^2$ on $T_{n,j}$ is not so simple. By using the various recurrence relations satisfied by the Bessel functions and the Gegenbauer polynomials, we can show that

$$\frac{\partial T_{n,j}}{\partial z}=f_{n,j}(r)C^{3/2}{}_{n+1}(\mu)+g_{n,j}(r)C^{3/2}{}_{n-1}(\mu) \quad . \quad . \quad . \quad (53)$$

and

$$\frac{\partial^2 T_{n,j}}{\partial z^2}=L_{n,j}(r)C^{3/2}{}_{n+2}(\mu)+M_{n,j}(r)C^{3/2}{}_n(\mu)+N_{n,j}(r)C^{3/2}{}_{n-2}(\mu), \quad (54)$$

where

$$f_{n,j}=\frac{n+1}{2n+3}\left[\frac{d}{dr}\left(\frac{J_{n+3/2}(\alpha_{j,n}r)}{r^{3/2}}\right)-n\frac{J_{n+3/2}(\alpha_{j,n}r)}{r^{5/2}}\right], \quad . \quad . \quad . \quad (55)$$

$$g_{n,j}=\frac{n+2}{2n+3}\left[\frac{d}{dr}\left(\frac{J_{n+3/2}(\alpha_{j,n}r)}{r^{3/2}}\right)+(n+3)\frac{J_{n+3/2}(\alpha_{j,n}r)}{r^{5/2}}\right], \quad . \quad (56)$$

$$L_{n,j}=-(n+2)\left[\frac{f_{n,j}}{r}+\frac{(n+1)\alpha^2{}_{j,n}}{(2n+3)(2n+5)}\frac{J_{n+3/2}(\alpha_{j,n}r)}{r^{3/2}}\right], \quad . \quad . \quad (57)$$

$$M_{n,j}=-\frac{(2n^2+6n+1)\alpha^2{}_{j,n}}{(2n+1)(2n+5)}\frac{J_{n+3/2}(\alpha_{j,n}r)}{r^{3/2}}, \quad . \quad . \quad . \quad . \quad . \quad . \quad (58)$$

$$N_{n,j}=+(n+1)\left[\frac{g_{n,j}}{r}-\frac{(n+2)\alpha^2_{j,n}}{(2n+1)(2n+3)}\frac{J_{n+3/2}(\alpha_{j,n}r)}{r^{3/2}}\right]. \quad . \quad (59)$$

The functions $f_{n,j}$, $g_{n,j}$, $L_{n,j}$ and $N_{n,j}$ have recently been tabulated by Donna Elbert (1957).

Substituting from eqns. (51), (52) and (54) in eqn. (44) we obtain

$$\sum_{n,j}A_{n,j}\{-\alpha^6_{j,n}+(n+1)(n+2)C\}\frac{J_{n+3/2}(\alpha_{j,n}r)}{r^{3/2}}C^{3/2}_n(\mu)$$
$$+T\sum_{m,k}A_{m,k}(L_{m,k}C^{3/2}_{m+2}+M_{m,k}C^{3/2}_m+N_{m,k}C^{3/2}_{m-2})=0. \quad (60)$$

Equating the terms in the Gegenbauer polynomials $C^{3/2}_n$, we obtain (cf. eqn. (58))

$$\sum_j A_{n,j}\left\{-\alpha^6_{j,n}-(n+1)(n+2)C-\frac{2n^2+6n+1}{(2n+5)(2n+1)}\alpha^2_{j,n}T\right\}J_{n+3/2}(\alpha_{j,n}r)$$
$$+T\sum_k(A_{n-2,k}L_{n-2,k}+A_{n+2,k}N_{n+2,k})r^{3/2}=0. \quad . \quad . \quad . \quad (61)$$

Multiplying this last equation by $rJ_{n+3/2}(\alpha_{j,n}r)$ and integrating from 0 to 1 and making use of the orthogonality relation,

$$\int_0^1 rJ_{n+3/2}(\alpha_{j,n}r)J_{n+3/2}(\alpha_{k,n}r)\,dr=\tfrac{1}{2}[J'_{n+3/2}(\alpha_{j,n})]^2\delta_{j,k}, \quad . \quad (62)$$

we obtain

$$\tfrac{1}{2}[J'_{n+3/2}(\alpha_{j,n})]^2A_{n,j}\left\{-\alpha^6_{j,n}-\alpha^2_{j,n}\frac{2n^2+6n+1}{(2n+5)(2n+1)}T+(n+1)(n+2)C\right\}$$
$$+T\sum_{k=1}^{\infty}\{A_{n-2,k}\langle n-2\,;\,k\,|\,n\,;\,j\rangle+A_{n+2,k}\langle n+2\,;\,k\,|\,n\,;\,j\rangle\}=0 \quad . \quad (63)$$

where

$$\left.\begin{aligned}\langle n-2\,;\,k\,|\,n\,;\,j\rangle&=\int_0^1 r^{5/2}L_{n-2,k}J_{n+3/2}(\alpha_{j,n}r)\,dr,\\ \text{and}\qquad\\ \langle n+2\,;\,k\,|\,n\,;\,j\rangle&=\int_0^1 r^{5/2}N_{n+2,k}J_{n+3/2}(\alpha_{j,n}r)\,dr,\end{aligned}\right\} \quad . \quad . \quad (64)$$

denote the matrix elements which have to be evaluated numerically.

Equation (63) leads to the following determinantal equation for the characteristic root C:

$$\Big\|T\{\langle n-2\,;\,k\,|\,n\,;\,j\rangle+\langle n+2\,;\,k\,|\,n\,;\,j\rangle\}$$
$$-\tfrac{1}{2}[J'_{n+3/2}(\alpha_{j,n})]^2\delta_{m,n}\delta_{j,k}$$
$$\times\left\{\alpha^6_{j,n}+\alpha^2_{j,n}\frac{2n^2+6n+1}{(2n+5)(2n+1)}T-(n+1)(n+2)C\right\}\Big\|=0. \quad (65)$$

From eqn. (65) it follows that

$$(n+1)(n+2)C\to\alpha^6_{j,n}\left[1+\frac{2n^2+6n+1}{(2n+5)(2n+1)}\frac{T}{\alpha^4_{j,n}}\right] \quad (T\to 0). \quad (66)$$

Table 1. The Basic Matrix

	(0, 1)	(0, 2)	(0, 3)	(2, 1)	(2, 2)	(2, 3)
(0, 1)	$-8{\cdot}231064\times10^{3}$ $-4{\cdot}038146\,T$ $+2C$	0	0	$+2{\cdot}88748\,T$	$+10{\cdot}1553\,T$	$-1{\cdot}87557\,T$
(0, 2)	0	$-2{\cdot}125572\times10^{5}$ $-11{\cdot}93590\,T$ $+2C$	0	$-1{\cdot}97847\,T$	$+4{\cdot}76659\,T$	$+26{\cdot}7449\,T$
(0, 3)	0	0	$-1{\cdot}680909\times10^{6}$ $-23{\cdot}77998\,T$ $+2C$	$+1{\cdot}6959\,T$	$-2{\cdot}9568\,T$	$+6{\cdot}5665\,T$
(2, 1)	$+1{\cdot}902918\,T$	$-0{\cdot}782806\,T$	$+0{\cdot}479433\,T$	$-1{\cdot}164373\times10^{5}$ $-22{\cdot}78789\,T$ $+12C$	0	0
(2, 2)	$+9{\cdot}240749\,T$	$+2{\cdot}60411\,T$	$-1{\cdot}15397\,T$	0	$-1{\cdot}277867\times10^{6}$ $-50{\cdot}64097\,T$ $+12C$	0
(2, 3)	$-2{\cdot}1891\,T$	$+18{\cdot}74192\,T$	$+3{\cdot}28717\,T$	0	0	$-6{\cdot}606133\times10^{6}$ $-87{\cdot}56339\,T$ $+12C$

A method of solving the infinite order characteristic equation which eqn. (65) provides for C would be to set the determinant formed by the first few rows and columns of the matrix on the left-hand side of eqn. (65) equal to zero and let the order of the determinant take increasingly larger values.

Table 2. The Characteristic Numbers C for the Onset of the Lowest Mode of Instability for Various Values of the Taylor Number

T	1st Approx.	2nd Approx.	4th Approx.	6th Approx.
0	$4{\cdot}116\times10^{3}$	$4{\cdot}116\times10^{3}$	$4{\cdot}116\times10^{3}$	—
1000	$6{\cdot}135\times10^{3}$	$6{\cdot}093\times10^{3}$	$6{\cdot}056\times10^{3}$	—
2000	$8{\cdot}154\times10^{3}$	$7{\cdot}988\times10^{3}$	$7{\cdot}846\times10^{3}$	—
4000	$1{\cdot}219\times10^{4}$	$1{\cdot}155\times10^{4}$	$1{\cdot}105\times10^{4}$	—
6000	$1{\cdot}623\times10^{4}$	$1{\cdot}490\times10^{4}$	$1{\cdot}389\times10^{4}$	$1{\cdot}388\times10^{4}$
8000	$2{\cdot}027\times10^{4}$	$1{\cdot}811\times10^{4}$	$1{\cdot}650\times10^{4}$	$1{\cdot}648\times10^{4}$
10000	—	$2{\cdot}124\times10^{4}$	$1{\cdot}894\times10^{4}$	$1{\cdot}892\times10^{4}$
20000	—	—	$2{\cdot}970\times10^{4}$	$2{\cdot}962\times10^{4}$
50000	—	—	$5{\cdot}583\times10^{4}$	$5{\cdot}557\times10^{4}$
70000	—	—	$7{\cdot}137\times10^{4}$	$7{\cdot}098\times10^{4}$
100000	—	—	$9{\cdot}371\times10^{4}$	$9{\cdot}313\times10^{4}$
200000	—	—	$1{\cdot}655\times10^{5}$	$1{\cdot}642\times10^{5}$
1000000	—	—	$7{\cdot}267\times10^{5}$	$7{\cdot}196\times10^{5}$

From eqn. (65) it is clear that the solutions separate into two non-combining groups: those which include the even and those which include the odd orders of the Gegenbauer polynomials. By restricting oneself to determinants of order less than or equal to six by including the terms of orders $n=0$ and 2 in the Gegenbauer polynomials and the first three zeros of the Bessel functions $J_{3/2}(x)$ and $J_{7/2}(x)$ it appears that one can determine the lowest characteristic root for C with sufficient precision for $T\leqslant10^{6}$. The secular matrix including the elements for $n=0$, 2 and $j=1$, 2 and 3 is given in table 1. In table 2, the roots determined in the manner described are listed: the corresponding coefficients $A_{n,j}$ in the expansion for U are given in table 3. An examination of this table indicates that the values of C have been determined to an accuracy of the order of 1%. The results are further illustrated in the figure.

It is apparent from the figure and table 2 that rotation can be a decisive factor in inhibiting thermal convection in a fluid sphere. Indeed, the numerical evidence points to the proportionality

$$C\rightarrow\text{constant}\times T\text{ as }T\rightarrow\infty. \quad . \quad . \quad . \quad . \quad . \quad (67)$$

If this suggested asymptotic relation should be confirmed then (cf. eqns. (37) and (38))

$$\beta_{C}\rightarrow\text{constant}\,\frac{\kappa}{\nu}\left(\frac{\Omega}{R}\right)^{2}\quad(T\rightarrow\infty). \quad . \quad . \quad . \quad . \quad . \quad (68)$$

It is important to remember in this connection that in the presence of rotation convection currents cannot be entirely meridional. Thus,

Table 3. The Coefficients $A_{n,j}$ in the Expansion $U=\sum A_{n,j}T_{n,j}$ for the Solutions Obtained in the Different Approximations ($A_{0,1}=1$)

T	Approx.	$A_{0,2}$	$A_{0,3}$	$A_{2,1}$	$A_{2,2}$	$A_{2,3}$
1000	second			+0·0288		
	fourth	−0·00010	—	+0·0286	+0·0074	—
2000	second			+0·0574		
	fourth	−0·00039	—	+0·0561	+0·0143	—
4000	second			+0·1104		
	fourth	−0·00118	—	+0·1015	+0·0274	—
6000	second			+0·1535		
	fourth	−0·00175		+0·1322	+0·0392	
	sixth	−0·00291	+0·00032	+0·1320	+0·0391	−0·0019
8000	second			+0·1869		
	fourth	−0·00180	—	+0·1512	+0·0498	—
10000	second			+0·2127		
	fourth	−0·00133		+0·1627	+0·0593	
	sixth	−0·00424	+0·00042	+0·1626	+0·0593	−0·0032
20000	second			+0·2808		
	fourth	+0·00552		+0·1759	+0·0957	
	sixth	−0·00216	+0·00020	+0·1758	+0·0954	−0·0056
50000	fourth	+0·0279		+0·1605	+0·1483	
	sixth	+0·0088	−0·0041	+0·1608	+0·1474	−0·010
70000	fourth	+0·0373		+0·1534	+0·1648	
	sixth	+0·0126	−0·0065	+0·1539	+0·1636	−0·0116
100000	fourth	+0·0463		+0·1469	+0·1794	
	sixth	+0·0161	−0·0094	+0·1476	+0·1779	−0·0135
200000	fourth	+0·0597		+0·1381	+0·1995	
	sixth	+0·0181	−0·0151	+0·1392	+0·1972	−0·0172
1000000	fourth	+0·0732		+0·1301	+0·2183	
	sixth	+0·011	−0·0237	+0·1319	+0·2148	−0·024

according to eqn. (17) rotational motions must be present with an aplitude and a character which are determined directly by the meridional motions. Finally, it is worth noticing that in the expansion of U in the modes

$T_{n,s}$ (cf. eqn. (42)) the principal terms are the (0, 1), (2,1) and (2, 2) modes (see table 3).

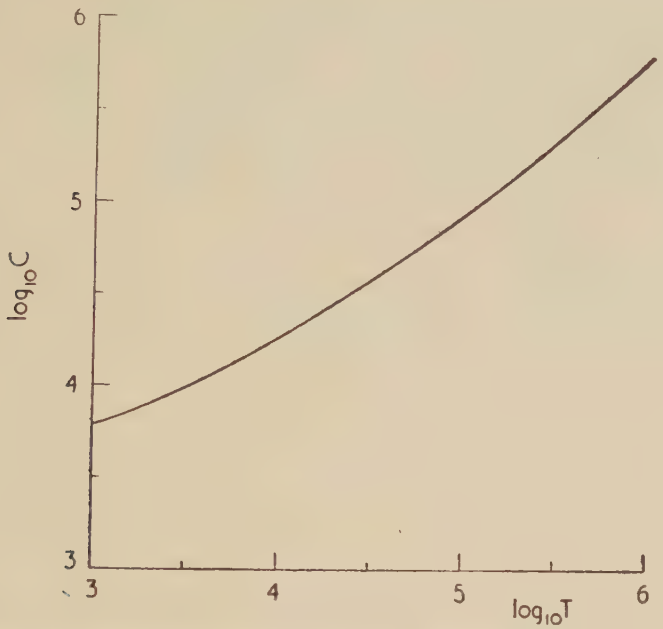

Illustrating the dependence of the Rayleigh number C for the onset of the lowest mode of instability on the Taylor number T.

§ 5. Concluding Remarks

This paper makes hardly more than a beginning in the study of the many problems of hydrodynamic and hydromagnetic stability in rotating fluid spheres. Thus, even in the special problem which has been considered, the assumption of a stationary marginal state should be given up: for, it is known (Chandrasekhar and Elbert 1955, Fultz and Nakagawa 1955) that in fluids with low Prandtl numbers (as most metallic liquids are) instability is more likely to set in as overstability than as convection. The discussion of the overstable case was difficult enough in the plane problem; but its importance would justify the efforts which would be needed to solve the same problem in a sphere.

Acknowledgments

In conclusion I should like to record my grateful appreciation of the assistance I have received from Miss Donna Elbert: she carried out the extremely laborious calculations which were needed for this investigation.

The research reported in this paper has in part been supported by the Geophysics Research Directorate of the Air Force Cambridge Research Center, Air Research and Development Command, under Contract AF19(604)–2046 with the University of Chicago.

References

Backus, G. E., 1955, *Phil. Mag.*, **46,** 1310.

Chandrasekhar, S., 1952 a, *Phil. Mag.*, **43,** 501 ; 1952 b, *Ibid.*, **43,** 1317 ; 1953 a, *Proc. roy. Soc.* A, **217,** 306 ; 1953 b, *Phil. Mag.*, **44,** 233, 1129 ; 1954 a, *Ibid.*, **45,** 1177 ; 1954 b, *Proc. roy Soc.* A, **225,** 173 ; 1956 a, *Ibid.*, **237,** 476 ; 1956 b, *Astrophys. J.*, **124,** 232 ; 1956 c, *Proc. nat. Acad.*, **42,** 1 ; 1956 d, *Astrophys. J.*, **124,** 244.

Chandrasekhar, S., and Elbert, D. D., 1955, *Proc. roy. Soc.* A, **231,** 198.

Elbert, D. D., 1957, *Astrophys. J. Suppl.*, Series 3 (in press).

Fultz, D., and Nakagawa, Y., 1955, *Proc. roy. Soc.* A, **231,** 211.

Jeffreys, H., and Bland, M. E. M., 1951, *Mon. Not. R. astr. Soc. geophys. Suppl.*, **6,** 148.

Lüst, R., and Schlüter, A., 1954, *Zs. f. Ap.*, **34,** 263.

Nakagawa, Y., 1957, *Proc. roy. Soc.* A, **240,** 108.

Wasiutynski, J., 1946, *Astrophys. Norveg*, **4.**

The Etching of Diamonds by Low Pressure Oxygen†

By M. Omar and M. Kenawi
Physics Department, A'in Shams University, Cairo

[Received May 9, 1956]

Abstract

Diamonds have been etched by heating on a molybdenum filament in a low pressure (about 2·5 μ Hg) of oxygen. The etch figures obtained by this method have the same orientation as those obtained by etching in oxidizing melts, but differ in outline by being sharply triangular. They are in fact similar in all respects, except for the inverted orientation, to the natural features called 'trigons'. It is therefore concluded, contrary to recently accepted opinion, that the latter are also probably etch figures, produced by an unknown natural etching process.

Note: Unless the edge of the crystal is in the field of view, all upright triangles are etch pits.

§ 1. Introduction

Etch figures on diamond octahedral faces are generally produced by heating the crystal in fused potassium nitrate or sodium carbonate at temperatures ranging from 525°c to 900°c (see for example Fersmann and Goldschmidt 1911, Williams 1932, Omar *et al.* 1954). The fuses give a limited supply of oxygen which attacks the carbon atoms which are diamond.

The figures obtained are triangular depressions mainly of a pyramidical nature with rounded corners, and are oppositely oriented to the natural figures called 'trigons'. Such trigons exist on nearly all octahedral faces of diamond, and are a characteristic feature of them. The trigons were previously thought to be etch figures but it is mainly due to the work of Tolansky (1947 onwards) that trigons are now generally accepted as a growth phenomena. The present work is however a retreat back to the old view that trigons are most probably etch figures.

Tolansky was not the only worker who attributed trigons to growth, but was preceded by illustrious figures such as Crookes (1909), Fersmann and Goldschmidt (1911), Van Der Veen (1911) and Sutton (1928). To confirm their view, Tolansky and Wilcock (1947) used multiple beam interferometry under what they called 'high dispersion' technique. They discovered certain marks which appear as extensions to the sides of trigons. These extensions, called by Tolansky 'basal-extensions'.

†Communicated by the Authors.

were found to be composed of groups of steps leading partly to the trigons. The steps were considered as growth layer edges, and as such were taken as a definite sign of growth. Tolansky went so far as to incorporate these extensions in a theory, which according to him explained the reason of formation of trigons. Williams (1932) wrote at length supporting the growth view from a different angle. He presented series of photomicrographs which showed that certain hillocks abide by most of the trigons. Generally 2 or 3 hillocks confined a trigon. The hillocks were composed of layers and were described by him as ' growth hillocks '. He deduced that trigons must be attributed to the same cause, i.e. growth.

§ 2. Observations

Experimental procedure

Both characteristic features of assumed growth, i.e. ' basal extensions ' and ' growth hillocks ' have been produced artificially in a series of experiments which we have carried out on the etching of diamond using a new technique. For this purpose the crystal was placed on a molybdenum filament under vacuum of the silvering plant and heated to a temperature of about 1000°c. The favourable pressure used was about 2·5 microns of mercury. After a long time of etching (about seven hours) etch figures made their appearance. The figures obtained got gradually bigger and bigger, and smaller figures appeared, until finally a pattern was obtained which could not be differentiated from the usual pattern of trigons. This observation is new and has not been described before.

The New Etch Figures

Figure 1† is such a pattern obtained after 21 hours of etching. Figure 2 shows the orientation of these pits with respect to the face edge of the crystal. As expected the corners of the pits point towards the corners of the triangular crystal face. Figure 3 shows a group of natural trigons, and fig. 4 their orientation with respect to the crystal edge. As can be seen from figs. 2 and 4 the orientation of both sets of triangles is different while the grouping of both (cf. figs. 1 and 3) is identical. Both types of triangles are straight edged with no rounding at the corners of the etch pits as is indeed clear in figs. 1 and 2.

The above magnifications are not enough to show the two characteristic features referred to above, i.e. basal extensions and ' growth ' hillocks. A, B, C and D, fig. 5 are the basal extensions discovered by Tolansky in the case of trigons, while E, F, fig. 6 is a similar extension which occurred to an ' etch pit ' while the crystal was under etching in an atmosphere of oxygen under reduced pressure. The basal extension of fig. 6 appears as a sharp-edged shelf exactly as has been described by Tolansky in the case of trigons. Sometimes it extended as a continuation to two sides of a single etch pit, as is clearly shown, also in fig. 6. This latter observation is a characteristic feature of most of the trigons.

† All figures are plates.

It has been mentioned that diamond octahedral faces are characterized not only by the existence of trigons, but also by the frequent occurrence of ' growth ' hillocks by the sides of the trigons. These are shown as A, B, and C, fig. 7 which is a feature of natural diamond. For the sake of comparison we present fig. 8 which has been chosen from our series of photomicrographs of etching. X, Y and Z, fig. 8, are hillocks surrounding the etch pits in a manner similar to those in fig. 7. While A, B and C appear naturally on octahedral faces of diamond, X, Y and Z are the hillocks created in the etching process ; in other words they are ' etch hillocks '. The unexpected exact similarity of both kinds of hillocks is surprising. Both are composed of layers which have curved edges at the top, and except for the fact that they are oppositely oriented with respect to each other, one can say that they are similar in all essential respects.

In view of the above observations, it can safely be stated that, apart from the orientation referred to, no morphological difference exists whatsoever between an assumed growth pattern on a diamond crystal and an etch pattern created in the manner described above. It is natural to attribute both phenomena to the same origin, i.e. to an etching mechanism. The side walls of the triangular depressions on (111) are in both cases of the form (h k k), (k h k), k k h), with $k<k$ in the natural trigons and $h>k$ in those produced by etching in low-pressure oxygen. Regarding the reason for this difference no more can be said than that it is well known that different etching agents can have different etching habits. We know nothing of the conditions under which the diamond has been formed, but on account of the well known affinity between oxygen and hot carbon atoms, it is relieving to deduce that the etchant in the case of diamond cannot have been oxygen.

Two new characterizing features have been quite recently laid stress upon by Tolansky (1955). The first is supposed to be a property of the *etch figure*. It states that etch pits are generally rounded ; the second belongs to ' growth ' *trigons* and describes their ability to lie in linear formations.

When we etched our crystals in an atmosphere of oxygen under reduced pressure, we obtained straight edged triangles, as is indeed clear in the photomicrographs presented here. It is true that when the crystals are heated in fusing melts (Williams 1932, Tolansky 1955) or exposed to a hot oxygen jet (Shultink *et al.* 1954) rounded etch figures are generally obtained. The rounding of these figures cannot, however, be taken as a crystallographic property of the etch pit. It is most probably due to solution currents in the oxygen-giving fuses, as well as to eddy currents in the jet.

The property of ' growth ' trigons to lie in straight line formation at 60° is not a new discovery. It has already been described in rare cases by Sutton (1928). This rare grouping has, however, occurred in a crystal that we have etched. The linear formations in fig. 9 are made of small etch pits, not ' growth ' trigons, and the pits are seen in lines making 60° with each other, exactly as in the case of assumed growth.

The six-sided pit in fig. 9 enlarged in fig. 10 has originally been a trigon, inverted of course to the now existing etch pits. The etching extended its area, causing a slight truncation at the corners. Further etching caused the truncated corners to extend, forming steps simulating growth, while the originally straight edges of the trigon are now the curved sides of the figure. Ultimately the ' growth ' trigon will be converted into a larger etch pit, oppositely oriented to the original figure. The importance of fig. 10 is that steps on the face of a crystal are not necessarily a sign of natural growth. They arise as well during a process of etching.

The Role of Basal Extensions

Figures 11 and 12 show a group of etch pits at two successive stages of the etching process. They are produced at a somewhat large magnification in order to illustrate a very interesting property of the basal extension. A, B, C and D, fig. 11, are two basal extensions to two neighbouring etch pits. Further etching increased their length somewhat as in fig. 12. Ultimately they will close, forming a larger etch pit. The final pit will contain two smaller pits inside it. The mystery of formation of pits inside the territory of larger ones is at last revealed. The basal extension turns out to be the dynamic agent responsible for the occurrence of this interesting observation, far from being a mechanism of growth as has been assumed in the case of natural trigons.

On account of the unexpected exact similarity of etch and ' growth ' patterns, it is sometimes difficult to discriminate one from the other, unless of course the edge of the octahedron is in the field of view. It is interesting to study series of photomicrographs of the same etch setting to see how the etching proceeds. Figures 13, 14, 15 and 16 illustrate different stages in the etching process at 1000°C in an atmosphere of oxygen at a pressure of 2·5 microns of mercury. The etching periods were 10, 15, 21 and 25 hours respectively.

§ 3. Conclusion

It is thus clear that every property characterizing the so-called trigons or trigon formations has its prototype in etch phenomena. These properties are (*a*) extreme linearity of the edges of the triangular figures, (*b*) the step formation of the walls of the pyramidical depressions, (*c*) the occurrence of basal extensions, (*d*) the existence of hillocks by the sides of the triangles, (*e*) the ability of the triangles to lie occasionally in linear formation at 60°, (*f*) the existence of smaller figures inside the larger ones. It is difficult to attribute exactly similar features and formations, especially if they are of an odd nature, to different causes, and we conclude by attributing all triangular depressions and ' apparent ' elevations in the form of hillocks by the sides of the ' trigons ' to an etching mechanism. The word apparent is used because the hillocks abiding by the trigons are not actual elevations, but it is what is left over after the etching proceeded downwards forming the trigons. Since artificial etch pits, using oxygen

as an etchant at a moderately high temperature, are inverted with respect to the trigons (which in view of the authors are natural etch pits) we conclude that the natural etchant could not have been oxygen. Oxygen figures—oppositely oriented to the natural figures—are nearly non-existent on the faces of natural diamonds. Williams (1932), after sorting out hundreds of thousands of diamond octahedral crystals, found some such figures on the faces of a single crystal. It is thus clear that diamond grew in an environment devoid of oxygen. If the trigons are etch figures, an opinion which we strongly support, some other natural reagent is responsible for their existence.

References

Crookes, Sir William, 1909, *Diamonds* (London).
Fersmann, A., and Goldschmidt, V., 1911, *Der diamant* (Heidelberg : Winter).
Omar, M., Pandya, N. S., and Tolansky, S., 1954, *Proc. roy. Soc.* A, **225**, 33.
Schultink, H. L., Spiers, and Van der Wagt, 1954, *Philips tech. Rundschau*, **16** (3), pp. 79–86.
Sutton, J. R., 1928, *Diamond* (New York : Van Nostrand).
Tolansky, S., 1955, *Microstructure of Diamond Surfaces* (London : N.A.G. Press).
Tolansky, S., and Wilcock, W. L., 1947, *Proc. roy. Soc.* A, **191**, 182.
Van der Veen, A., 1911, *Symmetrie Van Diamant* (Leiden).
Williams, A. F., 1932, *The Genesis of diamond* (London : Benn).

The Kinetics of Colour Centre Formation in Quartz†

By E. G. S. Paige
Royal Radar Establishment, Gt. Malvern, Worcs.

[Received April 17, 1957]

Summary

It is shown that when free carriers are generated in a solid containing two or more types of defect capable of trapping electrons or holes, the occupancy of one type of trap is not, in general, a simple irradiation time dependent function of the form $1-\exp(-t/\tau)$ but is dependent on the parameters of the other traps and at saturation can be significantly less than unity.

Using a model for crystalline quartz it is possible to explain radiation bleaching by both x-rays and neutrons, by considering the dependence of the occupancy of one trap on other traps. With the same model an explanation of the effect of heat treatment on the kinetics of colouration observed by Forman (1951) is given. From a quantitative comparison between the predicted and observed rate curves of an x-ray irradiated crystal, f-values and defect concentrations are calculated. Less detailed comments are made on the coloration of fused quartz.

§ 1. Introduction

Observations on changes in the concentration of colour centres have become part of the standard method of gaining information about defects in certain solids. In some instances the defect forms a colour centre and so gives rise to absorption only after it has trapped an electron or hole. The concentration of such colour centres, and hence the absorption, will depend on both the concentration of defects and the fraction of them which have trapped the requisite charge carriers. It is important to know, therefore, the factors which determine the fraction of traps which are filled ; they are considered in this paper. In particular it is demonstrated how the kinetics governing the trapping of a charge carrier at one type of defect may be influenced by trapping at another, or several other types of defect.

The analysis has been carried out for quartz though the results obtained may be more generally applicable. Quartz has been chosen to simplify the analysis since it is known that defects are not created or annealed, nor are colour centres thermally bleached during x-ray irradiation at room

† Communicated by the Author.

temperature (Mitchell and Paige 1956). Data relating the change of absorption to radiation dose (rate curves) have been published by Forman (1951), Ditchburn *et al.* (1954) and Mitchell and Paige (1956) for crystalline quartz and by Dainton and Rowbottom (1954), Levy and Varley (1955), and Ditchburn *et al.* (1954) for fused quartz. In some of the rate curves the absorption passes through a maximum before reaching a constant value. This unexplained feature has been called radiation bleaching. It is shown by the B_1 band of one sample in fig. 1, which presents some previously unpublished rate curves of two specimens of fused quartz x-ray irradiated under identical conditions. By considering the dependence of the occupancy of one trapping state on that of the other trapping

Fig. 1

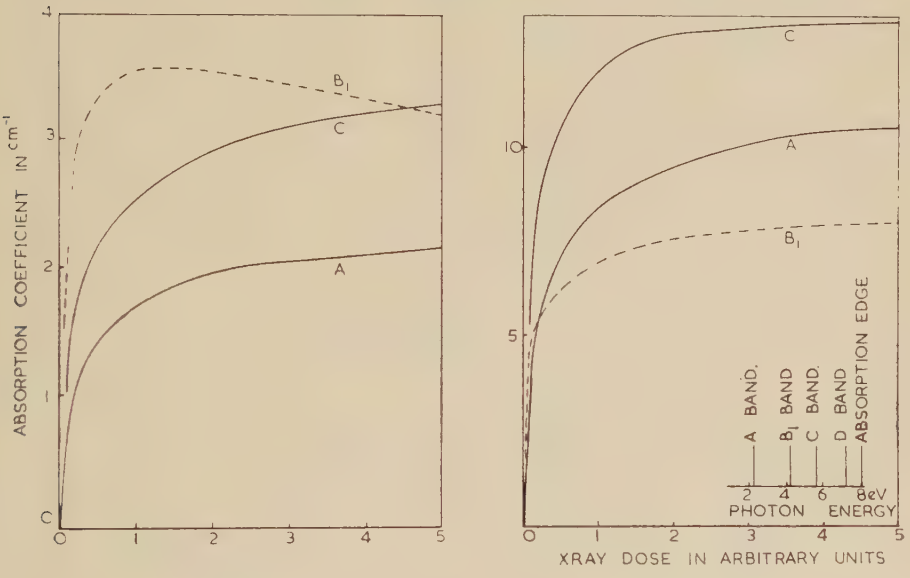

(*a*) (*b*)

Rate curves of two samples of fused quartz x-irradiated under the same conditions.

states it will be shown that radiation bleaching, together with the effects of previous heat treatment on rate curves observed by Forman (1951), may be explained. It will also be demonstrated that there is no justification for assuming the fraction of occupied trapping states to be unity when the absorption saturates. Often this assumption is made implicitly in calculating defect concentrations.

§ 2. A 'Single Centre' Model

To introduce the notation and the method of analysis together with some general assumptions, a simple model is considered. In this model only electrons can be trapped to form colour centres. Holes are immobile. For this and other models used it is assumed that traps are randomly

distributed and that phonon induced transitions between the trapping state and an energy band are negligible.

When quartz is irradiated with x-rays we are concerned only with electronic processes such as the generation of free carriers, the occupancy of existing trapping states and the recombination of electrons and holes. If I is the number of photons incident on unit area in unit time. μ_p the photoelectric absorption coefficient and γ the number of electron-hole pairs created by each photoelectron then the rate of generation of electron-hole pairs, X, is given by $I\mu_p\gamma$ for specimens of thickness x such that $\mu_p . x \ll 1$. For such samples X can be assumed uniform throughout the volume of the crystal. Wolff (1954) has shown that an upper limit to γ is $\frac{2}{3}E/Eg$ where E is the photoelectron energy, and Eg the gap width of the solid. For 30 kv x-rays and a typical dose rate X is about 2×10^{14} cm^{-3} sec^{-1}. The free electron concentration is reduced by recombination and trapping processes. The trapped electron can be released by either a sufficiently energetic electron or by direct interaction with the incident radiation. Release by both these mechanisms is assumed negligible. The differential equations governing the free electron, trapped electron and hole concentrations are

$$dn/dt = X - C_1 n(N_C - n_C) - knp, \quad . \quad . \quad . \quad . \quad . \quad (1\,a)$$

$$dn_C/dt = C_1 n(N_C - n_C), \quad . \quad . \quad . \quad . \quad . \quad . \quad . \quad . \quad (1\,b)$$

$$dp/dt = X - knp. \quad . \quad . \quad . \quad . \quad . \quad . \quad . \quad . \quad . \quad (1\,c)$$

The consideration of charge neutrality implies that

$$n + n_C = p. \quad . \quad . \quad . \quad . \quad . \quad . \quad . \quad . \quad . \quad (1\,d)$$

Here n, p, n_C and N_C are the concentrations of free electrons, holes, trapped electrons and electron traps respectively. C_1 and k are rate constants given by $\langle v\sigma_1 \rangle$ and $\langle v\sigma \rangle$ where v is the electron velocity, σ_1 is the cross section for the capture of an electron at a defect and σ the recombination cross section of an electron and hole. The v, σ product is averaged over the free electron distribution. The choice of symbols in this and the next two sections has been made in anticipation of their application to quartz.

In order to simplify the solution of these equations, certain assumptions will be introduced which may be qualitatively justified for quartz. It has been observed by Choong (1945) and others that only fluorescence occurs when quartz is irradiated with x-rays. Since it is certain that some of the fluorescence is due to trapping or recombination of free carriers it can be assumed that the free carrier concentration decays in a fraction of a minute. Using a typical dose rate coloration takes many hours. Thus the free carrier concentration is governed by a very short time constant compared with that controlling the formation of centres. Therefore we may regard the free carrier concentration to be at an equilibrium value determined by the occupancy of traps.

In the absence of traps eqns. (1 a) and (1 c) become identical and may be solved directly to give

$$n = p = \chi_0 \tanh(t/\tau),$$

where χ_0 is the saturation concentration of free electrons given by $[X\,k]^{1/2}$ and τ a time constant of $[k\,.\,X]^{-1/2}$. For a typical value of $X=2\times10^{14}$ cm^{-3} sec^{-1}, taking $v=10^7$ cm sec^{-1} and $\sigma=10^{-18}$ to 10^{-22} cm^2, values of $\chi_0=4\times10^{12}$ cm^{-3}, $\tau=2\times10^{-2}$ sec and $\chi_0=4\times10^{14}$ cm^{-3}, $\tau=2$ sec are obtained for the respective values of σ. We note that this time constant is short compared with hours and that values of χ_0 are small compared with detectable concentration of centres in thin samples (10^{16} cm^{-3} or greater in a 1 mm thick crystal). The presence of trapping states will lower the equilibrium free electron concentration. Any changes therefore, which occur in the population of traps after the x-irradiation has ceased are insignificant.

In the presence of N_C electron traps the equilibrium concentration of free electrons is

$$\chi=\tfrac{1}{2}b\left[\left(1+\frac{4\chi_0^2}{b^2}\right)^{1/2}-1\right],$$

where

$$b=\frac{C_1N_C+n_C(k-C_1)}{k}.$$

Inspection of b shows that when n_C reaches an observable concentration, $b\gg\chi_0$, so that $\chi\simeq\chi_0^2/b$. Substituting this value of χ in eqn. (1 b) and integrating, using the condition that $n_C=0$ at $t=0$, gives

$$\ln(1-y)+y(k-C_1)/k=-XC_1t/(N_C\,.\,k),$$

where y is the fraction of occupied traps. If $k=C_1$, then the solution reduces to

$$y=\left(1-\exp\left[-\frac{X}{N_C}\,.\,t\right]\right). \qquad (2)$$

This is the simplest rate law which can govern the formation of colour centres. However, it is seen here to occur as a special solution for a very simple model. The time constant of eqn. (2), N_C/X, is 1×10^4 sec for a trap concentration of 2×10^{18} cm^{-3} and the value of X previously chosen. This exceeds the time constant governing the free electron concentration by several orders of magnitude, an essential result for the self consistency of the method of analysis.

§ 3. Two Trapping States

Two trapping states are present in this model, one traps an electron, the other a hole. Both charge carriers are mobile. The main purpose of this model is to demonstrate how the parameters controlling the trapping at one type of defect may affect the kinetics governing the trapping at another. This interaction is transmitted by the free electron and hole concentrations, both of which may be controlled by the presence of trapping states.

Recombination of electrons and holes can take place in three ways: by direct recombination as in the previous model, by a free electron recombining with a trapped hole (rate constant A_2) and by a free hole recombining

with a trapped electron (rate constant C_2). The differential equations for the concentration of centres and free carriers are

$$dn/dt = X - C_1 n(N_C - n_C) - A_2 n p_A - knp, \quad . \quad . \quad . \quad (3\,a)$$

$$dp/dt = X - A_1 p(P_A - p_A) - C_2 p n_C - knp, \quad . \quad . \quad . \quad (3\,b)$$

$$dn_C/dt = C_1 n(N_C - n_C) - C_2 p n_C. \quad . \quad . \quad . \quad . \quad . \quad . \quad (3\,c)$$

$$dp_A/dt = A_1 p(P_A - p_A) - A_2 n p_A. \quad . \quad . \quad . \quad . \quad . \quad . \quad (3\,d)$$

To conserve change neutrality, assuming the defects are charged,

$$n + n_C = p + p_A, \quad . \quad . \quad . \quad . \quad . \quad . \quad . \quad . \quad (3\,e)$$

$$N_C = P_A.$$

P_A is the density of hole traps and p_A the concentration of holes trapped at them. A_1 is the rate constant for the trapping of a hole at a vacant hole trap.

Terms representing the excitation of electrons and holes from traps by direct absorption of an x-ray photon or by the impact of a high energy carrier have been omitted from eqn. (3). So have terms giving the rate of formation of centres by similar excitation processes occurring in the vicinity of a defect.

If $C_1 = C_2 = A_1 = A_2$, then for any value of k the equilibrium concentrations of free electrons, χ, and holes, ψ, are independent of the fraction of filled traps,

$$\chi = \psi = X/C_1 N_C.$$

The values of χ and ψ are obtained by the same method of approximation used in the previous section. It may be shown that this approximation is valid provided C_1^2, C_2^2, A_1^2, $A_2^2 \geqslant 10^{-23} k$, a condition which can be expected to be fulfilled in a real crystal.

The equations for n_C and p_A reduce to the simple expression,

$$n_C = p_A = \tfrac{1}{2} N_C \{1 - \exp(-2Xt/N_C)\}. \quad . \quad . \quad . \quad . \quad . \quad . \quad (4)$$

If however C_1, C_2, A_1 and A_2 are not all equal the values of χ and ψ are functions of the concentrations of centres formed. Suppose $C_1 = C_2 = A_1 = k$, but that $A_2 > k$, then the equilibrium free carrier concentrations are

$$\chi = X/[kN_C + (A_2 - k)p_A],$$

$$\psi = X/kN_C.$$

Substituting these values in eqn. (3 *d*) and integrating, using the condition that $p_A = 0$ at $t = 0$, gives

$$p_A = \{Y(1 + k/[A_2 - k]) - Y \exp(-2Xt/N_C)\}^{1/2} - Y/N_C, \quad . \quad . \quad (5)$$

where

$$Y \text{ is } kN_C^2/[A_2 - k].$$

The saturation density of centres is

$$N_C/[1 + \sqrt{(A_2/k)}].$$

Similarly, when $C_1 = A_1$, $C_2 = A_2$ and $C_1 \neq C_2$, a more complicated rate law than eqn. (4) is obtained and the saturation concentration of centres is

$$n_C = p_A = N_C/[1 + C_2/C_1].$$

From these examples we see that an essential condition for a simple rate law to be followed is that the free carrier concentration must be independent of the fraction of occupied states. This is achieved only when all the rate constants for transitions associated with the traps are equal, a condition which is unlikely to occur in a real crystal. When the free carrier concentration is sensitive to the density of colour centres the rate law is complicated and the saturation density of centres becomes a function of the rate constants. Only if the release of trapped electrons and holes is unimportant (values of A_2 and C'_2 very small compared with A_1 and C'_1) can the saturation concentration of centres equal the density of defects.

§ 4. A Model for Crystalline Quartz

Three absorption maxima have been observed in x-ray irradiated crystalline quartz by Mitchell and Paige (1956). A more realistic model for quartz, therefore, is obtained by introducing another trapping state, of density P_D, into the 'two centre' model previously considered. If these defects trap holes, the rate of colour centre formation is

$$dp_D/dt = D_1 p(P_D - p_D) - D_2 n p_D. \quad . \quad . \quad . \quad (6\,a)$$

where p_D is the density of D centres and D_1 and D_2 are rate constants corresponding to A_1 and A_2 for the A centre. Equations (3 *c*) and (3 *d*) are unaltered, while (3 *a*), (3 *b*) and (3 *e*) become

$$dn/dt = X - C_1 n(N_C - n_C) - n(A_2 p_A + D_2 p_D) - knp, \quad . \quad . \quad . \quad (6\,b)$$

$$dp/dt = X - A_1 p(P_A - p_A) - D_1 p(P_D - p_D) - C_2 p n_C - knp, \quad . \quad (6\,c)$$

$$N_C = P_A + P_D.$$

$$n + n_C = p + p_A + p_D. \quad . \quad . \quad . \quad . \quad . \quad . \quad . \quad . \quad (6\,d)$$

Inspection of these equations shows that the same general conclusion for the two-centre model is valid, namely that only when the free carrier concentration is independent of the density of centres are the rate laws for all the centres of the simple form given by eqn. (4). If the rate constants are not all equal the kinetics of colour centre formation become more complicated. To consider an interesting example, suppose all the rate constants have the same value except D_2 which is sufficiently small compared with the other rate constant for it to be taken as zero. Thus holes trapped at D defects cannot be released so the saturation concentration of D centres will inevitably equal the density of D defects. If the free carrier concentration was independent of the colour centre concentration, the saturation values of n_C and p_A would be $\frac{1}{2}N_C$ and $\frac{1}{2}P_A$ respectively. Clearly, when the value of p_D exceeds $\frac{1}{2}P_D$ the influence of the D centre will become marked, raising the concentration of C' centres above $\frac{1}{2}N_C$ and depressing the density of A centres below $\frac{1}{2}P_A$. It is proposed that this is the type of process which gives rise to radiation bleaching. Taking the

values of the rate constants chosen above, the equilibrium concentrations of electrons and holes are given by

$$\psi=\frac{X}{kN_C} \quad \text{and} \quad \chi=\frac{X}{k(N_C-p_D)}.$$

The concentration of D centres may readily be shown to be

$$p_D=P_D\left(1-\exp\left[-\frac{X}{N_C}.t\right]\right). \qquad (7)$$

Substituting in eqn. (3 *d*) for χ, ψ and p_D gives

$$\frac{dp_A}{dt}=\frac{X}{N_C}\left\{P_A-p_A\frac{(1+2\alpha+z)}{\alpha+z}\right\}, \qquad (8)$$

where $z=\exp(-Xt/N_C)$, and $\alpha=P_A/P_D$. Putting $\alpha=1$ and integrating, using the condition that $p_A=0$ at $t=0$, gives

$$p_A=P_A(1+3z+3z^2-7z^3)/3(1+z)^2. \qquad (9)$$

Fig. 2

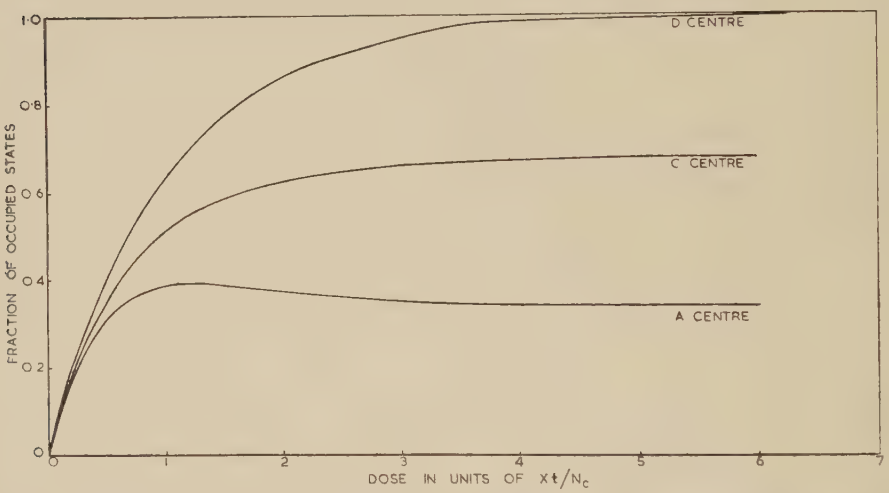

The variation of the occupancy of A, C and D defects with x-ray dose computed from eqns. (7) and (9).

The rate curve represented by this equation passes through a maximum before attaining an equilibrium value of $\frac{1}{3}P_A$. Such a dependence of absorption on radiation dose has been called radiation bleaching. The variation of the fraction of occupied traps with dose is shown in fig. 2 for n_C, p_A and p_D where n_C was obtained from $n_C=p_A+p_D$. A quantitative comparison between the observed rate curves and eqn. (9) is presented in § 5.

§ 5. Observed Rate Curves

5.1. *Radiation Bleaching by X-rays*

The three absorption maxima which have been observed in x-ray irradiated crystalline quartz have been called the A, C and D bands. The

rate curves for the A and C' bands (Ditchburn *et al.* 1954) show that the A band is radiation bleached. On the present theory, for radiation bleaching to occur there must be two defects which trap the same charge carrier. Further, it is changes in the occupancy of one of these two types of defect which are observed as radiation bleaching. Mitchell and Paige (1956) have presented evidence to show that a hole is trapped to form the A centre and an electron to form the C' centre. Therefore the D defect traps a hole to form a colour centre. Because of this conclusion, the A, C' and D centres considered in the model used in § 4 are identified as the centres giving rise to the A, C and D absorption bands.

To illustrate the measure of agreement, and the information that can be obtained, a comparison between the predicted and observed rate curves will be made. The rate curves for the A and C' bands of 100 kv x-ray irradiated quartz have been reported by Ditchburn *et al.*† (1954). The number of 100 kv photons incident on unit area per röntgen is 4×10^{9} cm^{-2} R^{-1} (Spoull 1946) and their photoelectric absorption coefficient in quartz

		Initial slope in cm^{-1} R^{-1}	Saturation absorption in cm^{-1}
A band	observed	5×10^{-6}	4·03
	predicted	$XP_Af_A10^{-16}/(N_C\,.\,\Delta E_A)$	$P_A{}^2f_A10^{-16}/(P_A+N_C.\Delta E_A)$
C band	observed	7×10^{-6}	11·1
	predicted	$Xf_C10^{-16}/\Delta E_C$	$N_C{}^2\,.\,f_C10^{-16}/(P_A+N_C\Delta E_C)$

is 0·5 cm^{-1}. Since the crystal used was 1 mm thick, it can be assumed that the rate of generation of free carriers was uniform throughout its volume and had a maximum value of $1{\cdot}7\times10^{13}$ cm^{-3} R^{-1}. If ΔE is the half-width of the band (1·8 ev for A, 1·4 ev for C) and μ is the absorption coefficient at its peak then $\mu.\Delta E=n.f\times10^{-16}$ where f is the oscillator strength for the transition. Using this relation various features of the rate curves can be compared with eqns. (3 *c*) and (3 *d*) as shown in the table. Equating the observed to predicted values tabulated it is found that $f_A=1{\cdot}0\times10^{-2}$, $f_C=5{\cdot}7\times10^{-3}$ and $P_A=2{\cdot}1\times10^{19}$ cm^{-3}, $N_C=4{\cdot}1\times10^{19}$ cm^{-3}, $P_D=2{\cdot}0\times10^{19}$ cm^{-3}. These are dependent on the value of X in such a way that if X is a maximum, minimum values of f and maximum values of defect concentrations are obtained. Since $P_A/P_D\simeq1$, eqns. (8) and (9) may be used in conjunction with the deduced f-values and defect concentrations to predict the maximum absorption of the A

† See fig. 12 of this paper. The initial increase of $d\mu/dt$ with dose is due to inaccuracies in estimating the *dose* between the first three measurements of absorption. Accordingly the origin has been taken at 2×10^{6} R in the calculations.

band and the dose at which it occurs, both can be found independently of X. The calculated values are 4·6 cm^{-1} and $2{\cdot}9\times10^6$ R respectively. These are in good agreement with the observed values of 4·35 cm^{-1} and between 2 and 3×10^6 R.

Mitchell and Paige (1956) have shown that the A defects are substitutional aluminium atoms and that for samples having a maximum A band absorption of 5 cm^{-1}, less than 50% of the total Al present in the crystal occurs substitutionally. Spectrographic analysis of the total Al content showed concentrations of 5×10^{19} cm^{-3} or more Al atoms for similar crystals (Ditchburn *et al.* 1954). An estimated concentration of 2×10^{19} cm ^{3} A defects from the rate curves is consistent with these data.

A more complicated model is required for fused quartz since five absorption bands have been observed (Paige 1955). However, radiation bleaching is believed to originate in the same way as in crystalline quartz. Figure 1 shows that radiation bleaching is dependent on the sample ; the bleaching of the B_1 band is observed for one specimen but not for another although they were irradiated under identical conditions. This can be explained by a difference in the relative concentrations of various defects. In fact, if in eqn. (8), α is made large or small compared with unity, eqn. (9) does not pass through a maximum.

If a simple rate law eqn. (4) is obeyed then a plot of ln $(\mu_s-\mu)$ against dose is linear where μ_s is the saturation value of the absorption coefficient. Figure 3 illustrates that a simple rate law is not followed by the A band of the silica sample shown in fig. (1 *b*). A plot of ln $(1-(\mu/\mu_s)^2)$ against dose is more nearly linear. This function was chosen because if $A_2\gg k$ in eqn. (5), then ln $[1-(\mu/\mu_s)^2]$ is proportional to dose.

Rate curves similar to fig. 1 have been observed by Dainton and Rowbottom (1954) except that their irradiation was not prolonged sufficiently for either saturation or radiation bleaching to be observed. It will be seen that the plot of ln $(\mu_s-\mu)$ against dose could be interpreted as the sum of two absorption coefficients each obeying a simple rate law. Dainton and Rowbottom suggested that both the A and B_1 bands did follow a simple rate law (eqn. (4)) but that they overlapped each other. This explanation requires that a high proportion of the absorption at the A band peak (2·3 ev) is due to the B_1 band. However, Yokota (1952) has prepared fused quartz which shows a B_1 band but no absorption for photon energies less than 3·0 ev. We may conclude, therefore, that the A band is following a more complicated rate law than that suggested by Dainton and Rowbottom and that it can be closely approximated by eqn. (5).

5.2. *Forman's Results*

Forman (1951) has published rate curves for the A band of crystalline quartz. After irradiating his samples till the transmission remained constant to within 1% (' saturation ') he thermally bleached them. On re-irradiation it was found that the rate of formation of A centres was faster and that the change depended on the time and temperature of the

heat treatment. No change of the saturation absorption and no radiation bleaching were observed. Similar heat treatment prior to the initial irradiation did not affect the rate of colour centre formation.

Radiation bleaching may not have occurred in Forman's samples because the relative defect concentrations were not suitable. Alternatively the condition for 'saturation' may have been such that the irradiation was terminated before radiation bleaching occurred.

Fig. 3

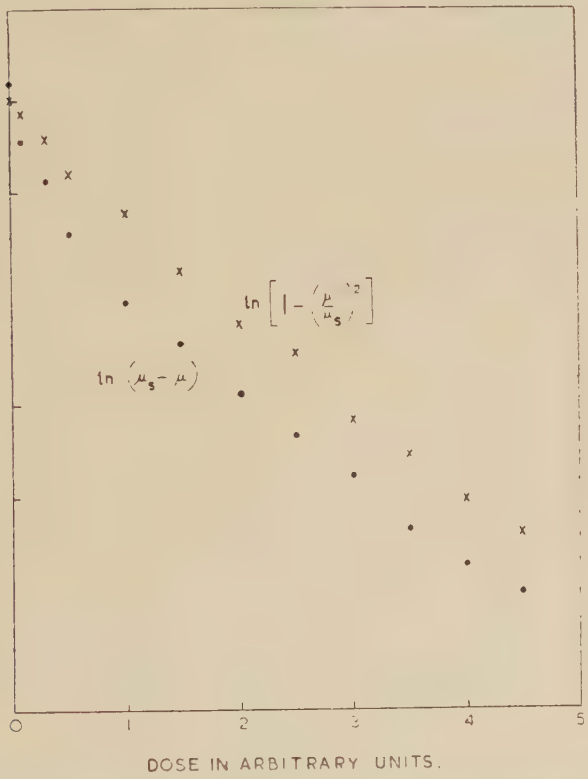

Plots of $\ln(\mu_s-\mu)$ and $\ln(1-[\mu/\mu_s]^2)$ against x-ray dose for the A band of fused quartz.

Since heat treatment prior to irradiation was ineffective, the effect observed is electronic in origin; it may be explained as follows. At 400°C, the temperature at which the heat treatments were carried out, the release of trapped carriers from A defects is much more rapid than from D defects (Paige 1955). Thus the A band may be completely bleached while C' and D centres still exist in the crystal. The distribution of electrons and holes in traps is then completely different from any distribution which occurs during the initial x-irradiation. This leads to changes in the kinetics of coloration of the A band on re-irradiation. To

illustrate this, suppose that after a heat treatment all A centres are bleached although all D centres are unaffected. With the same condition used in explaining radiation bleaching, $D_2=0$, the concentration of electrons will remain constant during re-irradiation at X . $(N_C-P_D)^{-1}$ cm^{-3}. This is a higher concentration than that encountered during the initial irradiation, except during the final stages, hence the A centre density will increase more rapidly during the early stages of re-irradiation. Longer periods of heating will reduce the D centre concentration significantly and the rate of increase in formation of A centres on re-irradiation will decrease accordingly. These are the effects observed by Forman.

Fig. 4

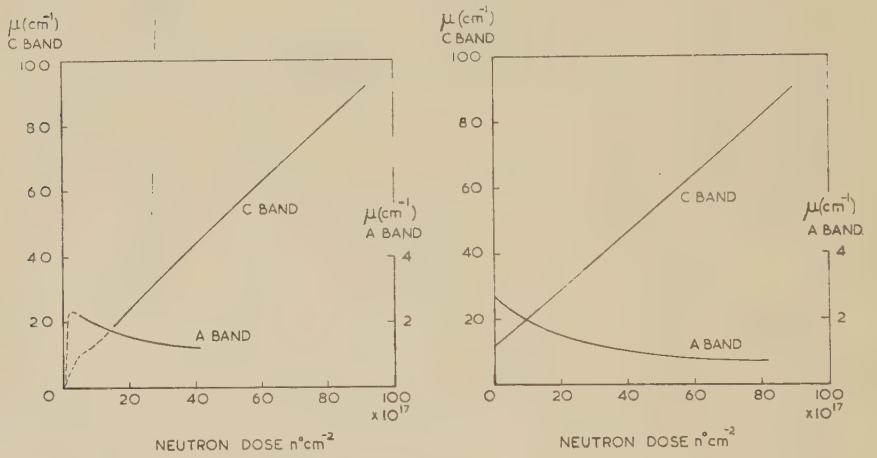

(*a*) (*b*)

(*a*) The observed rate curves of the A and C bands of neutron bombarded crystalline quartz. —— Concentration of centres in equilibrium with the total density of defects. – – – Before equilibrium is attained.
(*b*) Rate curves of the A and C bands of neutron bombarded crystalline quartz computed from eqns. (10) and (11).

Optical bleaching, which can be made more selective than thermal bleaching, should be more effective in demonstrating the changes in kinetics which can be achieved by disturbing the distribution of trapped electrons and holes.

5.3. *Radiation Bleaching by Neutrons*

An alternative means of changing the kinetics of coloration and also the equilibrium concentration of centres is to alter the relative densities of traps present, or to introduce new trapping states. Mitchell and Paige (1956) have demonstrated that fast neutron bombardment of quartz in a pile does both : the concentration of C centres is increased and a new absorption band, the E band, appears. The rate curve of the C band of neutron bombarded crystalline quartz is shown in fig. 4 (*a*) with that of the A band which is continuously radiation bleached.

In the pile the flux of ionizing radiation is such that the rate of creation of defects appears to be slow compared with the rate at which electrons and holes are trapped. The absorption of a specimen which had received a neutron dose of $3{\cdot}0\times10^{18}$ n/0 cm^{-2} was unchanged by subsequent x-irradiation. Accordingly the absorption after the initial rapid increase is assumed to be due to the equilibrium density of centres determined by the total concentration of defects. The continuous radiation bleaching of the A band can be shown to arise from a change in the occupancy of one type of trap due to the creation of other types of traps. The more obvious explanation for bleaching by neutron bombardment is that the defects in the solid are destroyed (Levy and Varley 1955). It has been shown by Mitchell and Paige (1956) that this is incorrect and that the bleaching is mainly electronic in origin.

Suppose that neutron bombardment increases the density of C defects and creates a new defect, E, both at a rate βt where β is a constant. The concentration of A and D defects remain constant. The E defects are included in the model for crystalline quartz by assuming that they trap holes (to maintain neutrality since the concentration of C defects is increasing) and have similar rate constants to the D defects. From eqn. (8) the equilibrium concentration of A centres is

$$p_A(\mathrm{eq})=P_A\cdot\frac{\alpha}{1+2\alpha}=\frac{{P_A}^2}{(P_A+N_C+\beta t)}. \quad . \quad . \quad . \quad (10)$$

The equilibrium concentration of C centres is

$$n_C(\mathrm{eq})=(N_C+\beta t)^2/(P_A+N_C+\beta t). \quad . \quad . \quad . \quad . \quad (11)$$

Figure 4 (*b*) show plots of $p_A(\mathrm{eq})$ and $n_C(\mathrm{eq})$ against dose. A comparison of fig. 4 (*a*) with 4 (*b*) shows that an explanation of the main features of fig. 4 (*a*) has been given. Further, when $N_C+\beta t\gg P_A$, $n_C(\mathrm{eq})\simeq N_C+\beta t$. Thus from the rate of change of μ_C with neutron dose for large doses, a value of f_C can be calculated if a reliable estimate of the neutron damage is available. Mitchell and Paige (1956) estimated that 25 ± 5 C defects will be produced in quartz per unit thermal neutron dose in a pile. Using this estimate and the observed rate of change of absorption an f-value of 6×10^{-3} is obtained for the C band. The variation of $n_C(\mathrm{eq})$ and $p_A(\mathrm{eq})$ have been shown as variations of absorption in fig. 4 (*b*). The absorption due to the centres was calculated using f_A and f_C obtained from the x-ray data.

§ 6. Conclusions

It has been shown that the occupancy of a trap is dependent on other types of traps which may be present. As a result a simple rate law for coloration cannot in general be expected. In addition, it is conceivable for the saturation concentration of colour centres to differ by orders of magnitude from the defect concentration.

A model for crystalline quartz was set up in which the number of types of defects was consistent with the radiation induced absorption

spectrum. It was possible to choose the rate constants for the defects so as to account for radiation bleaching under x-ray irradiation. Using the same model, including the selected rate constants, an explanation of Forman's observations on the effect of heat treatment on the rate curves of the *A* band was given. By extending the model to include defects produced by neutrons, the continuous radiation bleaching of the *A* band of neutron bombarded quartz could be explained. From a quantitative comparison between the predicted and observed x-ray rate curves, *f*-values and defect concentrations have been calculated. These were in agreement with those indicated by radiation damage calculations and the known concentration of aluminium in the crystal. Thus, although a major simplification was made by selection of the rate constants and the exclusion of certain processes the model is not inconsistent with known data. It is important to test its validity further since it provides the only means at present of estimating *f*-values and the fraction of occupied defects in quartz. The x-ray rate curves of the *D* band of a specimen which radiation bleached and the effect of thermal and optical bleaching on the subsequent rate curves of all three bands would be of great interest.

Acknowledgments

The author wishes to thank Dr. E. W. J. Mitchell and Dr. A. F. Gibson for their comments on this paper and to thank Dr. Mitchell for his advice and encouragement during its preparation.

References

Choong, S. P., 1945, *Proc. phys. Soc. Lond.*, **57,** 49.
Dainton, F. S., and Rowbottom, J., 1954, *Trans. Faraday Soc.*, **50,** 480.
Ditchburn, R. W., Mitchell, E. W. J., Paige, E. G. S., Custers, J. F. H., Dyer, H. B., and Clark, C. D., 1954, *Report of British Conference on Defects in Crystalline Solids* (London : Physical Society).
Forman, G., 1951, *J. opt. Soc. Amer.*, **41,** 377.
Levy, M., and Varley, J. H. O., 1955, *Proc. phys. Soc. Lond.* B, **68,** 223.
Mitchell, E. W. J., and Paige, E. G. S., 1956, *Phil. Mag.*, **1,** 1085.
Paige, E. G. S., 1955, *Thesis*, University of Reading.
Spoull, W. T., 1946, *X-rays in Practice* (New York : McGraw-Hill).
Wolff, P. A., 1954, *Phys. Rev.*, **66,** 1415.
Yokota, R., 1952, *J. phys. Soc., Japan*, **7,** 316.

Observations on the Magnetic Transition in Hematite at −15° C†

By G. Haigh
Department of Physics
Imperial College of Science and Technology, London

[Received April 13, 1957]

Abstract

An examination is made of the magnetic behaviour of hematite, αFe_2O_3, in the region of the antiferromagnetic transition temperature (−15°C). In this examination it is shown that the magnetic properties of hematite may be ascribed to two magnetically independent components of ferromagnetism, one dependent upon the antiferromagnetic transition whilst the other is independent of this transition. The magnetic properties of these two components have been determined firstly from a series of measurements with an astatic magnetometer, and then, by direct measurement at low temperature (−75°C), the magnetic properties of one component have been measured directly. These observations are critically discussed with reference to the magnetic structure for hematite proposed by Néel, and the inadequacy of this magnetic structure in accounting for some of the observations is pointed out.

§ 1

In 1950 Morin reported a transition in the magnetic susceptibility of hematite powders at about −15°C, and showed that this transition was suppressed by the introduction of 1% of titanium ions as an impurity. This transition has also been investigated by Néel and Pauthenet (1952) who observed the change in the remanent magnetization of a single crystal of Elba hematite. The effects on this transition of adding small quantities of impurity to hematite in the way described by Morin have been more fully investigated and reported in a previous paper (Haigh 1957), and these results were compared with the magnetic properties of some naturally occurring hematites. In this paper it was concluded that the magnetic properties of hematite were not only extremely structure sensitive but were also very dependent upon the past thermal and magnetic history of the specimens. Also briefly mentioned was a cyclic hysteresis effect involving temperature and remagnetization which has not previously been reported.

The present paper will describe in more detail this cyclic hysteresis effect with particular reference to the ' magnetic-structure ' for hematite proposed by Néel (1953), and further experiments which give more detailed information about this magnetic structure will also be described.

† Communicated by Professor P. M. S. Blackett, F.R.S.

§ 2

In all the experiments the remanent magnetization of the specimens was observed, i.e. measurements were always made in zero field. The specimens were in the form of circular discs of plaster of Paris, 2·3 cm in diameter and 0·5 cm thick, throughout which 0·5 g αFe_2O_3 was uniformly dispersed. The instruments used in measuring the remanent magnetism of the specimens were of two types.

The first used the astatic magnetometer for observing the changes in remanent magnetism of a hematite specimen in a thermal chamber situated in zero field immediately below the astatic system. The temperature of the specimen was lowered by a flow of cooled air passing over it, and by rotation of the specimen in the thermal chamber, changes in magnetization could be followed throughout the temperature range.

The second method of observation involved the use of a vibration instrument conceived by Blackett and originally built by Sutton. This instrument has been described in detail elsewhere (Blackett and Sutton 1956); the method of measurement is briefly as follows: the specimen is oscillated at 30 c/s along the axis of two pick-up coils connected in opposition. The induced e.m.f., which is proportional to the magnetic moment of the specimen, is amplified and recorded with a tuned vibration galvanometer. The pick-up coils were placed between the poles of an electromagnet and the vibrated specimen was enclosed in a thermal box which allowed the temperature to be varied between −70°c and 100°c. This method allows rapid and absolute measurements of the magnetic moment of a specimen in any desired field. It is less sensitive but much faster than the magnetometer method.

§ 3.1

Observations with the astatic magnetometer were made on the remanent magnetization of a hematite specimen during the cooling-heating cycle. The specimen was magnetized diametrally in a field of approximately 6000 Oe, cooled to −80°c and then allowed to regain room temperature†. The variation of the initial remanence, $J_{R,\,init}$ with temperature is shown in fig. 1.

As expected, the transition just below 0°c was found on cooling—the transition effect being completed at about −60°c. However, on re-heating back to room temperature, the remanence did not increase back to its original value, but only to about two-thirds of $J_{R,\,init}$. On remagnetizing the specimen at room temperature in the same field as previously, the remanence increased to its former value $J_{R,\,init}$. The cooling–heating cycle was repeated and the curves of fig. 1 were again traversed during the cycle. Here, then, we have a repeatable 'hysteresis-effect' involving change of temperature and remagnetization—the portion G to A being completed by remagnetization.

† Cooling rate ~1·0–1·5 deg./min.

§ 3.2

These experimental observations can be partially explained using the 'magnetic-model' of hematite proposed by Néel, originally for the case of a single crystal, but equally applicable to a powder specimen.

Néel described hematite as being primarily an antiferromagnetic body in which the direction of antiferromagnetism is parallel to the ternary axis below 260°K, and perpendicular to this axis above—this has been confirmed by Shull *et al.* (1951) using neutron diffraction. However, there is also present at all temperatures an *isotropic* parasitic ferromagnetism whose hysteresis properties are independent of direction in the crystal. Superimposed on this, and observable above 260°K, is another parasitic ferromagnetism which is essentially *anisotropic* and dependent not only upon direction in the crystal, but also upon the temperature, being closely linked with the direction of the fundamental antiferromagnetism. Both these components of ferromagnetism disappear at the Curie point, which is approximately 685°C.

Fig. 1

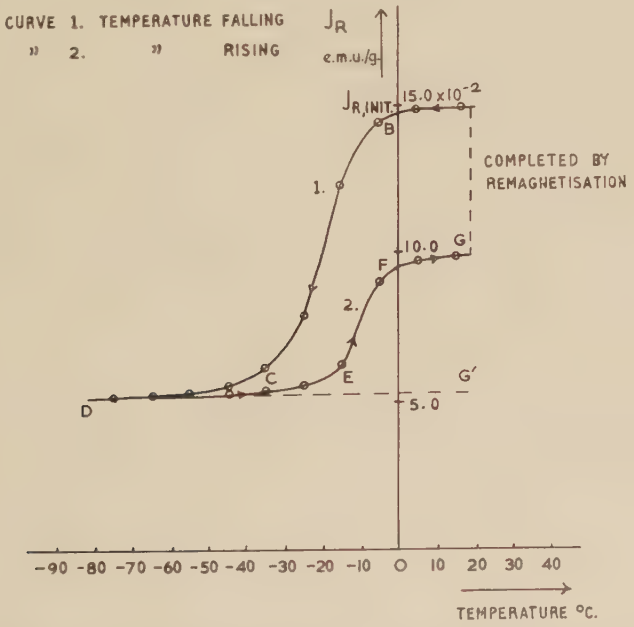

To interpret the observed changes below room temperature, Néel proposed that the spontaneous magnetization of the parasitic ferromagnetism was in a direction parallel to the fundamental antiferromagnetism. Above 260°K this parasitic ferromagnetism lies in the basal plane, but below 260°K, as the direction of antiferromagnetism coincides with the ternary axis, so the direction of this anisotropic parasitic ferromagnetism is also oriented along the ternary axis. However

as there is an equal probability of this orientation being in one direction as in the other along this axis, the anisotropic parasitic ferromagnetism should then disappear.

The cooling part ABCD of fig. 1 is therefore interpreted by Néel in the following way: in the region C–D, the observed ferromagnetic remanence is due solely to the *isotropic* parasitic ferromagnetism; in the region A–B, the magnetization is due not only to this *isotropic* ferromagnetism but also to the *anisotropic* ferromagnetism. In C–D the latter averages to zero, in A–B it takes its full spontaneous value. The region B–C of the cooling curve may be termed the 'transition-region', in which the parasitic ferromagnetism turns from a direction in the basal plane to be along the ternary axis perpendicular to this plane on cooling.

§ 3.3

In the reheating portion of this curve, the main transition of the anisotropic component takes place between E and F. As the specimen was situated in nearly zero field during this reheating, and assuming for the moment that there is no magnetic interaction or coupling between the two components of ferromagnetism, then there is no 'directive-force' influencing the anisotropic component to return in a preferred direction in the basal plane. Consequently this component should return into the plane in a completely random manner and there should be no increase in magnetization observed as the specimen heats up through the transition temperature. The curve should then follow the direction DEG′ shown dotted in fig. 1. The portion DEFG of the curve shows that this is not so, and there is a 'directional' return of the anisotropic component to the basal plane—this direction being that of the initial direction of magnetization of the specimen.

Considering now the possibility of external directive influences being present. By means of the vibration instrument described in § 2, it is possible to observe these remanent magnetization variations with temperature in the presence of an external field—this introducing a directive influence during the reheating. If the cooling and heating is carried out in a field $\sim$5000 Oe, then the curve corresponding to ABCD (fig. 1) is followed during the reheating as well as during the cooling, and Néel's explanation of the phenomena is valid in both parts of the temperature cycle. If, however, the observations are made in a weak field, say $\sim$20 Oe, then the behaviour similar to that shown in fig. 1 is observed. As the field at the specimen situated below the astatic magnetometer is at least two orders of magnitude less than this field of the vibration instrument, there will be no directive influence introduced by any incomplete cancellation of the earth's field in the former.

With regard to the possibility of there being an interaction between the two ferromagnetic components, this was also investigated with the vibration instrument in the following way. A virgin specimen was

cooled in approximately zero field to $-75°$C when it was magnetized in about 17 000 Oe. The field was then switched off and the specimen allowed to heat up in the small residual field of the magnet ($\sim$15 Oe). No increase in magnetization was observed as the specimen heated up through the transition temperature. There would not, therefore, appear to be any directive influence introduced by the isotropic component of ferromagnetism.

§ 3.4

From the nature of these experiments carried out to determine the origin of the directive influence present during the reheating in zero-field, it is immediately obvious that it must be a form of ' memory ' process—the effects only being observed when the specimen has been magnetized before cooling takes place.

Here, then, is a serious difficulty in the application of Néel's interpretation of the magnetic behaviour of hematite in the case when the observations of the remanent magnetization are made in zero field.

The amount of directional return , i.e. G'G in fig. 1 has been found to vary considerably with the particular sample of hematite, being least for highly pure, homogeneous and well crystalline samples of hematite, although so far it has not been possible to correlate this with any other property of the sample. Some of the variations found in the magnetic properties of different samples of hematite have been reported in an earlier paper (Haigh 1957).

Having observed the effect of cooling on a magnetized specimen of hematite, and the behaviour of the two parasitic ferromagnetisms in the cooling process, it is now possible to learn more about these two components by magnetically treating the specimen before subjecting it to the cooling cycle.

§ 4.1

Blackett (1956) has already discussed the effect of placing a ' backfield ' on a previously magnetically saturated specimen so as to leave the specimen weakly magnetized in a direction opposite to that of saturation, and has shown that the remanent intensity so produced reverses when the specimen is heated. By treating a specimen of hematite in a similar manner, and cooling it to $-75°$C, we can derive information about the two components of ferromagnetism, for at low temperatures we have only the isotropic component, whilst at room temperature, when the specimen was initially magnetized, we have both the isotropic (J_{I}) and anisotropic (J_{A}) components. It has been shown that J_{I} is relatively unaltered during the temperature cycle, and thus the effective J_{A}-value at room temperature can be determined. We are therefore able to obtain curves of J_{I} and J_{A} against H_{D}, the demagnetizing field field applied to the specimen after saturation. As we are measuring the remanent magnetization of the specimen, the coercivity determined from these curves is the remanence coercivity, and will be denoted by $(H_{\mathrm{c}})_{\mathrm{R}}$, to distinguish from the coercivity H_{c}, measured in the field.

§ 4.2

The procedure in each experiment was to saturate the hematite specimen at room temperature and then place it in given reverse fields. The percentage of saturation remanence (J_{init}) resulting from this treatment and its sign, either positive or negative according to whether the remanence was in the same or opposite direction to saturation, was measured. The specimen was then cooled to $-80°$C, and the variation of the intensity observed—a family of curves of this variation of J_{init}, after varying treatments, is shown in fig. 2. In the table there is given for each of the eight curves the demagnetizing field in column 2, and in column 3 and 4 the initial remanence, J_{init}, as a percentage of the saturation remanence $(J_s)_R$ and in e.m.u. g. respectively—these values being determined at 20°C. The J_I-values in e.m.u./g determined at $-75°$C when the transition is assumed to be complete, are given in column 5. The values of J_A, calculated from the vector relation $\mathbf{J}_{init}=\mathbf{J}_A+\mathbf{J}_I$, are given in e.m.u./g in column 6.

Fig. 2

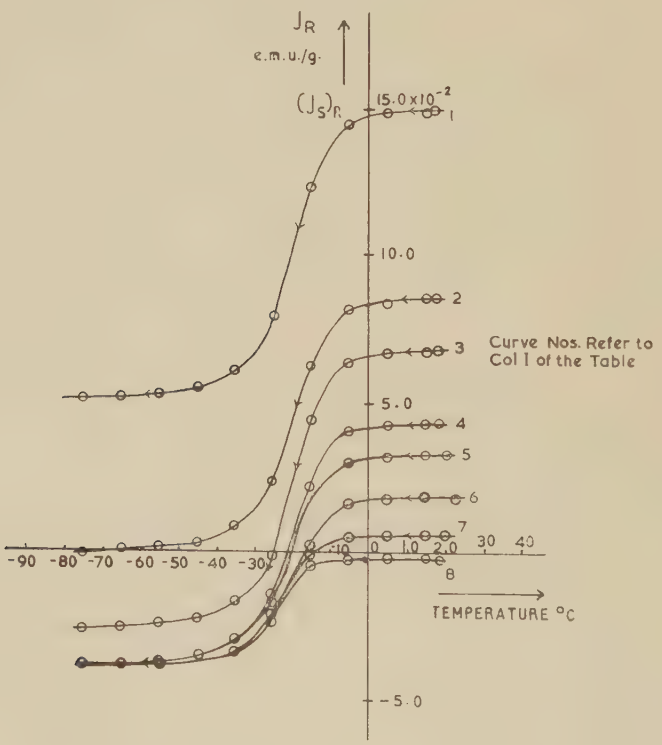

§ 4.3

The curve plotted from columns 2 and 4 of the table, shown in fig. 3, is the usual remanent demagnetization curve for the specimen when determined at room temperature. It gives a saturation remanence of

0·15 e.m.u./g and a remanence coercivity ~3200 Oe for the hematite specimen. (In this case the magnetizing field of 6000 Oe would not completely saturate the specimen. True saturation in hematite seems to be possible only with fields greater than 20 000 Oe).

Fig. 3

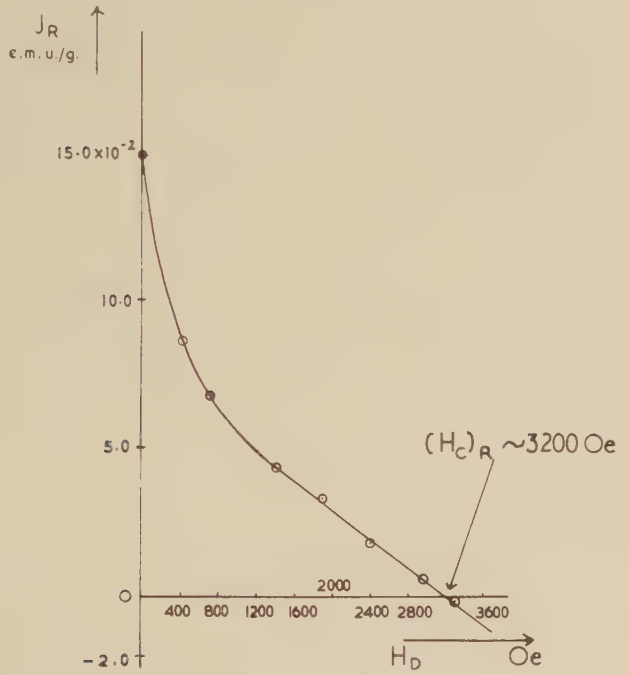

1 Curve	2 H_D Oe	3 $J_{inlt}=\frac{J_R}{(J_s)_R}$ %	4 J_{init} e.m.u./g.	5 J_I e.m.u./g	6 J_A e.m.u./g.
1	0	100	$+15{\cdot}0\times10^{-2}$	$+5{\cdot}1\times10^{-2}$	$9{\cdot}9\times10^{-2}$
2	438	~58	+8·7	−0·1	8·8
3	725	~45	+6·8	−2·6	9·4
4	1425	~29	+4·4	−3·8	8·2
5	1913	~22	+3·3	−3·9	7·2
6	2400	~12	+1·9	−3·8	5·7
7	2963	~4·0	+0·6	−3·9	4·5
8	3300	~−1·6	−0·2	−3·9	3·7

(The sign convention used above is as given in § 4.2) Initial saturating field 6000 Oe.

The curves plotted from columns 2, 5 and 6 of the table are the remanence demagentization curves for the two components of ferromagnetism in hematite.

The demagnetization curve for the isotropic component is a fairly smooth curve with a saturation value of $5{\cdot}1 \times 10^{-2}$ e.m.u./g and a remanence coercivity ~430 Oe. The shape of the curve is that usually observed with a material of low coercive force, i.e. magnetically 'soft'—this component saturating in fields of about 1200 Oe.

In contrast the demagnetization curve of the anisotropic component differs considerably from that for the isotropic component. With increasing demagnetizing field, the remanence does not fall-away rapidly and linearly from the saturation value of $9{\cdot}9 \times 10^{-2}$ e.m.u./g but appears to be little affected by fields less than 600 Oe. The magnetization effects in this low field region will be considered in more detail in § 4.4. For demagnetizing fields greater than about 800 Oe the magnetization falls

Fig. 4

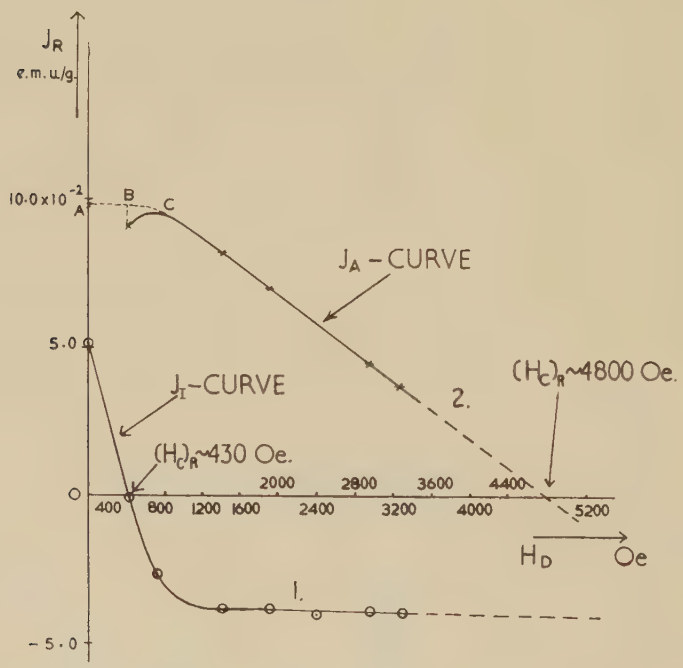

off linearly with the field, giving an extrapolated remanence coercivity ~4800 Oe. Thus this component has a remanence about double that of the isotropic component and a remanence coercivity more than ten times greater. With this high value of coercivity, the field necessary to saturate this component must be very high, probably of the order of several tens of thousands of oersteds.

Comparing the two components of ferromagnetism, the isotropic component is magnetically 'soft' whilst the anisotropic component is relatively 'hard'. It thus seems probable that it is this predominant anisotropic component of ferromagnetism of a magnetically hard nature

that prevents us saturating hematite specimens in moderate fields. The magnetic properties of hematite therefore will be determined principally by the magnetic properties of this anisotropic component. If the relative proportions of these two components in hematite samples can be varied, more may be learned about the magnetic structure of the mineral.

From neutron diffraction experiments carried out at room temperature and liquid nitrogen temperatures, there is evidence of a difference in the proportions of J_I and J_Λ components presents in samples of hematite which show very little decrease in the remanence on cooling and those samples showing a considerable decrease. This work however is still in progress and will be reported later.

§ 4.4

As a result of these measurements the orientation of the anisotropic component in the basal plane at normal temperatures was considered both in the magnetized and demagnetized states. On account of the trigonal symmetry of the rhombohedral crystal of hematite, it was suggested that for the anisotropic component a set of three easy directions of magnetization, 120° (2π 3) apart, may exist within the basal plane. The magnetic properties to be expected from such a system have been formulated mathematically by Dr. E. P. Wohlfarth (1955) of the Mathematics Department of Imperial College, to whom I extend grateful thanks for helpful discussions on this subject. Briefly the results to be expected are as follows: on magnetizing a completely virgin specimen to saturation, no remanence should be observed for fields less than a certain critical value. This is the field necessary to turn the intrinsic magnetization of a single domain through some minimum angle into an easy direction of magnetization nearer to the direction of the applied field—this minimum angle being a function of the spatial distribution of the easy direction of magnetization in the basal plane. Similarly, on demagnetizing a saturated specimen with this magnetic arrangement, a critical field must be applied before the state of saturation is altered—the critical fields in these two cases obviously being equal.

Results taken from the demagnetization curve of the anisotropic component seem to indicate that this critical field is of the order of 800 to 1000 Oe (AC in fig. 4). Using this value we find that the predicted remanence coercivity, from the model on which Dr. Wohlfarth's calculations are made, is at the most 1500 Oe. From curve 2 of fig. 4, the value deduced is more than three times this.

It is relevant to remark here that from the curves of fig. 4 the isotropic component is not strictly magnetically 'soft', but shows considerable hysteresis properties, having a remanence coercivity ~400 to 500 Oe. It is, however, soft when compared with the anisotropic component.

Whilst this model for the anisotropic component may be considered to give qualitative results about the shape of the demagnetization curve

and leads to a relatively high value for the coercivity, quantitative agreement has not been obtained. This model for the anisotropic component may require modification but until the variability in the properties of hematite samples is more fully understood, little quantitative agreement with theory can be expected.

§ 5.1

The next sections describe experiments in which the magnetic properties of the isotropic component are investigated directly at low temperatures, the observations being made with the vibration instrument described in § 2. With this instrument it is possible to measure directly the demagnetization curve for the isotropic component of ferromagnetism in hematite and compare it with that deduced in § 4.2 from the magnetometer observations.

If we cool a virgin specimen to $-75°$ C. magnetically saturate it and then demagnetize it at this same temperature, we will be observing only the isotropic component. In order to compare this curve with the J_I-curve of fig. 4, the magnetization was measured in zero field, after the demagnetizing field had been applied—this again gives the remanence coercivity $(H_c)_R$.

Fig. 5

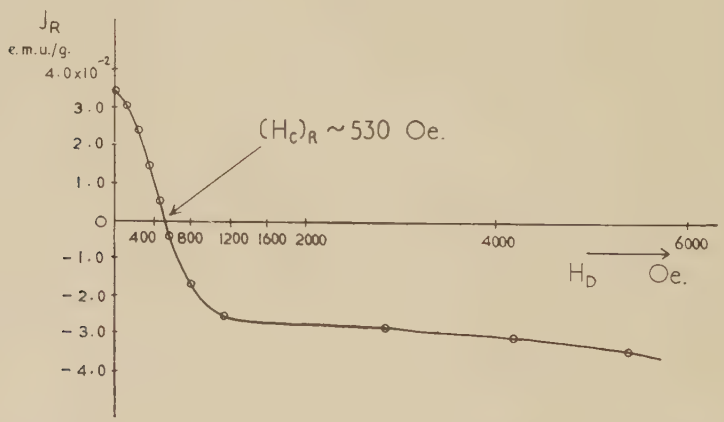

Figure 5 shows the directly measured demagnetization curve, which agrees well with the curve deduced from the magnetometer measurements, the coercivities in the two cases being ~ 530 Oe and ~ 430 Oe respectively. The differences in saturation moments can be attributed mainly to the variable properties of the hematite samples, the proportions of J_I and J_A components being different in the two samples—this possibility having been suggested already in § 4.3 as a result of neutron diffraction experiments. This similarity between the two J_I-curves can be seen even more clearly in fig. 6 where the normalized demagnetization curves have been drawn.

§ 5.2

Following the procedure described in § 5.1 for the demagnetization curve at −75°c, demagnetization curves were obtained for virgin specimens of hematite at temperatures of −40, −20, −10, −5, +20 and +40°c. The change in shape of these curves as the transition is

Fig. 6

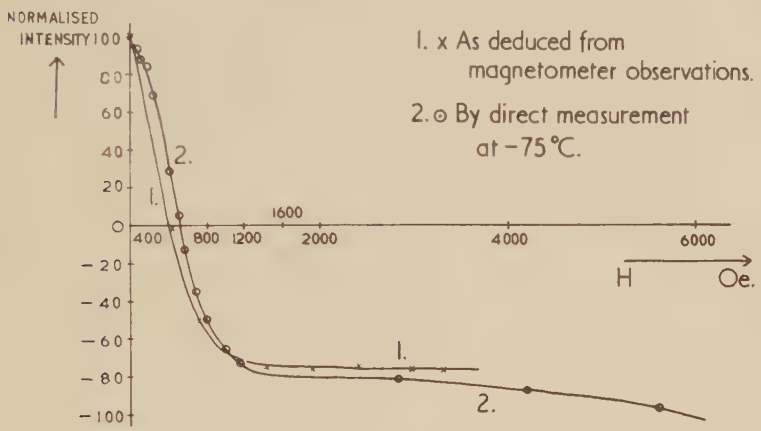

Fig. 7

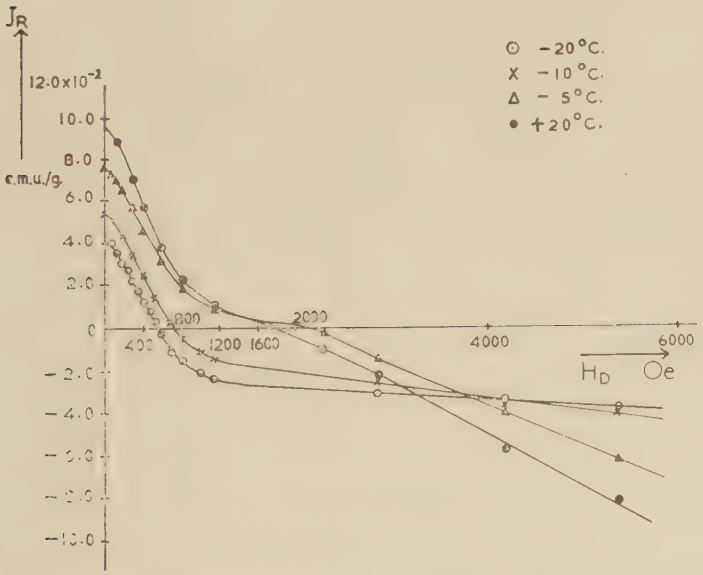

approached, and passed through, can be seen in fig. 7, where the main points of interest are firstly, in the movement of the ' knee ' of the curve, occurring at about 1000 Oe, across the H_D-axis for the higher temperature values, and secondly, in the increase in steepness of the curves past

the knee. The implications are that a hard second magnetic component is increasing in magnitude as the temperature increases from −20°c, thus requiring higher reversed fields to produce zero remanence of the specimen. The relative hardness of this new component, compared with that of the component existing below −20°c, can be inferred from the non-saturation appearance of the curves for fields less than 6000 Oe.

Using these demagnetization curves, figs. 8 (*a*) and 8 (*b*) were drawn. They show the variation of the remanence coercivity $(H_c)_R$, and saturation remanent magnetization as the temperature increases from −80°c through the transition region to +40°c. In fig. 8 (*a*) the broken curve

Fig. 8 (*a*)

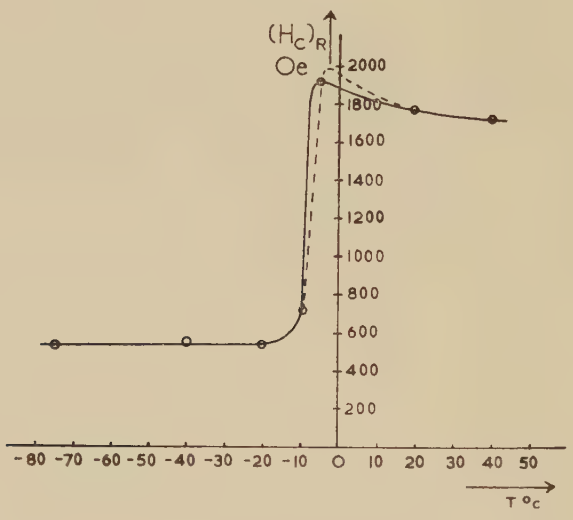

Fig. 8 (*b*)

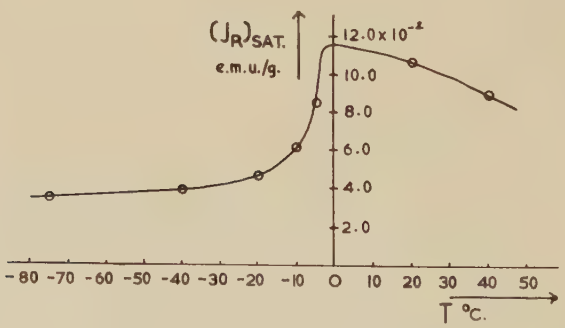

is drawn so that the maximum of this curve occurs at the same temper, ature as the maximum of curve 8 (*b*), although this latter curve is rather uncertain in the region of 0°c. Whilst with different hematite samples there may be a slight shift of these curves along the negative temperature axis, the general form of the curve is unlikely to vary much.

§ 5.3

The main results of this section of the paper are that the isothermal remanent magnetization curve at $-75°$C obtained by direct experiment is in excellent agreement with that deduced from the magnetometer observations of § 4.2, and that the method of analysis employed in § 4.2 of considering separately the two components of ferromagnetism seem to be justified in view of this agreement. As was expected from the magetometer results, there is a considerable change in coercivity through the transition temperature. The conclusion from considerations of the relative proportions of isotropic and anisotropic components present (from fig. 8 (*b*)) and of the change in coercivity through the transition (fig. 8 (*b*)) is that the coercivity of the hard (anisotropic) component must be of the order of several thousands of oersted, agreeing with the value deduced from fig. 4.

§ 6

From the observations described in this paper it is clear that there are several problems still to be solved before the magnetic properties of hematite are completely understood.

The theory put forward by Néel to account for the magnetic effects observed on cooling a hematite crystal has been shown to be applicable in the present investigation when hematite powder specimens were cooled to low temperatures. However, the theory does not explain the increase in magnetization as the specimen regains room temperature. The possibility of there being coupling between the two components of ferromagnetism has been investigated, but there does not appear to be any coupling of a magnetic nature.

These experiments, whilst contributing to the knowledge of the two parasitic components of ferromagnetism in hematite, do not assist greatly in establishing the more important question of the origin of the parasitic ferromagnetisms. This latter problem must be closely linked with that of accounting for the variability of the magnetic properties of different hematite samples.

As in the previous paper, it must be concluded that the results embodied in the present paper are more of qualitative than quantitative value on account of this variability of the magnetic properties of hematite from sample to sample.

Summary

In this paper the effects of cooling and reheating on a magnetized specimen of powdered hematite have been described and the observations have been discussed with particular reference to the two-component magnetic structure of hematite proposed by Néel.

It has also been shown that an analysis of the two components of ferromagnetism in hematite can be made in an original way by observations at temperatures above and below the antiferromagnetic transition

temperature of −15°C. Whilst one component (J_A) disappears on cooling through this temperature, the other component (J_I) is negligibly affected by this cooling so that the effects of any magnetic treatment on this latter component at room temperature, can be investigated by cooling below this temperature. Having determined the state of the J_I component by cooling, then by reference to the initial room temperature magnetic condition, the magnetic state of the J_A component was deduced. In this way the remanence demagnetization curves of a powder specimen of α ferric oxide have been determined for each of the components of ferromagnetism.

By direct experiment at low temperatures (−75°C) the demagnetization curve for the J_I component was determined, and good agreement found when compared with the curve obtained from the magnetometer measurements.

The magnetic properties of hematite were also examined near the transition temperature, where the effects of the anisotropic component are most marked.

Acknowledgments

The author wishes to express his indebtedness to Professor P. M. S. Blackett for his constant interest and advice throughout the course of this work.

He also wishes to thank Dr. M. Blackman of the Physics Department of this College for his helpful suggestions during the preparation of this paper.

Finally the author wishes to thank the Lancashire County Education Authority and the Department of Scientific and Industrial Research for grants enabling this research to be undertaken.

References

Blackett, P. M. S., 1956, *Lectures on Rock Magnetism* (Weizmann Science Press of Israel).

Blackett, P. M. S., and Sutton, D. J., 1956, *Lectures on Rock Magnetism* (Weizmann Science Press of Israel).

Haigh, G., 1957, *Phil. Mag.*, **48**, 505.

Morin, J., 1950, *Phys. Rev.*, **78**, 819.

Néel, L., and Pauthenet, R., 1952, *C. R. Acad. Sci. Paris*, **234**, 2172.

Néel, L., 1953, *Rev. mod. Phys.*, **25**, 58.

Shull, C. G., *et al.*, 1951, *Phys. Rev.*, **83**, 333.

Wohlfarth, E. P., 1955, *Phil. Mag.*, **46**, 1155.

Observations on Extensive Air Showers
III. The Distribution of Charged Particles†

By T. E. Cranshaw, W. Galbraith and N. A. Porter
Atomic Energy Research Establishment, Harwell

[Received March 21, 1957]

Summary

The distribution of charged particles in air showers containing 3×10^6, 3×10^7 and 10^8 particles at sea level has been measured and compared with theoretical calculations by Nishimura and Kamata. The best value of the age parameter S appears to be 1·4. The significance of this result is briefly discussed.

§ 1. Introduction

The lateral distribution of charged particles in extensive air showers has been the subject of many theoretical and experimental investigations. The theoretical calculations are concerned with the Coulomb scattering of the electrons in a photon–electron cascade, and the latest calculations of Nishimura and Kamata (quoted in Greisen 1956) seem to give good agreement with experiment. The distribution is obtained in terms of an age parameter S, $S=1$ representing cascades at the maximum of their development, and $S=2$ old cascades. The electrons observed in air showers must arise from cascades initiated by π^0 mesons at varying depths, and the mean value of S is usually found to lie between 1·2 and 1·4.

It is important to determine the structure over a wide range of shower sizes, since we might expect that changes in the shower development with energy will be reflected in the value of S which gives the best agreement. As the energy increases, it is expected that the shower will reach its maximum lower in the atmosphere, and that the dominant photon–electron cascades may have lower values of S.

Over the range of distances from the core which are of interest, the density varies by four or five powers of ten. Most experiments cannot cover this large range of density, and it is convenient to divide the experiments into three groups, according to whether the distances investigated are between 0·2 metres, 2–100 metres, or beyond 100 metres, calling the first group experiments on the core of the shower, the second short distance experiments, and the third large distance experiments. We are here concerned only with large distance experiments.

Barrett *et al.* (1952) have investigated the structure at large distances for showers containing between 10^4 and 10^6 particles at sea level, corresponding

† Communicated by the Authors.

to primary energies of about 10^{14}–10^{16} ev. Dobrotin *et al.* (1953) have reported measurements at 3860 m on showers containing up to 10^7 particles, the primary energy being about the same as in the Barrett experiment. Barrett *et al.* found good agreement with $S=1{\cdot}4\pm0{\cdot}15$, and Dobrotin found $S=1{\cdot}25\pm0{\cdot}12$. In the present experiments we have investigated the structure for showers containing 3×10^6–8×10^7 particles at sea level, corresponding to primary energies of at least 2×10^{17} ev. We discuss the significance of the distributions obtained.

Fig. 1

§ 2. Description of Apparatus

The apparatus has been described in paper I. In all cases showers are detected by ' a ' coincidences, that is by coincidences between the large 200 cm² counters in the units. The densities are determined from three other pieces of information: (i) the triggering of a tray of six 200 cm² counters placed at A, fig. 1; (ii) the triggering of the small ' b ' counters; (iii) the triggering of other ' a ' coincidences. (i) is mainly useful at large distances from the shower axis, where the density is of the order of 1 particle/m²; (ii) at short distances (densities up to 1000 particles/m²) and (iii) can be used at intermediate distances.

§ 3. Analysis of Results

3.1. *Selection of Showers*

Three shower sizes have been selected for analysis; I, those showers discharging just three units; II, those showers discharging eight or more

units ; III, those showers which it is supposed would have triggered 20 or more units on an infinite array. In category I, for the points plotted at 43, 93 and 134 metres, only those showers which discharged three units in a small triangle, none of which was on the outside edge of the array, were accepted. The densities at these points are obtained from information from the ' b ' counters which are either in the triangle discharged, or immediately surrounding it. For the points marked X in fig. 2, all showers discharging three contiguous units were accepted, provided that no unit discharged was on the outside edge of the array. For the remaining points obtained by the large tray all three-fold showers were accepted, and the

Fig. 2

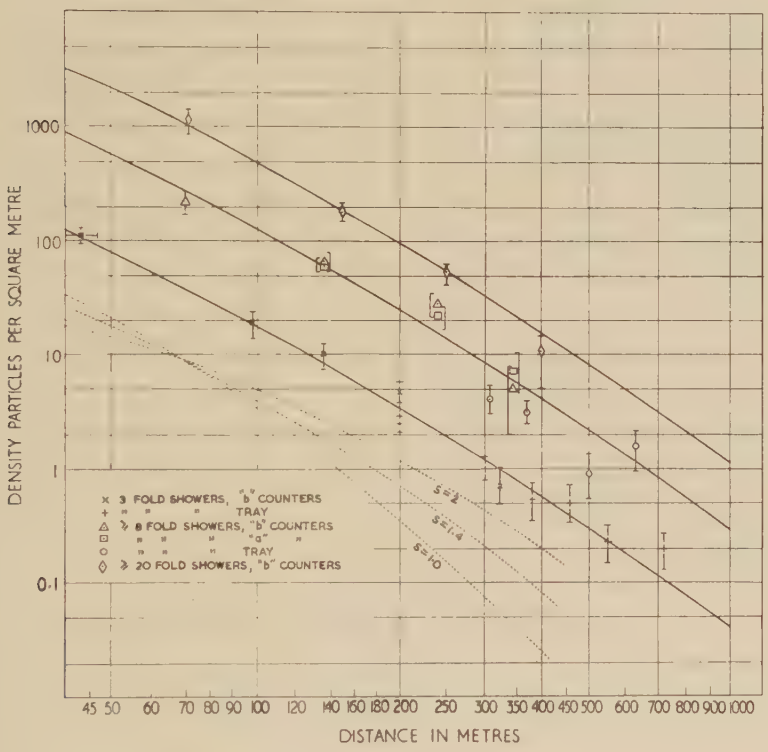

axis was assumed to lie at the centroid of the three units. The strict criteria for the shorter distances are necessary to ensure that the shower axis is reasonably well defined, but they can be relaxed for the greater distances. This point will be clearer when the estimates of distance are considered later.

In category II, for the points obtained from ' a ' and ' b ' counters, showers were accepted if the axis was judged to lie within the dotted area on fig. 1. For the points obtained by the tray, all showers were accepted, and again, the axis was assumed to lie at the centroid of the discharged ' a ' counters.

In category III, all showers were accepted provided that enough units on the array were discharged to make possible a reasonably precise determination of the position of the axis, and an estimate of the number of units which would have been triggered on an infinite array.

3.2. *Density Determination*

We assume that the showers have circular symmetry, that is to say the density ρ is a function only of r, the distance from the shower core. The expected fraction, p, of units in a narrow annulus of radius r to be discharged is then given by

$p_1=1-\exp(-\rho A_1)$ for single counters of area A_1 (' b ' counters or 6×200 cm^2 tray)

$p_2=\{1-\exp(-\rho A_2)\}^2$ for coincidence counters, area A_2 (' a ' counters).

From these expressions and the determination of p by counting, the density can be determined. In practice, the number of units in a narrow annulus is small. Hence we must average over many showers, which will not necessarily have the same density at r, and over relatively wide annuli. We first consider the effect of averaging over many showers, and in § 3.4 we consider the effect of taking wide annuli.

Table 1

$\bar{\rho}A$ for assumed distribution		0·02	0·1	0·2	0·6	1·0	2·0	4·0
$\bar{\rho}A$ from formulae	single counters	0·02	0·094	0·19	0·51	0·81	1·6	3·0
	coincidence counters	0·028	0·12	0·21	0·56	0·86	0·16	2·9

If ρA is known to be small over all the showers concerned, we may write $\rho=p_1/A_1$ or $\sqrt{(p_2)}/A_2$. The first of these is linear, and it is clear that the mean value of p which is obtained from the experiment gives $\bar{\rho}$, the mean value of ρ.

In order to get some idea of the errors involved when ρA is not small, or for the coincidence counters, we assume some form for the *a priori* distribution of ρ which approximates the distribution existing in the experiment. Then we may calculate $\bar{\rho}$ and $\bar{p}$ for this distribution, and compare the values with the values given by the simple formulae.

We have chosen a distribution of ρ of the form $N(\rho)d\rho=k\rho^{-3}d\rho$, from some value ρ_0 set by the shower selection criteria to infinity. Table 1 gives the values of $\bar{\rho}A$ for the assumed distribution, and calculated from the simple formulae. It will be seen that for the single counter measurements, no errors greater than 10% are involved if $\rho A<0{\cdot}25$, and for coincidence

counters if $0{\cdot}15 < \rho A < 0{\cdot}6$. These limits were observed throughout the work except for a few measurements at high density, where corrections of the order of 15% were applied.

In category I, the distribution of densities is certainly much narrower than given by the distribution assumed above, because large showers are excluded. Thus no corrections were necessary in this category.

3.3. *Procedure in Reduction of Results*

For the determinations with the tray, concentric circles were drawn round the tray as shown in fig. 1. Then during the observation period the number of showers in each category falling in the annuli was counted, and the number of times the tray was discharged recorded. Using the relations above, the density is determined. These results are plotted in fig. 2 at the mean distance for each annulus.

For the determinations at intermediate distances in category I, the following procedure was adopted. A number of showers satisfying the selection criteria was taken, and concentric circles drawn round the centroid of the struck counters at radii of 150, 250 and 400 m. The number of units lying in these annuli was counted, and the average taken over the sample. We have thus obtained the mean number of units, W, lying between 150 and 250 metres and 250 and 400 metres, from the axes of showers satisfying the selection criteria. The same shower data were used to find the rate S at which these showers are recorded by the apparatus. A much longer observation period was then used to find the rates C'_a, C'_b at which the ' a ' and ' b ' counters were discharged in the same annuli, in coincidence with showers of this type.

Then the fractions p_1, p_2 are given by

$$p_1 = \frac{C_b}{SW}, \quad p_2 = \frac{C_a}{SW}$$

and the density is determined as above.

3.4. *Estimation of Distance*

The points plotted at 43 m, 98 m and 138 m present the greatest difficulty. The point at 43 m is obtained from the number of times ' b ' counters are triggered in the units which define the 3-fold shower. In showers in which three units in a small 90 m side triangle have been triggered, the probability of the ' b ' counter being simultaneously triggered is found to be 0·16, corresponding to a density of 110 particles m^{-2}. We have now to determine what distance from the axis this density corresponds to.

We note that the centre of the triangle is 54 metres from the vertices. However, this is the distance corresponding to the measured density only if the density falls off as r^{-1}. In fact, rough measurements (by, for instance,

plotting these points at the mean distances) show that the slope is about $-1{\cdot}8$. To make a better estimate of distance we proceed as follows. We may assume for this calculation that the axes of showers causing the three-fold showers of this type fall nearly uniformly over the small triangle. (Calculations using an approximate distribution function show that this is not quite true, and experimental results on the variation will be given in paper V.) Then the probability that a ' b ' counter is triggered by showers at a distance r from the counter is

$$p=[1-\exp\{-\rho(r)A_1\}].$$

The number of shower axes at r, dr is proportional to $r\,dr$.

Therefore we may write the mean probability

$$\bar{p}=\frac{\int_0^R [1-\exp\{-\rho(r)\,A_1\}]\,r\,dr}{\int_0^R r\,dr}$$

where R is some distance representing the side of the triangle opposite the ' b ' counter. R was put equal to 84 m, but the result is not sensitive to the value chosen.

By using this expression, and assuming $\rho \propto r^{-1{\cdot}8}$, we find that the point 110 part/m^2 should be plotted at about 43 m, instead of 54, and an error of about 3 m has been allowed for the uncertainties of the calculation. Similarly the next point is plotted at 98 m, whereas the distance of the counters from the centre of triangle is 108 metres. The correction for the 138 metre point and more distant points is negligible.

For categories II and III, the procedure adopted was as follows. For each event, the position of the axis was judged visually. Then concentric circles were drawn round this point at 50, 100, 200, 300 and 400 metres. The number of units lying in each annulus and the number discharged was noted. The densities plotted are the result of averaging over 26 showers in category II and 20 in category III. For the densities at greater distances, the unshielded tray was used as before.

3.5. *The Density Distribution*

The results obtained are shown in fig. 2. The solid lines represent the best parabola through all the points, i.e. the curve is of the form $\rho=k\,r^{-(a+b\log r)}$. The best values for a and b are $a=0{\cdot}73$, $b=0{\cdot}38$. This means that at 100 m the distribution behaves like $r^{-2{\cdot}25}$, and at 400 m like $r^{-2{\cdot}71}$.

3.6. *Zenith Angle Effects*

Up to this point, we have ignored the fact that the showers are distributed in zenith angle. We show that a small correction can be made for this effect.

When a shower axis makes an angle θ with the vertical, particles which are at a distance r_m from the axis measured along the ground are not in general r_m from the axis measured normal to the axis, but are at some distance between r_m and $r_m \cos\theta$. To a sufficiently close approximation, we can say that the mean r is $\frac{1}{2}r_m(1+\cos\theta)$.

If we assume an exponential absorption in the atmosphere, we can write the zenith angle distribution as

$$J(\theta)\,d\theta = J_0 \exp\{B(1-\sec\theta)\}\sin\theta\cos\theta,\,d\theta$$

and the average value of r is given by

$$\bar{r} = \tfrac{1}{2}r_m \frac{\int_0^{\pi/2}(1+\cos\theta)\,J(\theta)\,d\theta}{\int_0^{\pi/2} J(\theta)\,d\theta}$$

$$= \tfrac{1}{2}r_m\left\{1+\frac{E_4(B)}{E_3(B)}\right\}\dagger .$$

From measurements of the barometer coefficient, we find $B\sim 8$. Then $\bar{r}=0{\cdot}95\,r_m$. Similarly, the effective area of the cylindrical counters is 0·95 of the measured area. The main effect of these corrections is to subtract 5% from the apparent total number of particles.

3.7. *The Total Number of Particles*

The dotted curves in fig. 2 are the curves of Nishimura and Kamata for $S=1{\cdot}0$, $1{\cdot}4$ and $2{\cdot}0$, and 10^6 particles. The experimental curve appears to be in good agreement with $S=1{\cdot}4$. If we assume that this distribution holds everywhere, the mean numbers of charged particles in the three categories are given in table 2.

Table 2

Category	I	II	III
$\bar{N}$	$3{\cdot}2\times10^6$	$2{\cdot}3\times10^7$	$9{\cdot}0\times10^7$

§ 4. Discussion

The experimental distribution is the distribution of charged particles, whereas the calculations refer to electron–photon cascades only. Measurements which will be reported later have shown that about 10% of the charged particles are μ-mesons (paper IV). However, the distribution of μ-mesons is so much flatter than that of the electrons, that corrections for the μ-mesons are greater than 10% only at distances beyond 250 m.

$\dagger\ E_n(x)=\int_1^\infty \exp(-xu)\,u^{-n}\,du.$

Probably the best determined feature of our distribution for comparison with theory is the slope at about 100 metres, i.e. $r/r_1 = 1{\cdot}25$ where r_1 is 80 m. The theoretical distribution behaves like $r^{-\alpha}$ where α is as follows:

S	1	1·4	2·0
α	3·2	2·5	1·6

The observed value is $\alpha = 2{\cdot}25 \pm 0{\cdot}4$. This may be compared with the value of $\alpha = 2{\cdot}7$ found by Dobrotin *et al.* (1956) at 3860 metres for $r/r_1 = 1{\cdot}5$.

With the present apparatus we have no way of determining the distribution at distances less than about 50 metres. This is a rather important region, because according to the Nishimura and Kamata distribution more than one-third of the particles are contained in it. However, if the normalization is made at about 70 metres, the determination of the mean number of particles assuming the Nishimura and Kamata distribution is not sensitive to the choice of S. Moreover, an independent method (to be reported later, papers V and VI) of determining the number of particles which is substantially unaffected by their distribution gives good agreement with the above figures and thus provides confirmation of the general correctness of the Nishimura and Kamata distribution for these showers.

According to shower theory S determines both the rate of absorption of the particles and the structure. It appears that all measurements that have been made on the structure and absorption of showers, at all energies and altitudes up to 3860 metres, have given the same result, although the accuracy of the measurements is admittedly not high. This statement applied to showers in the energy region 10^{15} ev has been discussed by Greisen (1956). We have now to consider that it is also true for energies near 10^{17} ev.

At the lower energies there are good reasons to believe that the electrons detected at sea level come from π^0 mesons produced in the nucleonic cascade relatively close to the ground (Greisen 1956, Dobrotin *et al.* 1956). It is, of course possible, as some models of the nucleon cascade suggest, that at higher energies ($> 10^{16}$ ev) the electrons at sea level come from π^0 mesons produced in the first few collisions. It would be possible to choose multiplicities in the early collisions so that the shower at sea level would have the observed structure and absorption. Against this, however, is the fact that at these high energies the absorption would be decreasing with increasing energy, in conflict with our measurements of barometer coefficients, which are constant, or even increasing with increasing energy (paper VII). Moreover, we would expect that the ratio of nucleons to electrons would be decreasing with number of electrons if the early collisions were making large contributions to the electron component at sea level. This is not borne out by the few measurements that exist (Nikolsky 1956).

References

Barrett, P. H., Bollinger, L. M., Cocconi, G., Eisenberg, Y., Greisen, K., 1952, *Rev. mod. Phys.*, **24**, 133.

Dobrotin, N. A., Zacepin, G. T., Nikolsky, S. I., Hristiansen, G. B., 1956, *Supp. Nuovo Cim.*, **4**, 635.

Greisen, K., 1956, *Progress in Cosmic Ray Physics*, Ed. J. G. Wilson.

Nikolsky, S. I., 1956, *Oxford Conference on Air Showers*, A.E.R.E., Harwell.

Observations on Extensive Air Showers
IV. The Lateral Distribution of Penetrating Particles†

By N. A. Porter, T. E. Cranshaw and W. Galbraith
Atomic Energy Research Establishment, Harwell

[Received March 21, 1957]

Abstract

The lateral distribution of the penetrating component has been measured in showers containing more than 3×10^6 charged particles. Between 300 and 500 metres, the distribution follows a power law with exponent 1·5, and falls more steeply beyond 500 metres. The median spread of the particles is about 500 metres. The interacting component falls off more steeply, and was not detectable beyond 150 metres. About 8·5% of all the particles are penetrating, and of these, about 10% are interacting.

The results are compared with theoretical models, and good agreement is obtained with the predictions of Rozental, based on a Fermi model of the nuclear interaction. The results appear to be in conflict with the hypothesis that the primaries of air showers might be high energy dust grains.

---

§ 1. Introduction

The penetrating component in extensive air showers is of interest because it is more directly descended from the primary interaction than is the electron–photon component, which appears at sea level as a superposition of many secondary cascades. Theories of the nuclear cascade, which gives rise to both components, have been published by Messel (1951, 1954), Rozental (1952) and other authors. Among the predictions of the theories which may be tested experimentally are the proportion (k) of penetrating particles in showers, the numbers of μ-mesons and interacting particles, and the distribution of these components relative to the shower axis. Experimental measurements of these quantities have been made by many authors (e.g. Janossy and Broadbent 1948, McCusker and Millar 1951, Cocconi *et al.* 1949, Eidus *et al.* 1952). Most of this work referred to showers containing less than 10^6 particles at sea level.

The object of the experiment described here was the determination of the distribution of μ-mesons in showers containing more than 3×10^6 particles at sea level, at distances up to 1 km from the axis; and an approximate derivation of the total number of μ-mesons and interacting

† Communicated by the Authors.

particles in the showers. The array constructed at Culham by Cranshaw and Galbraith (1957, referred to subsequently as I) was used for the selection of showers.

Fig. 1

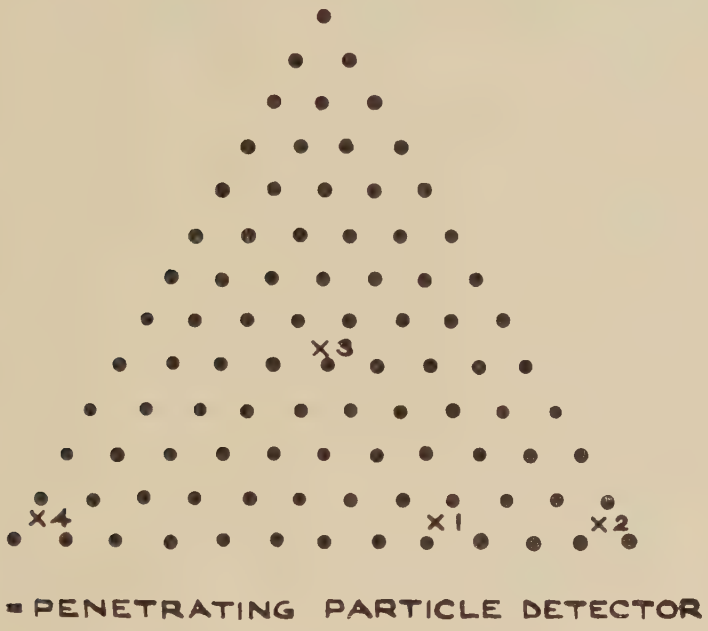

Position of shielded detectors on the array.

Fig. 2

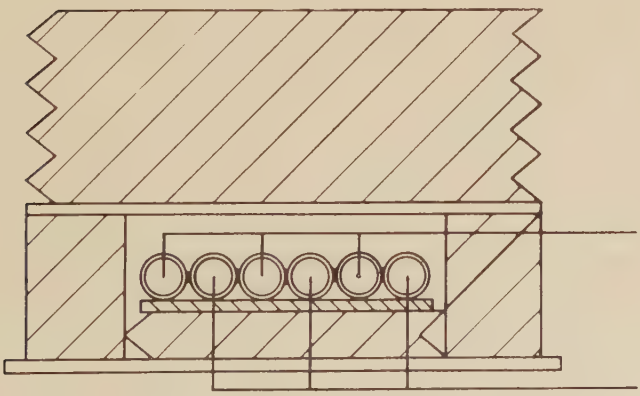

§ 2. Experimental Arrangement

Four shielded particle detectors were used. Their positions on the array are shown in fig. 1, and a diagram of one of the detectors in fig. 2. It had six 200 cm² G.M. counters, enclosed individually in lead pipes

4 mm thick. The counters were connected alternately, in two banks of three, to quenching and blocking oscillator circuits, and were shielded by 20 cm of lead above them, 10 cm at the sides, and 5 cm beneath. Methods of monitoring the operation of the counters were similar to those described in I.

Either of the single banks could be triggered by a single μ-meson of energy >450 MEV. Both banks could be struck in coincidence by :

(*a*) Two μ-mesons.

(*b*) An interacting particle producing two or more charged secondaries in the lead.

(*c*) A single μ-meson producing a knock-on electron or soft shower in the lead.

(*d*) A single μ-meson incident at an angle $>40^\circ$ to the zenith.

The probability of observing a (*c*)-type event was reduced to less than 1% by the lead pipes (Janossy and McCusker 1949) and these events as, well as those of type (*d*), have been neglected in the analysis. The interaction probability in the lead for a nucleon incident vertically was 0·77, assuming a geometric mean free path, and the energy required to produce two detectable secondaries, of the order of 3×10^9 ev (Camerini *et al.* 1951). The possibility of electrons or photons triggering the counters through a cascade in the lead was neglected, since a particle of about 10^{12} ev is required to produce, on average, one electron at a depth of 20 cm.

Signals from the detectors were transmitted to the control unit, and if in coincidence with a shower, recorded on the same punched card. The shielded units took no part in the selection of showers.

§ 3. Analysis of Observations

Lateral distributions of μ-mesons have been derived assuming that :

(*a*) Particles are not associated in pairs or groups over an area comparable with that of a shielded detector.

(*b*) Showers are single-cored, with horizontal circular symmetry.

(*c*) The core of each shower is coincident with the centroid of the units struck on the main array, assigning equal weight to each ' a ' coincidence, and neglecting information from the small ' b ' counters.

(*d*) Edge effects, arising from the finite size of the array, are negligible.

The validity of these assumptions will be considered in § 5. The centroid of each shower was determined with a simple analogue computer, which operated directly from the punched cards.

To determine the distributions, annuli were drawn about each detector, and showers grouped according to the annulus in which the centroid fell.

Assuming first that μ-mesons are the only type of penetrating particle present, then for each detector, if :

N_1=number of single bank penetrating events with coincident centroids in a given annulus,

N_2=number of double bank penetrating events with coincident centroids in a given annulus,

N_T=total number of showers with centroids in the annulus,

then the density (ρ) of μ-mesons at a distance from the centroid equal to the mean radius of the annulus is given approximately by :

$$(N_1+N_2)/N_T=\{1-\exp(-\rho A)\} \quad . \quad . \quad . \quad . \quad . \quad (1)$$

where A is the total sensitive area of the detector. Expression (1) is not strictly true, since ρ is distributed within the annulus, and $\{1-\exp(-\bar{\rho}A)\}$ is not exactly equal to $\overline{\{1-\exp(-\rho A)\}}$, but it has been shown previously (Cranshaw *et al.* 1957, referred to as III) that the approximation is satisfactory, provided ρA is less than about 0·25. For higher densities a correction may be applied.

Now if only μ-mesons were present the number of double bank coincidences N_c would be given by :

$$N_c/N_T=\{1-\exp(-\rho A/2)\}^2 \quad . \quad . \quad . \quad . \quad . \quad . \quad (2)$$

where ρ is derived from (1). Since interacting particles also occur the experimental value of N_2 is greater than N_c. A better value for the μ-meson density is given by :

$$(N_1+N_c)/N_T=\{1-\exp(-\rho A)\} \quad . \quad . \quad . \quad . \quad . \quad (3)$$

and the mean density of interacting particles, η, at the same distance from the centroid, by :

$$(N_2-N_c)/N_T=\{1-\exp(-\epsilon\eta A)\} \quad . \quad . \quad . \quad . \quad . \quad (4)$$

where ϵ is the efficiency for detection of an interacting particle as a double bank event. Experimentally, both the interacting particle density η, and the correction for the distribution of ρ, were negligible for distances greater than 150 metres from the shower centroid.

A correction was applied for the chance coincidence rate between the shielded detectors and showers observed on the array. This was determined from the test cards, produced artificially at half-hour intervals. It was 0·25% of the total number of showers observed, for each detector, and was subtracted for each annulus, according to the number of shower centroids observed within it. The correction to the number of penetrating particles was about 5% for most of the annuli, but rose to about 40% at distances greater than 800 metres from the detector.

Possible distortions of the lateral distribution, arising from geomagnetic deflections of the μ-mesons in flight, were neglected, since the expected effects were small ; a study of events from the central detector (3 in fig. 1) showed no preferred direction for showers relative to the detector.

§ 4. Results

4.1. *μ-Mesons*

Approximately 11 000 showers have been analysed, with a total of 722 penetrating events in coincidence, from all four detectors. The distribution of these events relative to the detectors have been given in detail previously (Porter and Sherwood 1957). Annuli of 84, 105, or 126 metres width were used for analysis. Showers were analysed in two groups, $\geqslant$3-folds, containing on average $6{\cdot}7\times10^6$ charged particles, and $\geqslant$8-folds, with $2{\cdot}7\times10^7$ particles (see paper III).

Densities derived from the observations are shown in fig. 3 as a function of distance from the axis. The distribution $\rho=Kr^{-(n+ar)}$ has been fitted to the points. Expressing ρ in particles/metre^2, and r in metres, the best values of K, n and a, are :

$\geqslant$3-folds $K=61^{+27}_{-19}$
$n=0{\cdot}825$
$a=0{\cdot}000417$ metres^{-1}.

Mean Standard Error in $(n+ar)=\pm0{\cdot}095$.

The $\geqslant$8-fold results could be fitted to the $\geqslant$3-fold distribution, normalizing K, and are statistically compatible with it on a χ^2 test. The dotted curve in fig. 3 is the distribution of all charged particles in $\geqslant$3-folds.

Total numbers of μ-mesons in the showers can be found by integrating the experimental distributions : $N_\mu=\int_0^\infty 2\pi\rho\, r\, dr$. The distributions are determined only for $r=40$–1000 metres, and the total numbers of μ-mesons within these limits, with the contributions added on extrapolating the distributions, and the proportion of μ-mesons in the showers, are shown in the table.

Number and Proportions of μ-Mesons (r in Metres)

Shower size	Experimental $r=40$–1000	Extrapolated		Estimated total number	Fraction of all particles
		$r=0$–40	$r>1000$		
$\geqslant$3-folds	$(4{\cdot}3+2{\cdot}1)\times10^5$ ($-1{\cdot}5$)	$1{\cdot}5\times10^4$	$1{\cdot}3\times10^5$	$(5{\cdot}7\pm2{\cdot}3)\times10^5$	$0{\cdot}085\pm0{\cdot}035$
$\geqslant$8-folds	$(1{\cdot}9+1{\cdot}4)\times10^6$ ($-0{\cdot}8$)	$7{\cdot}6\times10^4$	$3{\cdot}3\times10^5$	$(2{\cdot}3\pm1{\cdot}3)\times10^6$	$0{\cdot}085\pm0{\cdot}049$

The root-mean-square spread of the μ-mesons, which is the quantity usually predicted by cascade theory, is difficult to measure, since it is sensitive to contributions from large distances. In the measured region, the r.m.s. spread is about 530 metres, for both $\geqslant$3-folds and $\geqslant$8-folds. If the distributions are extrapolated to infinity, the spread becomes about 1000 metres in both cases. This is probably greater than the true value. The median spread may be determined more accurately. It is about

500 ± 100 metres for both classes of shower size, assuming the distributions to hold beyond $r = 1000$ metres, and about 400 metres in the measured region itself.

4.2. *Interacting Particles*

The array is unsuitable for the study of the distribution of interacting particles (I.P.) in the showers, since the density falls off rapidly from the axis, which is difficult to locate to an accuracy better than about 50 metres. The total number of I.P. in the showers may, however, be determined without deriving the structure function.

Consider a detector of area A, near the centre of an array of area B. If in a time t, the number of shower cores detected by the array $= C$, and the number of coincident I.P. detected $= I$, then the rate of shower cores $R_c = C/tB$ per unit area unit time, and the rate of interacting particles $R_I = I/tA$ per unit area/unit time. The rate of cores in an infinitesimal annulus of radius r, dr, about the detector, is $dR_c = R_c \times 2\pi r\, dr$ per unit time. The rate of I.P. at the detector due to showers with cores within the annulus, is $dR_I = 2\pi r R_c \rho\, dr$, per unit area/unit time. The total rate of I.P. due to cores anywhere on the array is then

$$R_I = R_c \int_B 2\pi r\, \rho\, dr \approx R_c \int_0^\infty 2\pi r \rho\, dr = R_c N/\text{unit area/unit time},$$

where N is the total number of I.P. in a single shower. The integral over the array can be put equal to the integral from 0 to ∞, since the spread of the interacting component is small compared with the array. The total number of I.P. in the shower is now $N = R_I/R_c = IB/CA$.

The mean number of interacting particles in $\geqslant$3-fold showers has been determined by this method. Only 20 events were available which could be ascribed to I.P., from detector 3 in the centre of the array. This corresponds to a total number $N = (4{\cdot}1 + 2{\cdot}1) \times 10^4$ *particles*. No reliable estimate could be made for $\geqslant$8-fold events. Further measurements on the interacting component are in progress. Interacting particle densities could be determined only at two distances from the axis. These are shown in fig. 3 with the distribution $\rho \propto r^{-1{\cdot}5}$, which is consistent with the results.

§ 5. Discussion

5.1. *Validity of the Assumptions*

(*a*) The assumption that penetrating particles are not locally correlated is justified by the experimental observation that double bank penetrating events occur only in the region where they would be expected from considerations of μ-meson and interacting particle density, and not in parts of the shower distant from the centroid.

(*b*) The assumption that the showers are single-cored, appears, from a visual examination of the patterns produced, to be valid for the majority of events. About 0·5% of the events do not conform with this pattern

(Cranshaw 1956) but the effect of including these in the analysis is negligible. The assumption that showers have horizontal circular symmetry is of course invalid, since the zenith angle of incidence may be appreciable. The effect of oblique incidence on the observed lateral distribution has

Fig. 3

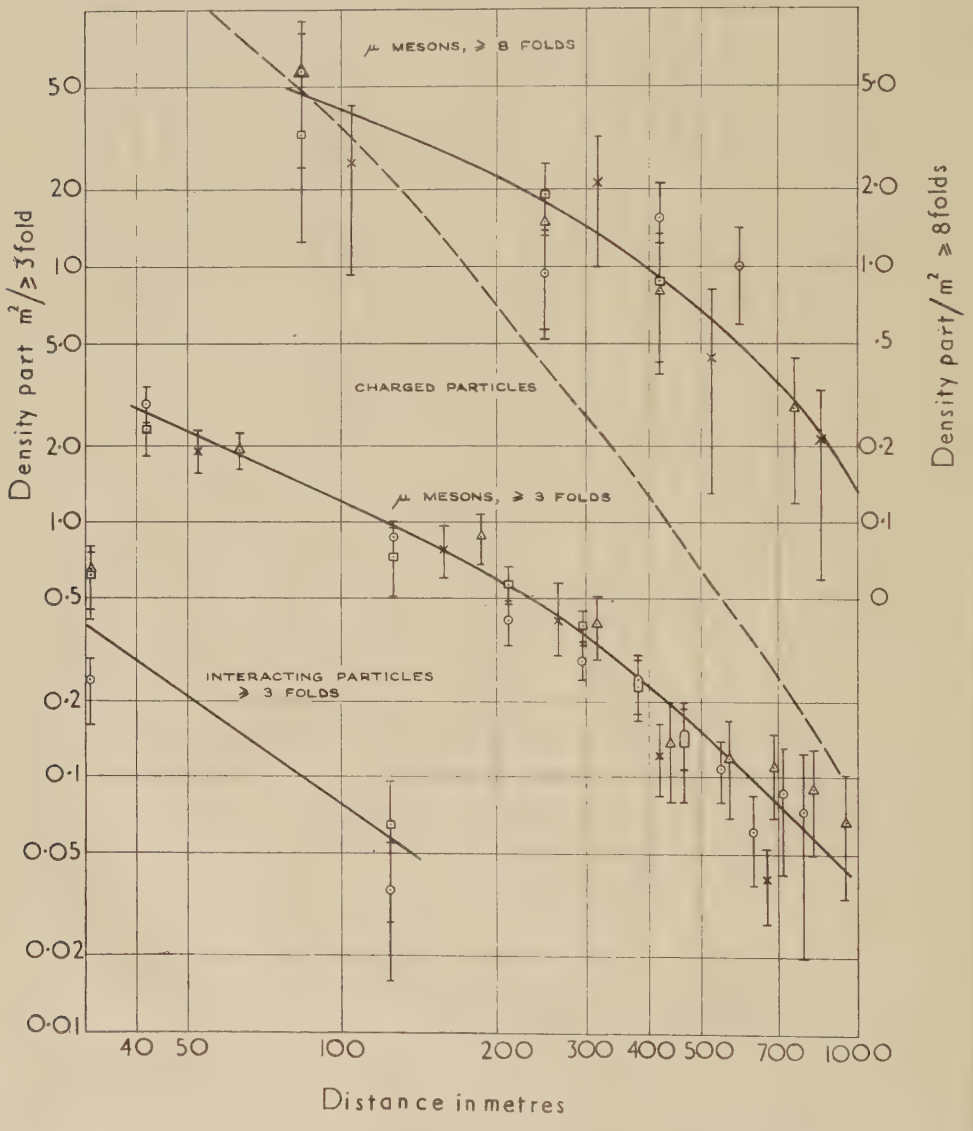

been calculated, using a zenith angle dependence of $I = I_0 \cos^6 \theta$, for a μ-meson distribution of the form $\rho = Kr^{-n}$, with n varying between 0·5 and 2·0. The zenith angle dependence was determined from observed barometer coefficients. The contribution from oblique showers leads to an underestimate of the true μ-meson densities by about 5%, but does not

distort the form of the distribution. This correction has not been applied to the results given in fig. 3. A more serious source of error may arise from a change in the true value of k in oblique showers. The proportion of μ-mesons probably increases with zenith angle, since the absorption length for μ-mesons is greater than that for the electron photon cascade. This will give rise to an experimental over-estimate of the absolute number of μ-mesons in vertical showers, but would not be expected to alter the form of the distribution from that which would be observed if only vertical showers were present.

(*c*) and (*d*) The assumptions that the centroid of the units struck is a good approximation to the shower core, and that edge effects are negligible, is justified experimentally by the consistency of the results from different detectors. Each of these, if analysed separately, give distributions close to the mean, in the $\geqslant$3-fold showers. In the $\geqslant$8-folds, the deviations are greater, but since the statistics are poor, the differences may reasonably be ascribed to fluctuations.

The neglect of effects due to knock-on electrons or oblique μ-mesons may again be justified experimentally by the small number of double bank events observed. Spurious events of this type should occur as a proportion of the total number of single bank coincidences observed, and since very few double bank coincidences occurred for $r>150$ metres, the effect should be small also at short distances from the axis.

5.2. *Comparison with Previous Experiments*

The results are in qualitative agreement with previous observations on somewhat smaller showers. The increase in the proportion of penetrating particles with distance from the axis was reported by Eidus *et al.*, and the proportion of interacting particles is consistent with that found by Vavilov *et al.* (1955).

The form of the μ-meson distribution is slightly different from that reported by Zatsepin (1956), who found a distribution $\rho=Kr^{-\nu}$, with $\nu=0{\cdot}5$ for $r=0$–50 metres, and $\nu=2$ for $r=300$-500 metres, in showers of 10^5–10^6 particles. The distribution $\rho=Kr^{-(n+ar)}$ is tangential at any point to a distribution $\rho=Kr^{-\nu}$, where $\nu=d(\log\rho)/d(\log r)=-(n+ar+ar\ln r)$. For $\geqslant$3-fold showers the best value of ν for $r=300$–500 metres is $\nu=1{\cdot}48\pm0{\cdot}06$. The slope could not be measured for $r=0$–50 metres.

5.3. *Comparison with Theory*

The results are in reasonable agreement with the predictions of Rozental (1952 *loc. cit.*) using a model of the nuclear interaction similar to that suggested by Fermi (1951, a, b). The ratios of penetrating particles to electrons, and of interacting particles to μ-mesons, are predicted for showers containing 7×10^5 particles at sea level :

$$\frac{N_{p.p.}}{N_e}=0{\cdot}1, \qquad \frac{N_I}{N_\mu}=0{\cdot}1.$$

Experimental values for $\geqslant$3-folds are :

$$\frac{N_{p.p}}{N_e} = 0{\cdot}095 \pm 0{\cdot}039, \qquad \frac{N_I}{N_\mu} = 0{\cdot}07 \pm 0{\cdot}04.$$

The comparison of theory with somewhat larger showers is probably justified, since only ratios of numbers are considered. The predicted r.m.s. spread of the μ-mesons is 600 metres, in reasonable agreement with experiment. The detailed form of the distribution and its median spread, are not given.

Other models of the nuclear interaction cannot be excluded by the experimental results. Unfortunately, detailed predictions of the μ-meson distribution arising from a plural type of cascade (Heitler and Janossy 1949) or taking into account the tunnel effect in the nucleus (Roesler and McCusker 1953) are not available.

The results seem difficult to reconcile with the suggestion of Alfven and Herlofson (1956) that the large showers may be caused by primary dust grains, however. In this model the primary contains 10^3–10^6 atoms, each carrying 10^{12}–10^{14} ev/nucleon. The proportion of μ-mesons predicted between $r=0$–200 metres is about five times greater than that found experimentally, and is only about 50% greater at the core than at 200 metres. Between 200 and 1000 metres the form of the distribution resembles the experimental result, but the proportion of μ-mesons is again higher.

The agreement with the theory of Budini and Moliere (1953) is also poor.

§ 4. Conclusion

The distribution of μ-mesons in showers containing about $6{\cdot}7 \times 10^6$ particles, and produced by primaries of estimated energy 5×10^{16} ev has been determined with moderate accuracy, between 50 and 1000 metres from the shower core. It may be fitted to a law of the form $\rho = Kr^{-(n+ar)}$. The determination of the total number of μ-mesons in the showers, and their median spread, is dependent on the extrapolation of the law beyond 1000 metres, where, if it is assumed to hold, a further contribution of about 20% is made to both these quantities. The root-mean-square spread is sensitive to the contribution from beyond 1000 metres, and cannot be reliably determined. The distribution of μ-mesons in the group of larger showers, containing about $2{\cdot}7 \times 10^7$ particles, follows a similar law, though it may be slightly less steep in the region $r=0$–400 metres. The proportion of interacting particles appears similar to that found at lower primary energies.

The qualitative similarity between these results and the work on smaller showers seems to indicate that the basic nature of the nuclear interactions does not change between 10^{16} and 5×10^{17} ev. Perhaps the most significant feature of the work is the disagreement between experiment and the primary dust grain model. The agreement with a theory based on Fermi's model of meson production is reasonably good, but it seems likely

that a model in which the interactions are elastic could give equally good agreement with experiment. This ambiguity could be at least partially resolved if the altitude of μ-meson production were known.

References

Alfven, H., and Herlofson, N., 1956, *Proceedings of the Oxford Conference*, April (A.E.R.E. Publication).

Budini, P., and Moliere, G., 1953, *Kosmische Strahlung*, Ed. W. Heisenberg (Berlin: Springer).

Camerini, U., Davies, J. H., Fowler, P. H., Franzinetti, C., Muirhead, H., Lock, W. O., Perkins, D. H., and Yekutieli, G., 1951, *Phil. Mag.*, **42**, 1241.

Cocconi, G., Tongiorgi, V. C., and Greisen, K., 1949, *Phys. Rev.*, **75**, 1063.

Cranshaw, T. E., 1956, *Proceedings of the Oxford Conference*, April (A.E.R.E. Publication).

Cranshaw, T. E., and Galbraith, W., 1957, *Phil. Mag.*, **2**, 804.

Cranshaw, T. E., Galbraith, W., and Porter, N. A., 1957, *Phil. Mag.*, **2**, 891.

Eidus, L. K., Adamovich, M. I., Ivanovskaya, I. A., Nikolaev, V. S., and Tulyankina, M. S., 1952, *Z. exp. Teor. Fiz.*, **22**, 440.

Fermi, E., 1951 a, *Progr. theor. Phys.*, **5**, 570; 1951 b, *Phys. Rev.*, **81**, 863.

Heitler, W., and Janossy, L., 1949, *Proc. phys. Soc. Lond.*, **62**, 374.

Janossy, L., and Broadbent, D., 1948, *Proc. roy. Soc.*, **192**, 364.

Janossy, L., and McCusker, C. B. A., 1949, *Nuovo Cim.*, **6**, Suppl. 535.

McCusker, C. B. A., and Millar, D. D., 1951, *Proc. phys. Soc. Lond.*, **64**, 915.

Messel, H., 1951, *Comm. Dublin. Inst.*, A.7.

Messel, H., 1954, *Progress in Cosmic Rays*, Vol. II., Ed. J. G. Wilson (Amsterdam: North-Holland).

Porter, N. A., and Sherwood, A. C., 1957, *A.E.R.E. Report* NP R.2110.

Roesler, F. C., and McCusker, C. B. A., 1953, *Nuovo Cim.*, **10**, 127.

Rozental, I. L., 1952, *Z. exp. Teor. Fiz.*, **23**, 440.

Vavilov, Y. N., Nikolskii, S. I., and Sarantsev, V. P., 1955, *Z. exp. Teor. Fiz.*, **28**, 505.

Zatsepin, G. T., 1956, *Proceedings of the Oxford Conference*, April (A.E.R.E. Publication).

Fusion Induced by Mu-Mesons†

By T. H. R. Skyrme
Atomic Energy Research Establishment, Harwell, Didcot, Berks.

[Received May 1, 1957]

Abstract

An experiment has recently been reported from which it has been inferred that the (p, d) reaction is catalysed by the presence of mu-mesons forming mesic atoms and molecules. A brief analysis is made in this note of the reaction rates necessary to explain the experimental results. The relatively large number of events observed in which the meson takes away the energy released in the reaction can be understood as the result of conversion of an electric monopole transition.

§ 1. Introduction

Alvarez *et al.* (1956) have reported the following experiment. Mu-mesons, arising from the decay of pions from the Berkeley cyclotron, were slowed down and stopped in a liquid hydrogen bubble chamber. A number of events were observed in which the meson came to the end of its normal range, and then apparently was re-ejected with an energy of about 5·4 Mev ; on one or two occasions this behaviour was observed twice in succession. These events were interpreted as evidence that the nuclear reaction

$$p+d \rightarrow {}^3He+5{\cdot}4 \text{ Mev}$$

was occurring with appreciable frequency following the formation of a molecule in which the proton and deuteron are bound closely together by the meson ; the excess energy was carried off by the meson.

The experiment was repeated with hydrogen enriched in deuterium ; the number of events observed increased with increasing concentration in the manner shown in table 1, which contains the data given by Alvarez. The first line gives the reciprocal concentration of deuterium, the second the number of mesons observed to stop in the chamber, and the third the number of events of the above type. The last line is given by a semi-empirical formula for the number of events, discussed in § 2.

When a meson is stopped in condensed material it is captured into the Coulomb field of some nucleus, and falls rapidly into the lowest 1S orbit,

† Communicated by Dr. B. H. Flowers. Since completion of this paper the author has received a preprint of a similar analysis by J. D. Jackson (*Phys. Rev.* (in the press)).

as was shown by Fermi and Teller (1947). The mesic atom formed in this way with a nucleus of unit charge is a small neutral system that can easily diffuse through matter; the repulsive Coulomb field is largely shielded by the meson, so that interactions with other nuclei can occur more readily.

This shielding effect is not however sufficient by itself to explain the observed frequency of reactions. The intrinsic probability of the (p, d) reaction should be very nearly equal, at least at thermal energies, to that of the mirror (n, d) capture reaction. The latter has a cross section of 0·46 mb at the neutron velocity of $2{\cdot}2\times10^5$ cm/sec which gives

$$v\sigma\simeq10^{-22}\ \mathrm{cm^3\ sec^{-1}}.$$

The particle density of liquid hydrogen is about $4{\cdot}2\times10^{22}$ nuclei per $\mathrm{cm^3}$; so that even with complete neglect of the Coulomb barrier the reaction rate would only be of the order of a few per second, with a negligible

Table 1

$1/c$	5000	333	20
Mesons stopped	2500	1600	1000
Events	18	38	30
Formula (2)	16	40	31

chance for the reaction during the lifetime of the meson, 2·2 μsec. If however the proton and deuteron are bound together in a mesic molecule, the local density will be increased by something of the order of $(207)^3$, 207 being the ratio of mesic to electronic masses; then the reaction can occur at a rate comparable with the mesic decay rate.

These considerations were pointed out by Zeldovich (1954), who also made an estimate of the rate at which molecules might be formed. He found that the rate was small unless there were a molecular level close to the dissociation threshold so that there was a resonance effect, and he estimated that the first vibrational level was near this position. A precise estimate is clearly not possible without an accurate calculation of the three-body molecular system.

In § 2 we make a phenomenological analysis of the course of the atomic and nuclear reactions; we find that the experimental results collected in table 1 yield two relations between the various reaction rates. In § 3 we consider briefly the atomic reaction rates, and in § 4 the nuclear ones; there the main problem is to understand the frequency with which the reaction energy is taken off by the meson, rather than by radiation. This can be understood as the result of a monopole transition present in addition to the magnetic dipole one that is responsible for most of the capture of neutrons by deuterium.

§ 2. Phenomenological Description

The lifetime of the mu-meson is 2·2 μsec. and the reciprocal, the decay rate, will be denoted by

$$\lambda_0 = 4{\cdot}5 \times 10^5 \text{ sec}^{-1}.$$

Consider now the history of one meson stopping in the liquid hydrogen, with a concentration c of deuterium. After a time negligibly short compared with the lifetime the meson will be captured into the 1S orbit around either a proton or deuteron with probabilities $(1-c)$ and c respectively. The binding energies of these mesic atoms are known precisely from the usual formula ; there is an appreciable difference between them due to the different reduced masses of the meson in the two cases. The binding energy of the molecules can only be estimated rather crudely, because the adiabatic approximation that is good enough for the electronic case may be appreciably in error with mesons. The main part of the molecular binding will scale up in proportion to the reduced mass of the meson, but the (negative) contribution of the zero-point vibrational energy scales as the $\frac{3}{2}$ power of the mass. These estimates of binding energy are collected in table 2.

Table 2

Mesic atom or molecule-ion	$(H)_\mu$	$(D)_\mu$	$(HH)_\mu^+$	$(HD)_\mu^+$	$(DD)_\mu^+$
Binding energy, ev	2542	2677	2824	2941	3038

The mesic deuterium will end its life either by decay of the meson or by formation of a molecular-ion. In addition the mesic hydrogen may exchange its meson with a deuteron, and this is likely to be much faster than molecule-formation. The rate for this exchange reaction will be proportional to the concentration c, and will be denoted by $c\lambda_e$.

The rate of formation of the different molecules will be different apart from the concentration factors because of the effects of the different masses. These rates will be denoted as follows :

for $(H)_\mu$ to form $(HH)_\mu^+$: $(1-c)\,\lambda_{m2}$,
for $(H)_\mu$ to form $(HD)_\mu^+$: $c\lambda_{m3}$,
for $(D)_\mu$ to form $(HD)_\mu^+$: $(1-c)\,\lambda_{m3}$,
for $(D)_\mu$ to form $(DD)_\mu^+$: $c\lambda_{m4}$.

Once a mesic molecule-ion has been formed it will persist until either the meson decay or a nuclear reaction occur.

With the reaction rates defined above the number of $(HD)^+$ formed from one meson stopping is easily found to be

$$N = \frac{c(1-c)\lambda_{m3}\,[\lambda_e+\lambda_{m3}+2\lambda_0+(1-c)\lambda_{m2}+c\lambda_{m4}]}{[\lambda_0+(1-c)\lambda_{m3}+c\lambda_{m4}][\lambda_0+c(\lambda_e+\lambda_{m3})+(1-c)\lambda_{m2}]}. \quad . \quad (1)$$

In this formula we have neglected the possibility that any nuclear reaction

may occur before the molecule is formed. Zeldovich (1954) points out that the same resonance effect that enhances the rate of molecule formation, will also enhance the chance of a reaction 'in flight', that we found previously to be small; but the yield of this mechanism is small compared with that from the molecule.

The energy released in the nuclear reaction may be taken off either by a gamma ray or by the meson; the rates for these two processes in a molecule will be denoted by λ_1 and λ_2 respectively. If the reaction is radiative the meson in the molecular orbit will almost certainly be retained in an orbit around the final ^{3}He nucleus, because the recoil velocity of that nucleus is small, being only about 1/10 of the orbital velocity of the meson; there it will remain until it decays. On the other hand when the meson is ejected with 5·4 Mev it will go again through the same cycle of reactions. Accordingly the number of events (in which a meson is ejected) to be expected for every meson coming into the chamber equals

$$Y=\frac{N\lambda_2}{\lambda_0+\lambda_1+\lambda_2(1-N)}.$$

For small concentrations c, we can write then

$$1/Y=A+B/c \qquad . \quad . \quad . \quad . \quad . \quad . \quad . \quad . \quad (2)$$

where A and B are certain combinations of reaction rates. Provided λ_e is large compared with λ_0 and the λ_{mi}, we find

$$A+1=[(\lambda_0+\lambda_{m3})/\lambda_{m3}]\,.\,[(\lambda_0+\lambda_1+\lambda_2)/\lambda_2] \qquad . \quad . \quad . \quad (3)$$

and $$B=(A+1)(\lambda_0+\lambda_{m2})/\lambda_e.$$

The data in table 1 can be fitted, within the statistical error, by

$$A=32, \quad B=0{\cdot}025 \qquad . \quad . \quad . \quad . \quad . \quad . \quad . \quad (4)$$

as is indicated by the entries in the last line, obtained by multiplying the number of mesons stopping by $Y(c)$.

Two qualitative conclusions may immediately be drawn from these numbers. The first is that λ_e must be considerably greater than either λ_0 or λ_{m2}; this correlates with the onset of a saturation effect in the number of events at quite low deuterium concentration. The second is that

$$\lambda_2/\lambda_1 \geqslant 1/A=0{\cdot}03$$

which means that internal conversion is quite large: equality will hold only if both λ_{m3}, the rate of molecule formation, and λ_1, the reaction rate, are large compared with the decay rate λ_0.

§ 3. Atomic Reaction Rates

The second of eqns. (3) implies that λ_e must be at least of the order of 10^9 sec^{-1}; which means that for the reaction

$$(\mathrm{H})_\mu+\mathrm{d}\rightarrow(\mathrm{D})_\mu+p+135 \text{ ev}$$

at zero energy the value of $v\sigma$ must be at least 10^{-14} cm^3 sec^{-1}. The only

simple method of estimating such reaction rates is by the use of Born approximation, and in the present case that method leads to the value $v\sigma = 2 \times 10^{-11}$ cm^3 sec^{-1}. It is well known however that the Born approximation usually leads to a gross over-estimate of cross sections at low energies (see, for example, Dalgarno and Yodav 1953).

It is also evident from eqn. (3) that however strong internal conversion may be, the rate of molecule formation λ_{m3} must be greater than $\lambda_0/(A+1) = 1{\cdot}5 \times 10^4$ sec^{-1}. The energy liberated by the formation is most likely to be carried away by an electron, and a reasonable model would be provided by the collision of a mesic deuterium atom with an ordinary hydrogen atom,

$$(\mathrm{D})_\mu + (\mathrm{H})_e \rightarrow (\mathrm{HD})_\mu + e + 250 \text{ ev}$$

using the rough estimate of binding energy adopted in table 2. An estimate of the reaction rate by Born approximation (using a rough model of the molecular wave function) gives $v\sigma \simeq 10^{-23}$ cm^3 sec^{-1}. The much greater rate apparently implied by the experiments, must be due to transitions to excited molecular states more nearly in resonance with the initial state, as was suggested by Zeldovich (1954). We have not tried to estimate these more closely.

§ 4. Nuclear Reaction Rate

In this section we estimate λ_1, the rate for the radiative reaction. We assume that the intrinsic reaction rate is the same as for the mirror reaction, with $v\sigma = 10^{-22}$ cm^3 sec^{-1}; the molecular wave function is some function $\psi(x, r)$ where r is the separation of the nuclei and x is the distance of the meson from their mass-centre. Then

$$\lambda_1 = Pv\sigma = 10^{-22} P \quad . \quad . \quad . \quad . \quad . \quad . \quad . \quad (5)$$

where $P = \int |\psi(x, O)|^2 \, d^3x$ in the 'collision intensity' for the nucleons.

If further we make the adiabatic assumption

$$\psi(x, r) = \phi(x\,; r)\, \chi(r)$$

where $\phi(x\,; r)$ is a normalized wave function for the meson with fixed nucleons and $\chi(r)$ is the wave function of the nucleon motion in an effective potential $V(r)$, then simply

$$P = |\chi(0)|^2. \quad . \quad . \quad . \quad . \quad . \quad . \quad . \quad . \quad (6)$$

Near the position of equilibrium, at the separation

$$\rho = 1{\cdot}06 \text{ Å}/207 = 5 \times 10^{-11} \text{ cm},$$

the potential V may be approximated by an oscillator scaled up from the electronic case, giving

$$V(r) = (207)\,[-2{\cdot}8 + 5{\cdot}4\,(r-\rho/\rho)^2] \text{ ev}.$$

The normalized ground state wave function is then

$$\chi(r) = r^{-1}\,(\omega^{1/2}/4\,\pi^{3/2}\,\rho)^{1/2} \exp\,[-\tfrac{1}{2}\omega\,(r-\rho/\rho)^2] \quad . \quad . \quad . \quad (7)$$

where the numerical value of ω is approximately 3·0. Near $r = 0$, $\chi(r)$

must behave like a Coulomb wave function; we have joined (7) onto a Coulomb function at $r/\rho = 0{\cdot}36$, with a value of $\eta = 1{\cdot}44$; the latter was determined by the strict use of the adiabatic approximation. This led to a value for P according to eqn. (6),

$$P \simeq 10^{28}\ \text{cm}^{-3}$$

and so according to (5) gave $\lambda_1 = 10^6\ \text{sec}^{-1}$, twice the rate of meson decay.

This estimate has been derived by very approximate analysis, but that error is probably less than the error of the adiabatic approximation, which should tend to over-estimate the reaction rate.

It has also been implicitly assumed above that only the S-wave contributes appreciably to the reaction. There is however a small but significant contribution from the P-wave, because the relatively greater value of the electric dipole matrix element partially compensates for the reduced penetration of the wave.

§ 5. Internal Conversion

The remaining problem is to explain the value of λ_2, describing the conversion process actually observed in the experiment. As we saw in § 2, the internal conversion ratio is at least 0·03 from the analysis of the data.

The chief radiative capture process involves a magnetic dipole transition; according to Austern (1952) the amount of mixed electric quadrupole (arising from D-wave components of the wave-functions) in the neutron capture reaction in deuterium is of the order 10^{-5}, and it cannot be much greater for the mirror reaction. However the internal conversion coefficient for M1 radiation of 5·4 Mev and for a mesic He atom is only 10^{-4} (according to Born approximation), and the quadrupole admixture is too small to change this appreciably.

Thus the important conversion process cannot be that of the dominant radiative process. As was mentioned at the end of § 4, there may be a certain amount of E1 radiation due to the nuclear P-wave; since however the molecule as a whole is in an S-state the conversion would then be of a P-wave meson, and therefore far too small.

The remaining possibility arising from the nuclear S-wave is conversion of the (forbidden) electric monopole radiation. As has recently been pointed out by Church and Weneser (1956) this process may compete effectively with other radiations in suitable circumstances. In the present case, since the final nuclear state is doublet, the nuclear spins will be correctly aligned for $\frac{1}{3}$ of the time. This leads to the following expression for the rate of conversion for a meson initially in a 1S He atom orbit, according to Born approximation,

$$\lambda = (1/3)\, P\, (32/9)(e^2/\hbar c)^2(\omega/a^4)\,|(f\,|\Sigma r_p^{\,2}|\,i)|^2 \quad . \quad . \quad . \quad (8)$$

where ω is the frequency of the ejected meson, a is the mesonic Bohr radius, and the monopole matrix element is between the final ^{3}He state and an initial state appropriate to a p–d collision at zero energy and from

which the penetration factor P has been removed ; this initial state can therefore be identified with that for n–d scattering at zero energy, normalized to unit density at large distances.

We have estimated the monopole matrix element in the following way :

(*a*) The final state has been taken in the form const $[\exp(-\gamma\rho)/\rho]$ where ρ^2 is the sum of squares of distances between particles, and γ has been selected to give the right asymptotic behaviour for dissociation into proton and deuteron, since that is the most important part of the wave function in the matrix element.

(*b*) The incident wave, at zero energy, is simply the deuteron wave function, for which the asymptotic form has been used with the correct normalization. The initial state has been put equal to this incident wave less a suitable multiple of the final state, so that the two are orthogonal.

If the deuteron wave is asymptotic to $[\exp(-\alpha r)/r]$, the constant γ determined in the above way is equal to $\alpha/0{\cdot}6$. With these assumptions the matrix element can be evaluated analytically, with the result that from formulae (5) and (8),

$$\lambda/\lambda_1 = 0{\cdot}8\times10^{-4}\,(m_\mu c/\hbar)^7\,|(f\,|\,\Sigma r_p^2\,|\,i)|^2 \sim 0{\cdot}17. \quad . \quad . \quad . \quad (9)$$

This is larger by a factor 6 than the minimum value deduced above ; much of this factor is probably due to the over-estimate of the meson density at the origin made in the adiabatic approximation. That density is about 20 times the density at the same point in the average molecular state.

It is interesting with this value of the monopole matrix element to calculate the corresponding cross section for pair-production. We find that

$$v\sigma = 5\times10^{-26}\ \mathrm{cm^3\ sec^{-1}}$$

about 1/2000 of the rate for the radiative process. Pair-production by conversion of the M1 radiation has a similar rate (cf. Rose 1949).

Acknowledgment

The author is indebted to Professor J. M. Cassels for discussions which led to the analysis presented here.

References

Alvarez, L. W., *et al.*, 1956, UCRL-3620, University of California.
Austern, N., 1952, *Phys. Rev.*, **85**, 147.
Church, E. L., and Weneser, J., 1956, *Phys. Rev.*, **103**, 1035.
Dalgarno, A., and Yadav, H. N., 1953, *Proc. phys. Soc. Lond.* A, **66**, 173.
Fermi, E., and Teller, E., 1947, *Phys. Rev.*, **71**, 31 ; **72**, 399.
Rose, M. E., 1949, *Phys. Rev.*, **76**, 678.
Zeldovich, Ya. B., 1954, *Dokl. Ak. Nauk. S.S.S.R.*, **95**, 493.

The Production of Intense Cold Neutron Beams†

By I. Butterworth, P. A. Egelstaff, H. London and F. J. Webb
Atomic Energy Research Establishment, Harwell

[Received May 1, 1957]

Abstract

The moderation of pile neutrons to very low energies has been investigated. Liquid hydrogen, liquid hydrogen deuteride and methane at 20°K were found to be effective moderators. After an examination of the safety aspects, a volume of liquid hydrogen was maintained at the centre of a reactor, and the velocity spectrum of neutrons scattered from it was measured. Appreciable moderation of neutrons to very low energies was observed. By this method it is practicable to increase considerably the flux of cold neutrons in a beam. Thus, in the present experiment the flux of 10 Å wavelength was increased by a factor of 25.

§ 1. Introduction

From the time that nuclear reactors first provided strong sources of thermal neutrons, the use of neutrons as a tool for physical research has become steadily more widespread. Prominent among the methods employed is the scattering of cold neutrons, that is neutrons with temperatures less than about 60°K (i.e. with wavelengths >4 Å). These cold neutrons have two properties of particular value, their low energy and their long wavelength.

Their low energy makes it practicable to measure the energy transfer which occurs when neutrons are scattered. This is because the energy transfer may be comparable with the initial energy of the cold neutron. From a study of energy transfers new information on the thermal behaviour of solids and liquids can be obtained.

Their long wavelength makes cold neutrons suitable for the study of long range effects, such as fluctuation phenomena, which are of particular interest near the critical point of a phase transition. In addition neutrons of sufficiently long wavelengths do not suffer Bragg reflection. Therefore they are often used in experiments where Bragg reflection would yield a large background of unwanted scattering.

A third factor, which is likely to assume great importance as the field develops, is that a continuous spectrum of cold neutron wavelengths is available. Thus, since cold neutrons are obtained by passing a neutron

† Communicated by the Authors.

beam from a reactor through some form of velocity selector (see e.g. Hughes 1953), it is a simple matter to perform an experiment with neutrons of various wavelengths.

As the velocity spectrum of neutrons from a reactor is very nearly a Maxwell distribution corresponding to the pile temperature, the flux of cold neutrons is relatively small; for example only about 1% of the neutrons in a beam from the Harwell reactor BEPO have wavelengths greater than 4 Å. The fact that only low fluxes are available has limited the use of cold neutrons. If, however, one could bring the neutrons into thermal equilibrium with a moderator at low temperature, thus shifting the whole Maxwell distribution to lower temperatures, the cold neutron flux would be greatly increased.

The use of cooled moderators with cyclotrons is well known (e.g. Sutton *et al.* 1947, and Squires and Stewart 1955); in particular Sutton *et al.* investigated the use of liquid hydrogen as a moderating material. In this application, however, it is possible to cool a large volume of moderator, whereas in a reactor the volume which could be used would be severely limited by the need to situate the moderator in a high neutron flux, i.e. near the core of the reactor, where the space available for apparatus is small. In most materials there would be little moderation to very low energies in the volume available since cross sections for inelastic neutron scattering fall as the neutron energy becomes comparable with the atomic binding energy of the moderator. If a material is to act as a low temperature moderator, it must have a high free-atom cross section for neutron scattering, a weakly bound structure and also a small absorption cross section.

In a preliminary experiment (§ 2) we showed the feasability of moderating neutrons to low energies. Of the moderators found to be effective liquid hydrogen was the most convenient to use. Therefore, after studying the safety of putting liquid hydrogen in a reactor (§ 3), we maintained a volume of liquid hydrogen at the centre of the BEPO reactor. The velocity spectrum of neutrons scattered from the hydrogen was measured. This confirmed that liquid hydrogen was effective in producing large fluxes of cold neutrons.

§ 2. Preliminary Experiments

In the absence of data on cold neutron cross sections, the material which will most efficiently moderate neutrons to low energies and the form in which it should be used are not obvious. A simple experiment was therefore carried out to compare the moderating efficiencies of different materials.

2.1. *Apparatus*

The cryostat used for these experiments was similar to the apparatus later used in the reactor (§ 4) and is shown in fig. 1. The moderator under investigation was contained in a chamber 7·5 cm in diameter and 10 cm long. This was cooled by contact with a second chamber containing a coolant. The chambers were enclosed in a vacuum case.

The cryostat was surrounded by wax in form of a cylindrical block 45 cm diameter and 60 cm long. In the wax, four 250 mc polonium–beryllium neutron sources were buried at evenly spaced points about the cryostat on an 18 cm diameter circle. This circle was 2·5 cm above the level of the bottom of the moderator chamber. Thus neutrons reaching the moderator chamber had traversed at least 4 cm of wax. Measurements with a BF_3 counter at the position of the moderator chamber confirmed that the fluxes of thermal and epi-thermal neutrons falling on the chamber were in roughly the same ratio as in a reactor.

Fig. 1

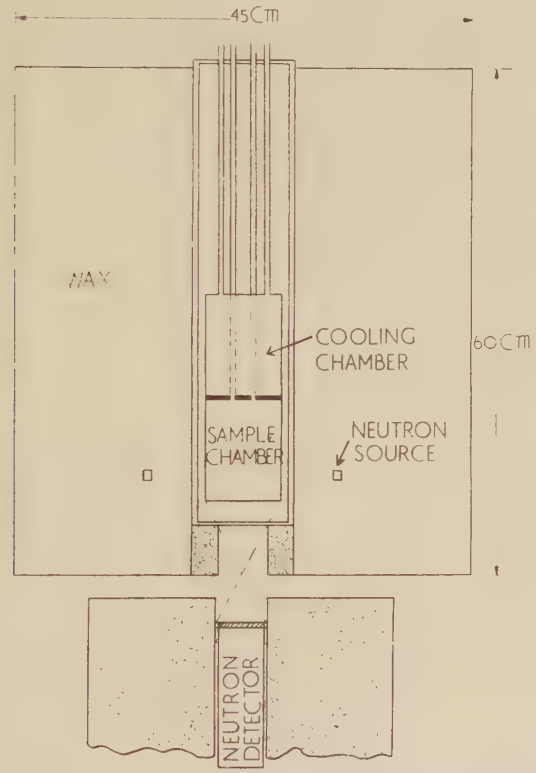

Apparatus used in preliminary experiments.

Neutrons scattered by the moderator through a collimator formed an external beam. Collimation was such that only neutrons coming from the direction of the moderator reached the neutron detector placed below the wax block.

Because the beam intensity was very low we could not use a neutron velocity selector, and therefore we could only measure an average neutron energy for the beam. This was deduced from the attenuation of the beam by a gold sheet, $\frac{1}{2}$ mm thick. On the assumption that the distribution of neutrons was Maxwellian, the temperature of this distribution

was calculated ; we call this the ' apparent beam temperature '. If the velocity distribution is not Maxwellian (and later measurements, § 5, show that in general it is not) this temperature has no absolute significance, but it does serve to indicate average neutron velocity and can be used to compare the efficiency of different moderators.

With the moderator chamber filled with pentane at 293°K we verified that the apparent beam temperature was correct, viz. 294±10°K.

2.2. *Results*

Extensive measurements were made on liquid hydrogen since this appeared to be the most promising moderator.

First, the variation of beam intensity with the depth of hydrogen in the cryostat was measured. It was found that the intensity was almost independent of the depth of hydrogen providing this exceeded 2 cm.

Figure 2 shows the apparent temperature of a beam scattered from liquid hydrogen at 20°K as a function of the relative proportions of ortho- and para-hydrogen. The moderation efficiency is seen to vary little over the range : 10% to 75% of ortho-hydrogen.

Table 1. Apparent Beam Temperatures obtained with Various Moderators (in °K)

Moderator \ Temperature of moderator °K	90	77	20	4
Pentane	—	135±14	121±15	—
Methane	135±5	134± 7	75± 6·5	65±8
Methyl alcohol	—	173±19	135±17	—
Hydrogen deuteride	—	—	77± 6	—

Figure 3 shows the effect of varying temperature with hydrogen of fixed composition, viz. 45% ortho-hydrogen. The point at 4°K refers to solid hydrogen cooled by liquid helium ; the other points refer to liquid hydrogen boiling at different pressures.

In table 1 are given results obtained with other moderators. It is seen that only hydrogen deuteride and methane are comparable with hydrogen in their ability to moderate neutrons to very low energies. The efficient moderation in methane is presumably due to the excitation of rotational levels, for methyl alcohol, which is similar in structure but has a greater molecular moment of inertia, is much less efficient.

2.3. *Conclusion*

Though liquid hydrogen at various temperatures, hydrogen deuteride and methane give similar average beam temperatures, the actual velocity spectra may differ considerably in detail ; in particular their yields of cold

neutrons may differ. Of the moderators found to be efficient however, liquid hydrogen at about its normal boiling point is the easiest to use, and so apparatus was designed which would permit a sample of liquid hydrogen to be maintained at the centre of BEPO†.

Fig. 2

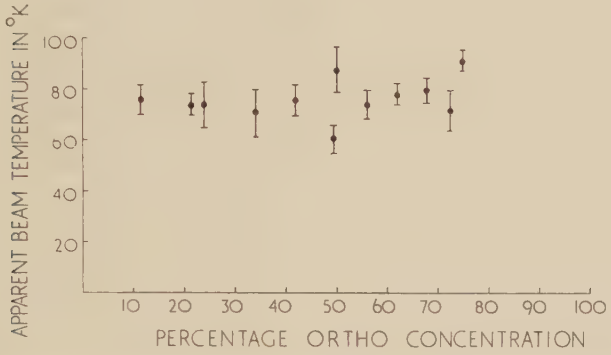

Apparent temperature of a neutron beam scattered from liquid hydrogen at 20°K.

Fig. 3

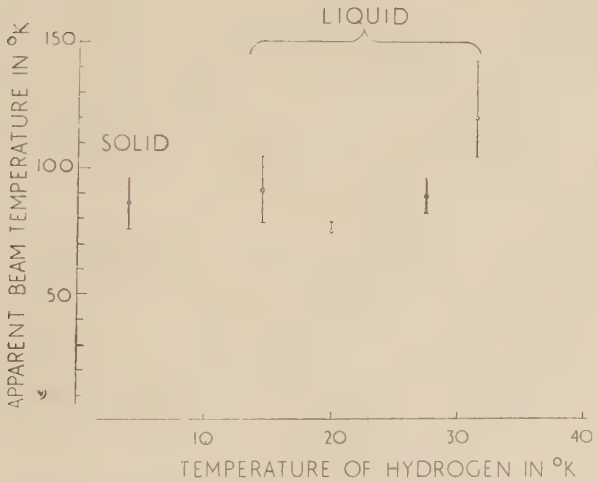

Apparent temperature of a neutron beam scattered from hydrogen of fixed composition at varying temperatures.

---

† It has been pointed out by J. Wright (private communication) that methane would not be a convenient moderator to use in a reactor, since under irradiation it undergoes polymerization and evolves free hydrogen.

§ 3. Safety Aspects†

The presence of some 200 cm³ of liquid hydrogen inside a reactor constitutes a potential explosion hazard. Besides taking all the normal precautions in using liquid hydrogen, we considered it necessary to show that even in the event of an explosion there would be no damage to the reactor.

The low temperature apparatus inside the pile was to be enclosed in a vacuum case of magnesium–zirconium alloy with walls 6 mm thick. To test that this would contain any explosion occurring in the apparatus, explosions were initiated in an identical tube buried vertically in the ground. With the tube filled with the optimum explosive mixture of gaseous hydrogen and air, explosions produced shock waves with peak pressures of 27 atmospheres at the closed end of the tube.

Liquid hydrogen explosions were then investigated. It proved very difficult to ignite mixtures of liquid hydrogen and solid air. We therefore placed separate Dewar vessels of liquid hydrogen and liquid air at the bottom of the tube, filled the tube with hydrogen gas and air and initiated explosion in the gas. Even when we exploded 300 cm³ of liquid hydrogen with the optimum amount of liquid air the tube was only slightly distorted at the point of explosion ; the peak pressure at the end of the tube was 77 atmospheres. The actual vacuum case used in the pile was tested repeatedly to a pressure of 47 atmospheres before assembly.

It is difficult to see how an explosion of the 200 cm³ of liquid hydrogen inside the pile could occur during an experiment with anything approaching the optimum amount of air. A sudden large leakage of air into the vacuum space would cause most of the hydrogen to boil off before much air had condensed. To prevent a slow leakage causing an accumulation of solid air, the vacuum case was not pumped continuously, so that the helium and neon content of the air would cause a noticeable deterioration in the vacuum before much solid air had collected.

§ 4. Bepo Liquid Hydrogen Moderator

An apparatus was installed in BEPO to maintain a volume of liquid hydrogen near the centre of the reactor. The chamber containing the hydrogen was at the centre of a hole traversing the reactor, and was fed with liquid hydrogen from the north face where all the low temperature equipment was situated. Neutrons scattered from the hydrogen and passing along the hole to the south face of the reactor formed a beam available for experimental work.

4.3. *Low Temperature Equipment*

The general lay out of the low temperature equipment is shown in fig. 4, and details of apparatus inside the pile in fig. 5. The liquid hydrogen moderator was contained in an aluminium can K, 7·5 cm diam. and

† Our thanks are due to Mr. J. E. Uppard and Dr. W. G. P. Lamb of A.W.R.E, Foulness for their help with these tests.

6·25 cm long, inside which was a cooler L with aluminium fins. The aluminium tubes (5 mm in diam.) supplying the liquid hydrogen were supported by wires from a set of cages contained inside the vacuum case of magnesium–zirconium alloy (§ 3). This case was 6 m long and extended to the pile face.

Fig. 4

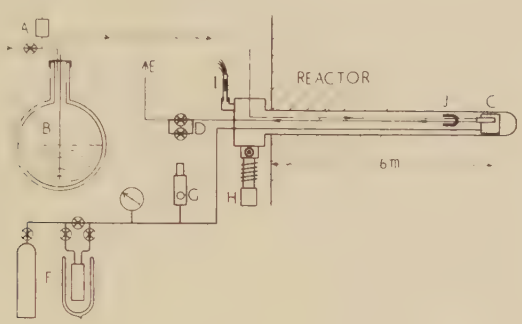

Lay-out of apparatus used to maintain liquid hydrogen in the BEPO reactor: A, Hydrogen gas regulator and relief valve; B, 68 litre liquid hydrogen container; C, moderator chamber; D, control valves; E, duct to atmosphere; F, condensing cylinder and charcoal cleaner; G, relief valve (4·7 atmospheres); H, oil diffusion pump; I, ionization gauge; J, carbon resistance thermometers.

Fig. 5

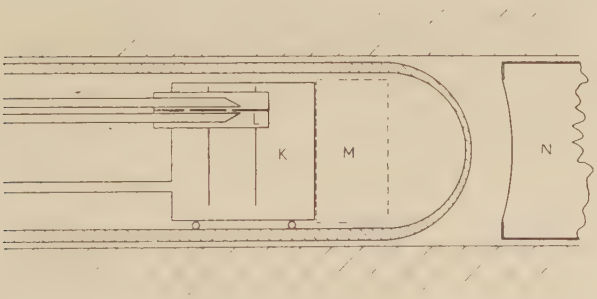

Details of apparatus within reactor core: K, aluminium can; L, cooler; M, beryllium block used in some experiments; N, evacuated flight tube.

Neutrons escaping from the reactor down to the vacuum case would consitute a radiation hazard. Blocks of neutron absorbing material were therefore placed in the vacuum case near the reactor face.

Two separate hydrogen systems were used. The moderator chamber was kept near 20°K by a flow of liquid hydrogen into the cooler L from a 68 litre storage Dewar B. A constant pressure was maintained over the liquid hydrogen in B, and the flow through the circuit controlled by two

valves D at the outlet. After the initial cooling the lowest flow we were able to use was 2 litres of liquid hydrogen an hour, though mechanical failure of the supports of the pipelines and the chamber, later resulted in an increased hydrogen consumption. However the system could be used satisfactorily even when its consumption was as high as 6 litres an hour. The cold gas emerging from the cooler was used to cool a radiation shield surrounding the liquid hydrogen line, thus reducing the heat inflow to it.

The main volume of liquid hydrogen K was condensed into the moderator chamber from a cylinder through a charcoal cleaner, and kept at a pressure of 5 atmospheres. At this pressure the boiling point is 27°K ; by keeping the chamber below this temperature boiling inside the chamber, with consequent fluctuations in the cold neutron flux, was prevented. The low temperature apparatus could be left unattended in this state for many hours. When the liquid hydrogen supply ran out, the hydrogen in the moderator chamber simply escaped from the relief valve G. In some of the experiments a beryllium block M was attached to the face of the moderator chamber (see § 6).

4.2. *Measurement of the Neutron Spectrum*

Neutrons scattered out of the south face of the moderator chamber could leave the pile along an evacuated flight tube (N in fig. 4), 9 cm in diameter, thus forming an external beam. The flight tube extended to the counting equipment, 6 m from the south face of the reactor (i.e. 12 m from the moderator). Collimators of boric acid and paraffin wax reduced the beam diameter to about 4 cm and ensured that the beam consisted only of neutrons coming from the direction of the liquid hydrogen.

The velocity spectrum of the neutrons in the beam was measured with the Harwell slow chopper (Egelstaff 1954), using a BF_3 neutron detector. As the chopper is constructed of cadmium it does not prevent neutrons with wavelengths shorter than 0·3 Å reaching the detector. These neutrons would cause a high background count. By passing the beam, through a block of beryllium, 23 cm long, cooled in liquid nitrogen virtually all neutrons with wavelengths shorter than 4 Å were removed without serious attenuation of the neutrons of longer wavelength.

§ 5. Results

Figure 6 shows the velocity spectrum of the neutron beam obtained when the moderator chamber was filled with liquid hydrogen (about 50% ortho-hydrogen) at 25°K. The rapid fall in counting rate at a neutron time-of-flight of $\sim$1000 μs/m is caused by the beryllium filter. The error bars indicate the statistical uncertainty of the results. Also plotted in fig. 6, on the same scale, is the spectrum obtained with the low temperature moderator replaced by graphite blocks at the pile temperature (130°C), all other conditions remaining unchanged. This second spectrum therefore represents the sort of beam normally used as a source of cold neutrons.

In plotting fig. 6 no allowance has been made for the fact that the detector efficiency, the transmission of the chopper and the transmission of the beryllium all depend on neutron velocity ; the spectra therefore differ somewhat from the true velocity distributions. At any given velocity, however, the ratio of the neutron flux obtained with hydrogen

Fig. 6

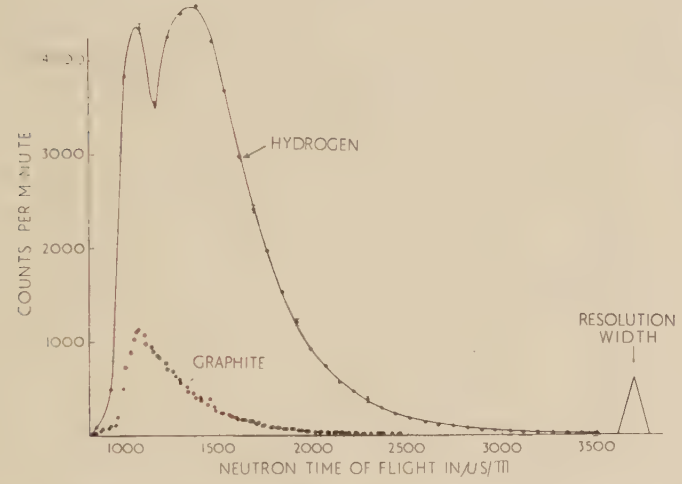

Spectrum of neutrons scattered from liquid hydrogen at 25°K and graphite at 400°K. (Beryllium filter in the beam.) Typical errors are shown.

Fig. 7

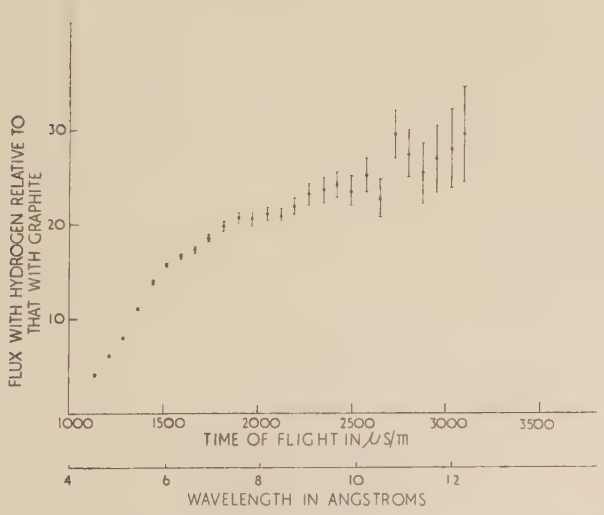

Relative efficiency of hydrogen at 25°K and graphite at 400°K in producing cold neutrons.

to that obained with graphite is independent of these effects. This ratio has been plotted in fig. 7. The curve (which is now independent of the counting system) shows the increase in cold neutrons flux obtained using liquid hydrogen instread of a moderator at pile temperature.

By removing the beryllium filter we extended the measurements of the neutron spectrum to higher velocities. The results are shown in fig. 8. The need to correct for a large background of fast neutrons now makes the statistical accuracy of the results inferior to that of fig. 6, and increases the possibility of systematic error. However, it can be seen from the shape of the curve that, using this amount of liquid hydrogen, moderation to hydrogen temperatures is incomplete.

Fig. 8

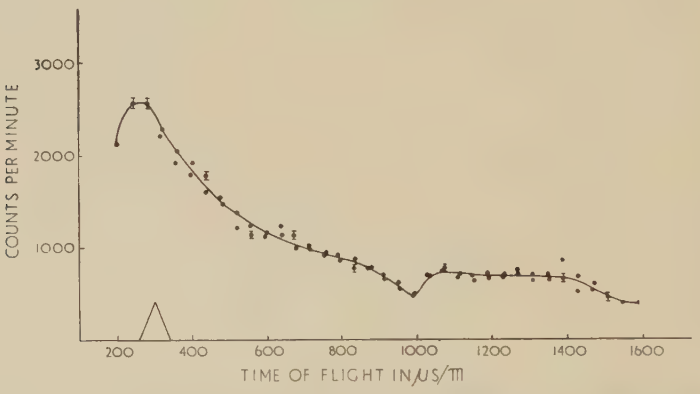

Spectrum of neutrons scattered from liquid hydrogen. (No beryllium filter in the beam.)

It should be noted that in measuring this spectrum the angular velocity of the slow chopper was twice that used in measuring those shown in fig. 6. The consequent change in the effective transmission of the chopper is the cause of the slight difference in appearance, over the same energy range, of the two curves obtained for neutrons scattered from hydrogen.

Since a larger sample of moderator could not be used an attempt was made to increase the efficiency of the moderator by attaching a disc of beryllium, 4 cm thick (M in fig. 5), to the face of the moderator chamber. It was hoped that this would reflect fast neutrons leaving the hydrogen, thus keeping their flux high in the moderator, whilst the escape of cold neutrons would not be impeded. However, the spectrum obtained differed little from that shown in fig. 6.

§ 6. Discussion

In the absence of data on cold neutron cross sections for liquid hydrogen one cannot calculate what neutron velocity spectrum to expect. If moderation were complete in the liquid hydrogen the velocities would have a Maxwell distribution corresponding to 25°K ; this would have a

peak at 1100 μs/m on a time-of-flight scale. It is clear from our results that only partial moderation has been achieved. The beam consists of a broad slowing down spectrum with a low temperature component approximately in thermal equilibrium with the moderator, though even this component is not exactly Maxwellian in form (fig. 8).

The first column in table 2 shows the observed gain in neutron flux using liquid hydrogen as moderator instead of graphite at pile temperature. The second column shows the gain which would be obtained if moderation were complete.

Table 2. Gain in Neutron Flux using Liquid Hydrogen in place of Graphite at 130°C

Neutron wavelength	Observed gain	Gain if moderation complete
5·0 Å	~ 7	60
7·5 Å	~20	135
10·0 Å	~25	180

As a small proportion of the neutrons attain thermal equilibrium with the moderator, it is possible that cooling the hydrogen with liquid helium might bring some neutrons into thermal equilibrium at 4°K, thus further enriching the flux of very long wavelength neutrons, without appreciably altering the apparent temperature of the beam as a whole (see § 4).

§ 7. Conclusion

It has been shown that it is possible and safe to use a low temperature moderator, placed in the core of a reactor, to enrich the flux of cold neutrons in a neutron beam. The large factors of gain which have been obtained with only 200 cm^3 of moderator make the method very attractive. Since the theoretical limit is much higher than the gain observed, the method warrants further development.

Acknowledgments

The authors wish to express their thanks to Mr. T. L. Schofield and Mr. D. H. C. Harris for their help in assembling and running the apparatus, and to Messrs. B. A. Booty, D. H. C. Harris and L. V. Lewis for assisting with the measurements.

References

Egelstaff, P. A., 1954, *J. nuclear Energy*, **1**, 57.

Hughes, D. J., 1953, *Pile Neutron Research* (Cambridge, Mass.: Addison-Wesley, Publishing Co.).

Squires, G. L., and Stewart, A. T., 1955, *Proc. roy. Soc.* A, **230**, 19.

Sutton, R. B., Hall, T., Anderson, E. E., Bridge, H. S., DeWire, J. W., Lavatelli, L. S., Long, E. A., Snyder, T., and Williams, R. W., 1947, *Phys. Rev.*, **72**, 1147.

The Thermal and Magnetic Properties of Ytterbium Ethyl Sulphate between 20°K and 1°K †

By A. H. Cooke, F. R. McKim, H. Meyer and W. P. Wolf
The Clarendon Laboratory, Oxford University

[Received May 13, 1957]

Abstract

The susceptibility of a single crystal of ytterbium ethyl sulphate has been measured between 20°K and 1°K. Below 4°K the results obeyed the relations $\chi_{\parallel}=1{\cdot}08/T$ per mol, and $\chi_{\perp}=0{\cdot}061_5$ per mol. These measurements served to identify the ground doublet state of the ytterbium ion in this case as $|J=\frac{7}{2}, J_z=\pm\frac{3}{2}\rangle$. The magnetic specific heat was measured at five temperatures between 3°K and 1°K by the relaxation method. The results were given by $CT^2/R=4{\cdot}34\times10^{-4}$, in agreement with calculations based on dipole–dipole and hyperfine interactions alone. The spin lattice relaxation time τ was also measured. At 3°K, $\tau\simeq5\times10^{-4}$ sec and was very temperature dependent.

Susceptibility measurements above 4°K indicated the population of excited states, which could not be unambiguously identified. Their separation from the ground state was at least 57°K.

§ 1. Introduction

The rare earth ethyl sulphates form an isomorphous series of salts of the general formula $M(C_2H_5SO_4)_3\ 9H_2O$ where M is the trivalent rare earth ion. They crystallize readily throughout the series in crystals of hexagonal symmetry. The crystal symmetry results in magnetic symmetry, the magnetic susceptibility at any temperature being specified completely by principal values parallel and perpendicular to the hexagonal axis of the crystal. The crystal structure determination made by Ketelaar (1937) shows that all the rare earth ions are magnetically equivalent and the bulk properties are therefore closely related to the properties of the individual ions. The relation is particularly simple since the crystals are magnetically so dilute that interaction effects between the magnetic ions are comparatively unimportant at temperatures above 1°K. Because of these properties, the ethyl sulphates serve as a convenient model series for investigation of the magnetic behaviour of rare earth salts.

Magnetic susceptibility measurements have been made on a number of members of the series (de Haas *et al.* 1933, Fereday and Wiersma 1935)

† Communicated by the Authors.

and several have been investigated by measurement of the magnetic rotation of the plane of polarized light (Faraday effect) (Becquerel *et al.* 1936, 1937, 1938, van den Handel 1940). The results of paramagnetic resonance investigations have been reviewed by Bleaney and Stevens (1953) and by Bowers and Owen (1955). However, prior to the measurements described in this paper, no susceptibility measurements had been made on the last member of the series, ytterbium ethyl sulphate. Bleaney and Scovil (1951) had reported that no paramagnetic resonance could be obtained at 20°K and Cooke and Park (unpublished) found that there was still no resonance down to 4°K.

The magnetic properties of the salts depend on the electric crystalline field in which the paramagnetic ion is situated. Following a suggestion of Ketelaar, Elliott and Stevens (1952, 1953 b) proposed a field of predominantly C_{3h} symmetry, which could be completely specified in any particular case in terms of four parameters. A field of this symmetry has two effects on any manifold J representing a degenerate state of a free ion with an odd number of electrons. The manifold will be split into a series of doublets having eigenstates $|\pm J_z\rangle$ where z is the crystal symmetry axis, and there will also be admixtures between states with J_z differing by 6 within the manifold. The ground state $4f^{13}\ {}^2F_{7\,2}$ of the free Yb^{3+} ion will therefore be split by a C_{3h} crystalline field into four doublets. Two doublets will be characterized by $|\pm\frac{1}{2}\rangle$ and $|\pm\frac{3}{2}\rangle$, these being pure states; the other two will be admixtures between $|\pm\frac{5}{2}\rangle$ and $|\pm\frac{7}{2}\rangle$. When a magnetic field is applied to the crystal these four doublet levels will be split, and, since the condition for there to be an allowed transition between two levels is $\Delta J_z=0$ or ± 1, the only doublet between whose levels there are no allowed transitions is the $|\pm\frac{3}{2}\rangle$ state. If this doublet were lowest then the absence of a paramagnetic resonance spectrum would be explained. This was first pointed out by Elliott and Stevens, who found that a wide variety of crystal field parameters led to a scheme of energy levels having this state lowest. In general the crystal field will also give rise to admixtures between the lowest manifold and excited states, as in the case of cerium (Elliott and Stevens 1952). In most cases these are small and for ytterbium they may be neglected when considering the ground multiplet, as the next J level is some 10 300 cm^{-1} higher.

From measurements on cerium ethyl sulphate, Elliott and Stevens deduced the numerical values of the crystalline field parameters for this salt. They then suggested how the parameters might change from member to member along the rare earth series, and showed that the available data could be satisfactorily explained, although the extrapolation became increasingly uncertain towards the end of the series. It would be particularly interesting, therefore, to determine the values of the parameters for ytterbium, the last magnetic member of the series, as the values for intervening members could then be obtained by interpolation rather than extrapolation. The experiments described here served to identify the ground state unambiguously as $|\pm\frac{3}{2}\rangle$ and showed

that the next doublet was at least 57°K higher, but for reasons discussed below more general conclusions regarding the crystal field parameters could not be drawn.

§ 2. The Measurements

The susceptibility measurements were made on a single crystal using the mutual inductance apparatus described elsewhere (McKim and Wolf 1957). The crystal was prepared from ytterbium oxide supplied by Johnson Matthey whose spectroscopic analysis indicated a purity of at least 99%, the main impurity being samarium oxide (0·5%). Both the temperature dependent and temperature independent contributions to the susceptibility were measured. At temperatures in the liquid helium range the susceptibility in the direction parallel to the crystal axis was found to obey the law

$$\chi_{\parallel} = \frac{1{\cdot}08_3 \pm 0{\cdot}05}{T} \Big/ \text{mol.}$$

No temperature independent susceptibility was detected, the upper limit being 0·01 per mol. From measurements perpendicular to the crystal axis it was found that

$$\chi_{\perp} = 0{\cdot}061_5 \pm 0{\cdot}001 \text{ per mol}$$

independent of temperature throughout the helium range.

Measurements of $\chi_{\parallel}$ and $\chi_{\perp}$ were also made in the liquid hydrogen range. It was found that perpendicular to the crystal axis the susceptibility deviated from the constant value obtained at lower temperatures (see figure), and that parallel to the axis Curie's law was approximately obeyed but with a Curie constant somewhat less than in the helium region. These measurements indicated that $\chi_{\parallel}$ should be equal to $\chi_{\perp}$ at a temperature of 18·0°K and this made it possible to check the consistency of our results by the following very simple experiment. A crystal was suspended with its axis horizontal by a fine thread inside a cryostat whose temperature could be varied by pumping the refrigerant (liquid hydrogen). A large horizontal magnetic field was applied and the crystal was made to oscillate about its axis of suspension. The period of oscillation, t, is then proportional to $(|\chi_{\parallel} - \chi_{\perp}|)^{-1/2}$ and is therefore infinite when $\chi_{\parallel} = \chi_{\perp}$. t was measured at temperatures near 18°K, and from a graph of t^{-2} against T it was found that $\chi_{\parallel} = \chi_{\perp}$ at 18·4°K in good agreement with the value expected from the separate measurements of $\chi_{\parallel}$ and $\chi_{\perp}$.

Magnetic specific heat measurements were made in the liquid helium region by the relaxation method, using the apparatus described by Benzie and Cooke (1950). Measurements were made at five temperatures between 1° and 3°K. The specific heat was found to be inversely proportional to the square of the absolute temperature. In the course of these experiments the spin–lattice relaxation time, τ, was estimated at each temperature and it was found that above 3°K, τ becomes so short

that valid results could no longer be obtained with our apparatus. Values for the magnetic specific heat and also for τ in the range 1° to 3°K are given in the table.

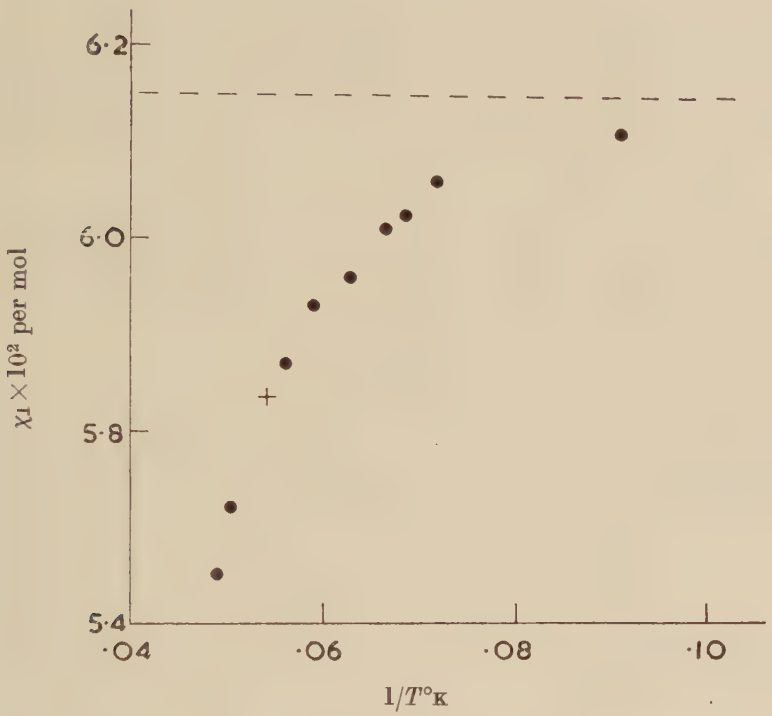

Ytterbium ethyl sulphate. Variation with temperature of the susceptibility perpendicular to the hexagonal axis of the crystal. The symbol + indicates the point where $\chi_{\parallel} = \chi_\perp$ as determined by the oscillation experiment (see text). The dotted line is the value of $\chi_\perp$ below 4·2°K.

T°K	τ sec	C/R per mol	CT^2/R per mol
1·09	—	$3{\cdot}64\times10^{-4}$	$4{\cdot}32\times10^{-4}$
1·40	—	$2{\cdot}20\times10^{-4}$	$4{\cdot}31\times10^{-4}$
2·16	$2{\cdot}1\times10^{-2}$	$9{\cdot}37\times10^{-5}$	$4{\cdot}37\times10^{-4}$
2·68	$2{\cdot}1\times10^{-3}$	$6{\cdot}07\times10^{-5}$	$4{\cdot}36\times10^{-4}$
2·93	$6{\cdot}7\times10^{-4}$	$5{\cdot}03\times10^{-5}$	$4{\cdot}32\times10^{-4}$
3·10	$3{\cdot}5\times10^{-4}$	—	—

§ 3. Discussion

The results of the susceptibility measurements in the helium region may be compared with the general form for the susceptibility of an

assembly of non-interacting ions each in a doubly degenerate ground state,

$$\chi_i = \frac{Ng_i^2\beta^2}{4kT} + \alpha_i \qquad (1)$$

where N is Avogadro's number, β the Bohr magneton, k Boltzmann's constant, g_i the spectroscopic splitting factor for the two levels of the ground state when the measuring field is in the i direction, and α_i is a temperature independent term depending on matrix elements to excited states. Comparison of this formula with the results obtained gave

$$g_{\parallel}=3{\cdot}40\pm0{\cdot}07 \qquad \alpha_{\parallel}=\ 0\pm0{\cdot}01$$
$$g_{\perp}=0{\cdot}00\pm0{\cdot}05 \qquad \alpha_{\perp}=0{\cdot}061\pm0{\cdot}001$$

Of the four possible doublet ground states only $|\pm\frac{3}{2}\rangle$ has $g_{\perp}=0$. The value of $g_{\parallel}$ for this state is equal to $3g_{\mathrm{L}}$ where $g_{\mathrm{L}}=8/7$, the Landé g factor for the $^2F_{7/2}$ manifold. This gives $g_{\parallel}=3{\cdot}43$ in excellent agreement with the experimental value. From this we conclude that the ground state is indeed $|J_z=\pm\frac{3}{2}\rangle$, as suggested by Elliott and Stevens.

The magnetic specific heat measured at the lowest temperatures, when all the ions are in the ground state, contains two contributions, one due to interactions between neighbouring paramagnetic ions in the crystal lattice, the other due to the splitting of the ground state of each ion by nuclear effects. If the interaction specific heat be attributed solely to magnetic dipole–dipole interaction, which is likely as exchange effects are known to be small in the isomorphous neodymium ethyl sulphate (Roberts *et al.* 1953), then by standard methods (Van Vleck 1937, Daniels 1953) it can be shown that

$$\frac{C_{dd}}{R} = \frac{g_{\parallel}^4\beta^4}{32k^2T^2}\left[\sum_j \frac{1}{r_{ij}^6} - 6\sum_j \frac{z_{ij}^2}{r_{ij}^8} + 9\sum_j \frac{z_{ij}^4}{r_{ij}^{10}}\right] + 0\left(\frac{1}{T^3}\right) \qquad (2)$$

where r_{ij} is the distance between the ions i and j and z_{ij} is the component of this along the z-axis. In the temperature range of our measurements only the first terms in this expansion need be considered, and using the values of the lattice sums evaluated by Daniels, eqn (2) reduces to

$$\frac{C_{dd}T^2}{R} = \frac{g_{\parallel}^4\beta^4}{k^2}(532{\cdot}2)a^{-6}$$

when a is the unit cell dimension perpendicular to the hexagonal axis. Taking the value af a as 13·81 Å, obtained by extrapolation of this quantity for earlier members of the rare earth series (Ketelaar 1937), we find

$$\frac{C_{dd}T^2}{R} = 1{\cdot}24\times10^{-4}.$$

The other contribution to the specific heat, due to hyperfine interaction had to be evaluated in an indirect manner in view of the absence of paramagnetic resonance data for this salt. The general spin Hamiltonian describing the interaction of an ion in a doubly degenerate electronic ground state with both a magnetic field and its nucleus is given by

$$\mathscr{H} = \beta\boldsymbol{H}\,.\,g\,.\,\boldsymbol{S} + \boldsymbol{S}\,.\,A\,.\,\boldsymbol{I} \qquad (3)$$

(Abragam and Pryce 1951), neglecting small quadrupole effects. If the electric field which has given rise to the doublet has axial symmetry this reduces to

$$\mathscr{H}=g_{\parallel}\beta H_z S_z+g_{\perp}\beta(H_x S_x+H_y S_y)+A_{\parallel}S_z I_z+A_{\perp}(S_x I_x+S_y I_y).$$

If admixtures from excited states having a J differing from that of the ground manifold can be neglected, we have a simple relation between the principal values of the g and A tensors (Elliott and Stevens 1953 a)

$$\frac{A_{\parallel}}{g_{\parallel}}=\frac{A_{\perp}}{g_{\perp}}=\gamma$$

where γ is a constant for the ion independent of the particular crystal field in the salt. Thus, for the state $|\pm\frac{3}{2}\rangle$, for which $g_{\perp}\equiv 0$, $A_{\perp}=0$, and the spin Hamiltonian reduces to the simple form

$$\mathscr{H}=g_{\parallel}\beta H_z S_z+(\gamma g_{\parallel})S_z I_z.$$

The constant γ was calculated from the resonance data on ytterbium acetate (Cooke and Park 1956) for which transitions within the lowest doublet are not forbidden as in the ethyl sulphate.

In zero field a spin Hamiltonian of the form (3) leads to a specific heat contribution

$$\frac{C_N}{R}=\frac{1}{9}\left(\frac{hc}{kT}\right)^2\{(\gamma g_{\parallel})^2 S(S+1)I(I+1)\}$$

(Bleaney 1950). Substituting the value of γ obtained from the acetate and allowing for the abundances of the two Yb isotopes with non-zero spin, we find

$$\frac{C_N T^2}{R}=3{\cdot}22\times 10^{-4}.$$

The sum of the two contributions yields a total specific heat given by $CT^2/R=4{\cdot}46\times 10^{-4}$, compared with the measured value of $4{\cdot}34\times 10^{-4}$. The close agreement between these confirms that there is very little contribution from exchange interaction to the specific heat, which can be explained in terms of magnetic dipole–dipole and hyperfine interactions alone.

The effect on the low temperature susceptibility of the dipole–dipole and nuclear interactions can similarly be calculated in terms of the lattice parameters, g value and the constant γ. Expressing the correction in terms of a power series in $1/T$ it can be shown (Daniels 1953) that dipole–dipole interaction contributes a term $-(0{\cdot}013/T)\chi_0$, where χ_0 is the first order term in $1/T$ given by eqn (1) while the effect of nuclear interaction enters only in the next approximation (Bleaney 1950). At temperatures down to 1°K these corrections are therefore negligible and Curie's law is obeyed. Below 1°K they become increasingly more important, but even down to 0·1°K the deviations from Curie's law will be small.

The deviation of the susceptibility in the hydrogen region from its behaviour in the helium region was interpreted as due to some ytterbium

ions being excited into states other than the ground doublet. Population of these excited states will also give rise to a Schottky anomaly in the specific heat, which at the low temperature end has the form

$$CT^2/R = \Delta^2 \exp[-(\Delta/T)],$$

where Δ is the energy of the first excited state, expressed in °K. This result is quite independent of the magnetic strength of the excited states since the specific heat depends only on the energy difference between the states, and not on their quantum description. Now at the highest temperature of measurement, 2·93°K, no onset of an anomaly was observed. Assuming that a 5% variation in CT^2/R would have been detected, a lower limit could be put on Δ, namely $\Delta \geq 57$°K. Other than this, it was not possible to draw any definite conclusions about the identification and positions of the excited states. Calculations showed that the susceptibility results could not be explained with the $|\pm\frac{1}{2}\rangle$ state as the first excited state and the other two states at much higher energies, whereas a reasonable fit was obtained with one doublet, principally $|\pm\frac{5}{2}\rangle$ with a small admixture of $|\pm\frac{7}{2}\rangle$ at about 70°K above the ground state. But the possibility of there being two doublets at about the same energy separation from the ground state could not be excluded. It would be very desirable to have specific heat measurements at temperature above 3°K. If the onset of the Schottky anomaly could be observed then it would be possible to decide whether one or two excited states were being populated, and to obtain some idea of the splitting between these levels and the ground state.

The susceptibility measurements have shown that at temperatures below 4°K ytterbium ethyl sulphate is completely anisotropic. If a single crystal is demagnetized adiabatically then the subsequent application of a large magnetic field perpendicular to the crystal axis will produce no heating. It is therefore a better substance than is cerium ethyl sulphate for the type of magnetic experiments below 1°K suggested previously by Bogle *et al.* (1951). Measurements of the thermodynamic properties below 1°K have recently been made and will be published in due course, together with experiments in nuclear alignment.

References

Abragam, A., and Pryce, M. H. L., 1951, *Proc. roy. Soc.* A, **205**, 135.

Becquerel, J., de Haas, W. J., and van den Handel, J., 1936, *Physica*, **3**, 1133; 1937, *Ibid.*, **4**, 345, 543; 1938, *Ibid.*, **5**, 753.

Benzie, R. J., and Cooke, A. H., 1950, *Proc. phys. Soc. Lond.* A, **63**, 201.

Bleaney, B., 1950, *Phys. Rev.*, **78**, 214.

Bleaney, B., and Scovil, H. E. D., 1951, *Proc. phys. Soc. Lond.* A, **64**, 204.

Bleaney, B., and Stevens, K. W. H., 1953, *Rep. Progr. Phys.*, **16**, 108.

Bogle, G. S., Cooke, A. H., and Whitley, S., 1951, *Proc. phys. Soc. Lond.* A, **64**, 931.

Bowers, K. D., and Owen, J., 1955, *Rep. Progr. Phys.*, **18**, 304.

Cooke, A. H., and Park, J. G., 1956, *Proc. phys. Soc. Lond.* A, **69**, 282.

Daniels J. M., 1953, *Proc. phys. Soc. Lond.* A, **66**, 673.

de Haas, W. J., van den Handel, J., and Gorter, C. J., 1933, *Phys. Rev.*, **43**, 81.

ELLIOTT, R. J., and STEVENS, K. W. H., 1952, *Proc. roy. Soc.* A, **215**, 437 ; 1953 a, *Ibid.*, **218**, 553 ; 1953 b, *Ibid.*, **219**, 387.
FEREDAY, R. A., and WIERSMA, E. C., 1935, *Physica*, **2**, 575.
KETELAAR, J. A. A., 1937, *Physica*, **4**, 619.
MCKIM, F. R., and WOLF, W. P., 1957, *J. sci. Instrum.*, **34**, 64.
ROBERTS, L. D., SARTAIN, C. C., and BORIE, B., 1953, *Rev. mod. Phys.*, **25**, 170.
VAN DEN HANDEL, J., 1940, *Thesis*, Leiden.
VAN VLECK, J. H., 1937, *J. chem. Phys.*, **5**, 320.

CORRESPONDENCE

Cascade Decay of a Heavy K-Meson

By S. N. Sen Gupta and M. S. Sinha
Bose Institute, Calcutta

[Received April 5, 1957]

A cloud chamber evidence for cascade decay of a heavy charged unstable particle is reported here. The picture shows two V-events, one due to a charged particle and the other due to a neutral particle. From a consideration of the coplanarity of the apex of the charged V-event and the tracks of the two secondaries of the other and also of the angles of emission and minimum ionization of all the decay products it appears that a heavy particle of mass not below 1460 m_e has undergone a cascade decay process according to the mode

$$K^{\pm} \rightarrow L^{\pm} + \theta \rightarrow \pi^{+} + \pi^{-} + 212 \text{ Mev.}$$

The photograph reproduced in fig. 1 (Plate), shows that a charged particle PO, which is produced in an interaction at P (Cu-plate), traverses about 5 cm with 2–3 times minimum ionization and then decays in the gas at O. The charged decay product OA starting from O disappears towards the rear of the chamber at minimum ionization after passing through 29 g of Cu equivalent. At O′ a V^0-particle is found to decay into two minimum ionizing particles O′B and O′C, the former disappearing through the left side-wall and the latter through the front plate of the cloud chamber after penetrating 15 g of Cu equivalent without multiplication.

Since both the events take place in the gas volume, we exclude the possibility of a capture process at O or a pair creation of electrons at O′ and proceed to correlate the two events. A stereo-projection shows that the decay point O of the charged V-track POA lies in the plane containing the two decay tracks O′B and O′C of the neutral V-event within $\pm 3°$. This strongly suggests that the particle PO has a neutral decay product OO′ besides the charged one OA, and this neutral particle most probably produces the decay event at O′. The angles made by the emitted particles with their respective parents in space are shown schematically in fig. 2.

Interpretation

Since most of the neutral V-events are either Λ^0 or θ^0 decays, we naturally try to identify the V^0-event at O′ with one of them. If we assume it to be a case of Λ^0 decay, it follows that the particle O′B making

the smaller angle of 27° with the line of flight of the neutral particle should be a proton and the other particle O′C making the angle 65° a π-meson. Since O′B is a proton travelling with minimum ionization its momentum must exceed 1 Gev/c. Conservation of momenta and energies then leads to a minimum mass of 1·7 Gev for the neutral particle OO′, which rules out the possibility of identifying it with a Λ^0. A similar calculation with the assumption that it is a case of θ^0 decaying into two pions gives a minimum mass value of 468 Mev for the V^0-particle. Here, we take the momentum of the vertical secondary O′C which makes the larger angle and remains at minimum ionization after passing through 15 g of Cu, to be at least 180 Mev/c at the point of emission. The lower limit of 468 Mev for the mass of the neutral particle is not far from the known θ^0-mass of 493 Mev. We, therefore, conclude that the neutral particle OO′ is a θ^0-particle.

Fig. 2

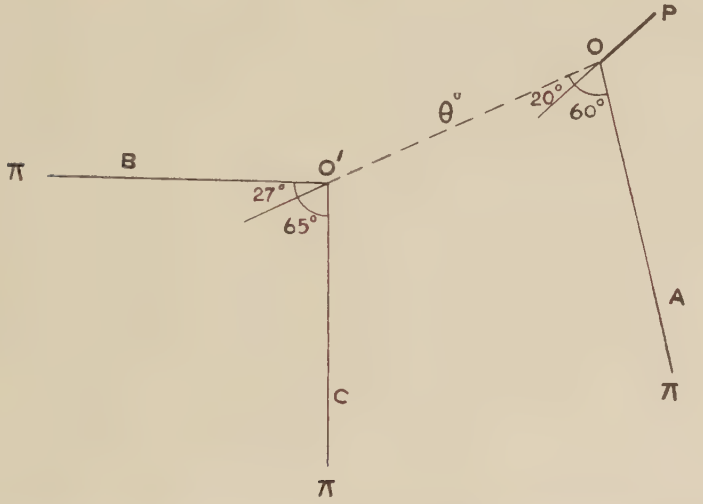

The various angles made in space by the different secondaries with their respective parents are shown schematically.

The identification of the charged decay product OA is made in an indirect way. Since OO′ makes an angle (20°) which is much smaller than that (60°) made by OA with the parent particle PO, we can reasonably conclude that the particle OA is considerably lighter than OO′. The particle OA is therefore taken to be an L-meson of a minimum momentum 190 Mev/c at the point of emission corresponding to an almost minimum ionization even after passing through 29 g of Cu equivalent. Assuming a two-body decay of PO, conservation of transverse momentum requires a minimum momentum of 481 Mev/c for the neutral secondary OO′, which has been previously identified with a θ^0. Conserving energy and longitudinal momentum the minimum mass and momentum which we

find out for the primary particle PO are 745 MeV (1460 m_e) and 549 MeV/c respectively pointing to an ionization of 2·5 times minimum which is quite consistent with its observed ionization.

All cascade decays so far reported (Thompson 1956) have Λ^0 as the neutral secondary and one leg of the secondary decay event has been invariably of more than minimum ionization. In the present picture both the secondaries of the secondary decay event at O′ are distinctly of minimum ionization and therefore its identification with a Λ^0 decay is not possible.

Another possibility is that the θ^0 decaying at O′ and the K-particle decaying at O might have been produced in the same interaction at P. This is very unlikely since the plane containing O′B and O′C makes an angle of more than 15° with the point P obtained by joining the three visible tracks emitted from that plate.

Lifetimes of the Particles

As both the decays have occurred in flight and the decaying particles are both produced within the visible region, a lifetime determination is possible. The paths traversed by the charged and neutral decaying particles are 5 ± 1 and 16 ± 2 cm respectively in the laboratory system between production and decay. We, however, know only the lower limit of their momenta and this gives an upper limit for the lifetimes as $2{\cdot}5\times10^{-10}$ and $6{\cdot}5\times10^{-10}$ sec for the charged and neutral particles respectively. From the above considerations it appears that the two V-events in fig. 1 (Plate) are actually linked with each other and they represent a case of cascade decay of a charged K-particle whose mass is above 1460 m_e and whose lifetime is below $2{\cdot}5\times10^{-10}$ second.

Acknowledgments

The authors wish to acknowledge with thanks the financial support from the Atomic Energy Commission, Government of India. They are also grateful to Dr. D. M. Bose, Director, Bose Institute, for his kind interest and for offering facilities to work at the high altitude station of the Bose Institute at Darjeeling, where this picture was obtained.

Reference

Thompson, R. W., 1956, *Prog. Cosmic Ray Phys.*, **3**, 294.

REVIEWS OF BOOKS

Theories of Nuclear Moments. By R. J. Blin-Stoyle. (Oxford University Press.) [Pp. 88.] Price 8*s.* 6*d.*

In these days of intense specialisation, when papers on any one subject appear in many journals and advanced textbooks are invariably expensive, the introduction of a new series of inexpensive paper-backed monographs called the *Oxford Library of the Physical Sciences* is most welcome.

This volume, the first of the series, is mainly concerned with a comparison of the predictions of theories based on simple nuclear models with the experimental results. It contains an excellent account of moment calculations using the different particle and collective models, and the effects of meson currents, velocity dependent forces, intermediate coupling and interconfigurational mixing are discussed in some detail. A chapter on the experimental methods of measuring nuclear spins and moments is included for completeness, and several tables of moments, both experimental and theoretical, with notes about the relevant models are set out in the text and in an appendix. K. F. S.

Fatigue in Aircraft Structures. Proceedings of the International Conference held at Columbia University, January 30th to February 1st, 1956. Edited by A. M. Freudenthal. (New York : Academic Press Inc. ; London : Academic Books Ltd.) [Pp. ix + 456.] Price $12.00.

This book contains a number of contributions on the effect of fatigue on design of aircraft and on cumulative damage under varying stress. In addition there are several very interesting review papers, by Wood, Forsyth, Thompson and others on the physical processes observed as a fatique crack is developing, though it is not made clear whether this work has as yet contributed to the development of alloys for practical purposes. N. F. M.

Progress in Low Temperature Physics. Edited by C. J. Gorter. (North Holland Publishing Company.) [Pp. xi + 480.] Price 84*s.*

The second volume of " Progress in Low Temperature Physics ", like its predecessor, is of very uneven quality and interest, but it possesses enough articles of value that one may welcome its appearance. It may however be queried whether Low Temperature Physics is nowadays a sufficiently self-contained topic to justify a regular examination of its progress. Certainly some of the articles here on solid-state matters, such as the one concerned with semi-conductors, suffer from too rigid an attention being paid to the low temperature aspects, while at the other extreme the article on the rare-earth metals hardly seems to qualify for admission into this volume. Of the traditional problems of low temperature research, liquid helium is well represented by 137 out of the 480 pages, while 13 is all that is allowed to super-conductivity. Perhaps this bias, already noticeable in the first volume, may be taken to reflect the special interests of the editor, whose hand is also understandably discernible in the choice of authors. This tendency, normally beneficial or at any rate harmless, is rather regrettable when it lends itself to partisanship in the current controversy over an improved temperature scale, a matter which has already led to acrimony and in which the right is by no means obviously on one side or the other.

Much that is discussed here is of such ephemeral interest, and that only to the low temperature specialist, that it is encouraging to find extended accounts of topics which in the future may have something to contribute in a wider sphere than mere low temperature physics ; the articles by Shoenberg on the de Haas-van Alphen effect and by Steenland and Tolhoek on nuclear orientation are on this account particularly welcome, and help to redeem the volume of something of the atmosphere of a parish magazine. A. B. P.

The Defect Solid State. By T. J. Gray, D. P. Detwiler, D. E. Rase, W. G. Lawrence, R. R. West and T. J. Jennings. (New York: Interscience Publishers Inc.; London: Interscience Publishers Ltd.) [Pp. vii+511.]

This book is a gallant attempt on the part of members of the staff of the College of Ceramics of Alfred University, New York, to put together the fundamental parts of the physics and chemistry of the solid state which are relevant to the branch of technology with which the College is concerned. This includes the properties of dielectrics, magnetism, corrosion and in particular reactions in solids. Inevitably, through covering so wide a field, the treatment is sketchy in places; but none the less this attempt to provide a textbook of fundamental theory for a particular industry is of real interest. N. F. M.

Photographic Sensitivity. Vol. 1. Hakone Symposium. Edited by Shin Fujisawa. (Tokyo: Maruzen Co. Ltd.) [Pp. 147.] Price $4.00.

Under the title "Photographic Sensitivity Vol. 1" published by the Maruzen Company, Tokyo, 1956, are published the Proceedings of a Symposium held at Hakone in September 1953. There were some forty attenders, mostly Japanese, but including N. F. Mott and F. C. Frank from Bristol and F. Seitz from the University of Illinois. The main subjects covered The Physical Properties of Silver Halides and Photographic Emulsions, ranging from lattice defects and the orientation of print-out silver with respect to the parent silver-halide crystal to the chemical sensitization of emulsions and the mechanism of sensitivity of collodion emulsions. This successful venture was continued on two later occasions by The Group of Research Workers on Lattice Defects, and it is planned to issue further publications in the same form. W. F. B.

Elements of Partial Differential Equations. By I. N. Sneddon. (London and New York: McGraw-Hill.) [Pp. ix+327.] Price $7.50.

This is an account of methods for finding analytical solutions of partial differential equations. There is more to it than would be needed by most undergraduates, but the unsophisticated treatment of many different techniques should make it extremely useful for theoretical physicists, engineers, and other applied mathematicians. There are numerous examples and problems.

J. M. Z.

Scientific Uses of Earth Satellites. By James A. van Allen (ed. by). (Chapman & Hall.) [Pp. x+316.] Price 63*s*.

This book contains 33 articles given at a meeting of the U.S. Upper Atmosphere Rocket Research Panel in January, 1956. The subjects covered are satellite orbits, methods of tracking, instrumentation and measurements using satellites, both from the ground and from instruments in the satellite. The subjects whose investigation is considered include the figure of the earth, air density and composition, meteorology, meteorites, solar radiation, cosmic rays, terrestrial magnetism, the ionosphere and the aurora.

The articles are of considerable interest. They represent practicable experiments most of which we may expect to see carried out during the next twenty years. One of the most ambitious projects is to fly a mass spectrometer in a satellite. E. C. B.

[The Editors do not hold themselves responsible for the views expressed by their correspondents.]

Fig. 1

Etch pattern.

Fig. 2

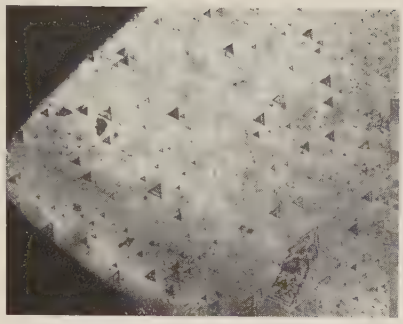

Etch pattern.

Fig. 3

Natural pattern.

Fig. 4

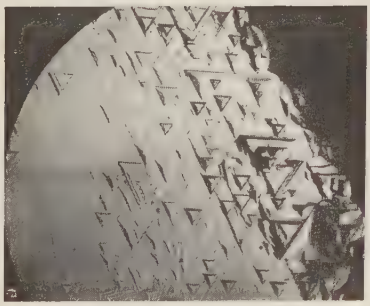

Natural pattern.

Fig. 5

Natural pattern.

Fig. 6

Etch pattern.

Fig. 7

Natural pattern.

Fig. 8

Etch pattern.

Fig. 9

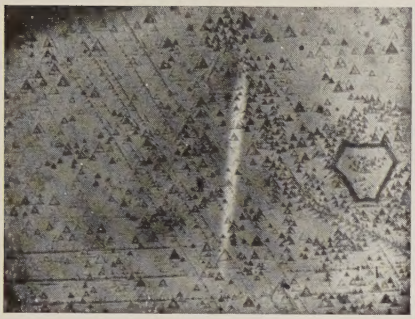

Etch pattern.

Fig. 10

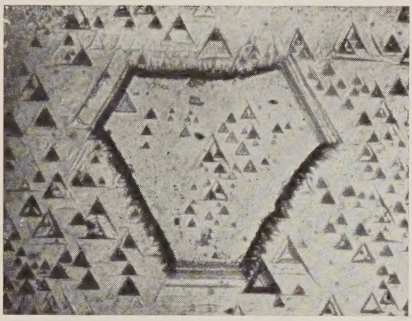

Etch pattern.

Fig. 11

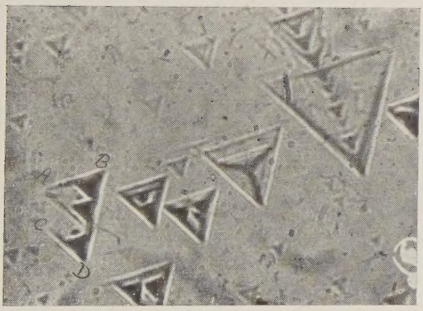

Etch pattern.

Fig. 12

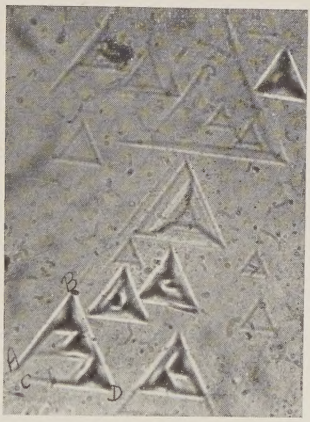

Etch pattern.

Fig. 13

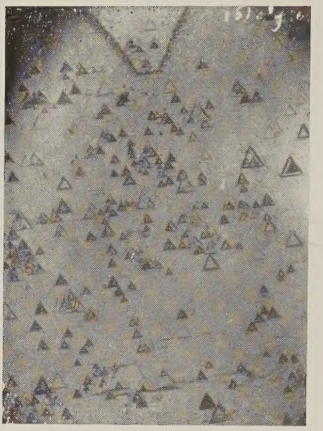

Etch pattern.

Fig. 14

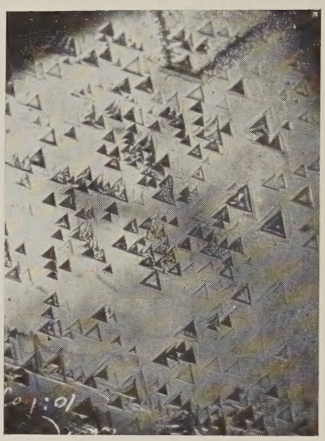

Etch pattern.

Fig. 15

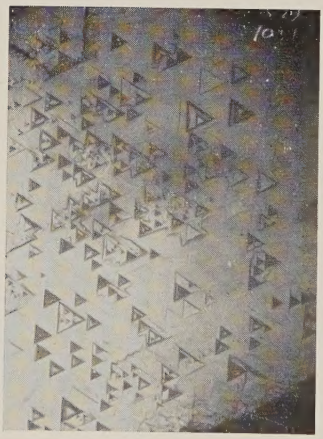

Etch pattern.

Fig. 16

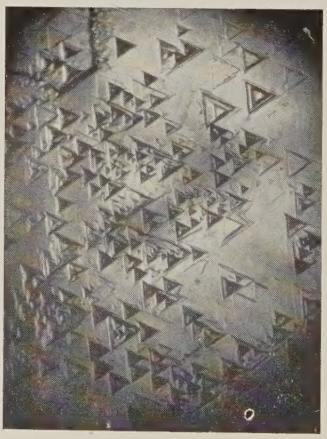

Etch pattern.

Fig. 1

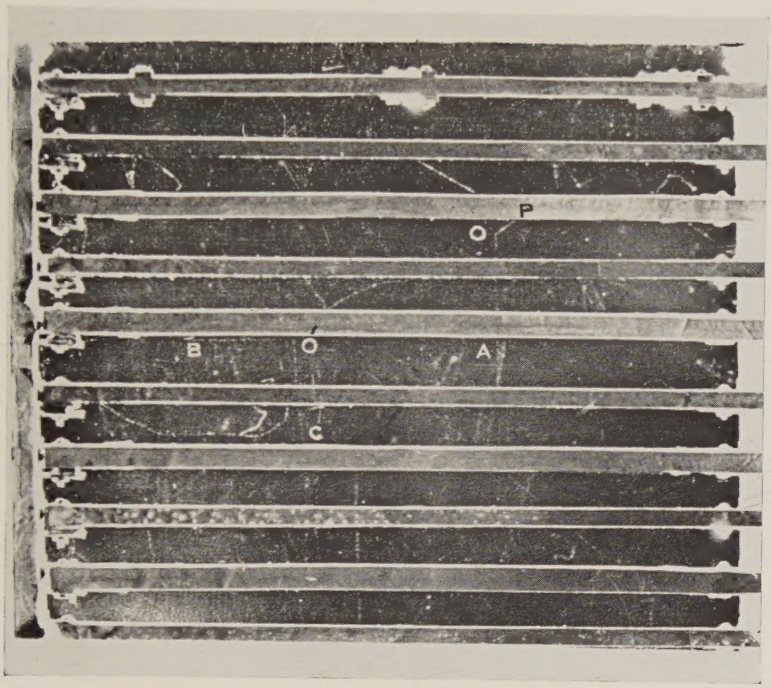

Left view

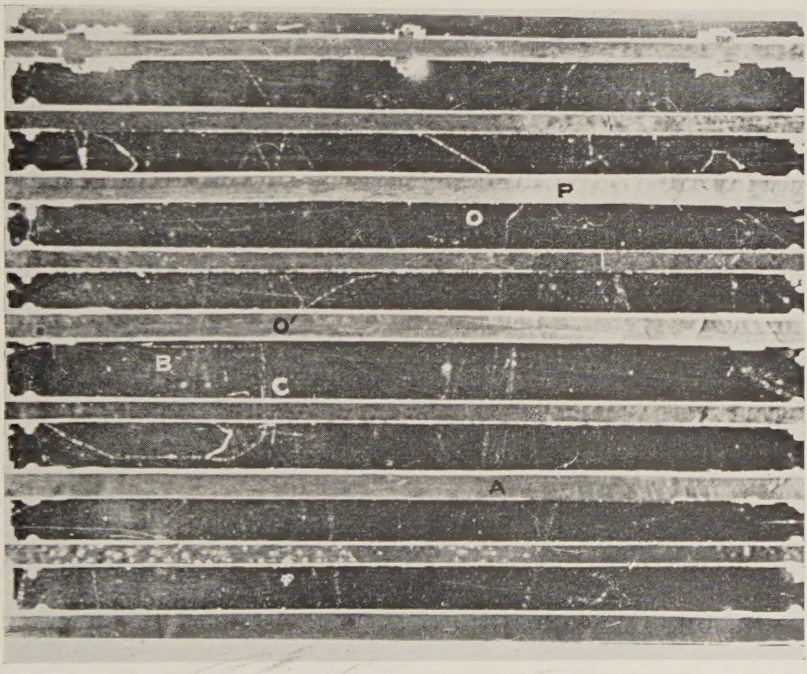

Right view

Photograph showing the decays of a charged particle at O and a neutral particle at O′. The plane containing the secondaries O′B and O′C of the V^0-event at O′ passes through O within $\pm 3^0$. It is interpreted that the mass of the particle PO is above 1460 m_e and it decays into an L-meson OA and a θ^0 represented by OO′ which subsequently decays into two pions O′B and O′C.